



HAL
open science

Structural and chemical heterogeneity of Proterozoic organic microfossils of the ca. 1 Ga old Angmaat Formation, Baffin Island, Canada

Sami Nabhan, Linda C Kah, Bhoopesh Mishra, Kilian Pollok, Ashley R Manning-berg, Mark A Zuilen

► **To cite this version:**

Sami Nabhan, Linda C Kah, Bhoopesh Mishra, Kilian Pollok, Ashley R Manning-berg, et al.. Structural and chemical heterogeneity of Proterozoic organic microfossils of the ca. 1 Ga old Angmaat Formation, Baffin Island, Canada. *Geobiology*, 2021, 19 (6), pp.557 - 584. 10.1111/gbi.12463. hal-03426869

HAL Id: hal-03426869

<https://hal.science/hal-03426869>

Submitted on 22 Nov 2021

HAL is a multi-disciplinary open access archive for the deposit and dissemination of scientific research documents, whether they are published or not. The documents may come from teaching and research institutions in France or abroad, or from public or private research centers.

L'archive ouverte pluridisciplinaire **HAL**, est destinée au dépôt et à la diffusion de documents scientifiques de niveau recherche, publiés ou non, émanant des établissements d'enseignement et de recherche français ou étrangers, des laboratoires publics ou privés.

1 **Structural and chemical heterogeneity of Proterozoic organic microfossils of the ca. 1 Ga**
2 **old Angmaat Formation, Baffin Island, Canada**

3

4 **Sami Nabhan**¹, **Linda C. Kah**², **Bhoopesh Mishra**³, **Kilian Pollok**⁴, **Ashley R. Manning-Berg**⁵, **Mark**
5 **A. van Zuilen**¹

6

7 ¹ Université de Paris, Institut de Physique du Globe de Paris, CNRS, F-75005 Paris, France

8 ² Department of Earth and Planetary Sciences, University of Tennessee, Knoxville, TN, USA

9 ³ School of Chemical and Process Engineering, University of Leeds, Leeds, UK

10 ⁴ Institute of Geosciences, Friedrich Schiller University Jena, Jena, Germany

11 ⁵ Department of Biology, Geology and Environmental Science, University of Tennessee at
12 Chattanooga, Chattanooga, TN, USA

13

14 **Abstract**

15 Organic microfossils in Meso- and Neoproterozoic rocks are of key importance to track the emergence
16 and evolution of eukaryotic life. An increasing number of studies combine Raman-spectroscopy with
17 synchrotron-based methods to characterize these microfossils. A recurring observation is that Raman-
18 spectra of organic microfossils show negligible variation on a sample scale and that variation between
19 different samples can be explained by differences in thermal maturation or in the biologic origin of
20 organic precursor material. There is a paucity of work, however, that explores the extent to which the
21 petrographic framework and diagenetic processes might influence the chemical structure of organic
22 materials. We present a detailed Raman-spectroscopy based study of a complex organic microfossil

23 assemblage in the ca. 1 Ga old Angmaat Formation, Baffin Island, Canada. This formation contains
24 abundant early diagenetic chert that preserves silicified microbial mats with numerous, readily
25 identifiable organic microfossils. Individual chert beds show petrographic differences with discrete
26 episodes of cementation and recrystallization. Raman-spectroscopy reveals measurable variation of
27 organic maturity between samples and between neighboring organic microfossils of the same
28 taxonomy and taphonomic state. Scanning transmission X-ray microscopy performed on
29 taphonomically similar coccoidal microfossils from the same thin section shows distinct chemical
30 compositions, with varying ratios of aromatic compounds to ketones and phenols. Such observations
31 imply that geochemical variation of organic matter is not necessarily coupled to thermal alteration or
32 organic precursor material. Variation of the Raman signal across single samples is most likely linked to
33 the diagenetic state of analyzed materials and implies an association between organic preservation
34 and access to diagenetic fluids. Variation in the maturity of individual microfossils may be a natural
35 outcome of local diagenetic processes and potentially exceeds differences derived from precursor
36 organic material. These observations stress the importance of detailed in-situ characterization by
37 Raman-spectroscopy to identify target specimens for further chemical analysis.

38

39 **Keywords**

40 Mesoproterozoic, organic microfossils, Angmaat Formation, Raman-spectroscopy

41

42 **1. Introduction**

43 **1.1. Carbonization and graphitization of organic matter**

44 Organic material (OM) in sedimentary and metasedimentary rocks experiences irreversible alteration
45 that includes both carbonization and subsequent graphitization processes (Romero-Sarmiento et al.,
46 2014; Buseck and Beyssac, 2014; Rouzaud et al., 2015; Delarue et al., 2016). Carbonization refers to
47 the broad set of organic processes that take place at temperatures typically lower than approximately

48 330 °C, where OM becomes dehydrated, long chained organic molecules break down into shorter
49 chains, and the ratio of aromatic molecules increases (Buseck and Beyssac, 2014; Rouzaud et al.,
50 2015). These changes are frequently determined by proxies such as the H:C ratio which decreases with
51 increasing degree of carbonization (Vendenbroucke and Largeau 2007; Ferralis et al., 2016). At low
52 degrees of carbonization, equivalent to the oil window (50-150 °C), OM in Phanerozoic rocks can be
53 further subdivided into three different types of kerogen with chemical fingerprints that have been
54 crudely assigned to different organic precursor materials including lacustrine algae, marine and
55 lacustrine planktonic algae, and terrestrial plants (Vendenbroucke and Largeau 2007). At higher
56 degrees of carbonization, equivalent to the gas window (150-200 °C), organic precursor materials can
57 be examined using a combination of analytic techniques including Raman-spectroscopy, micro-FTIR,
58 micro-XANES and STXM (Bernard et al., 2007; Bernard et al., 2009; Qu et al., 2015 and 2018; Bonneville
59 et al., 2020). These techniques, however, allow only for a limited assignment to the three primary
60 domains of life, namely Archaea, Bacteria and Eukarya, and assignation is often limited to the simpler
61 subdivision between Prokaryotes and Eukaryotes (Igisu et al., 2009; Qu et al., 2015). Nevertheless,
62 such classification of organic precursor material is particularly interesting for Precambrian
63 sedimentary rocks that may preserve evidence of the early emergence of eukaryotic life (Javaux et al.,
64 2001; Knoll, 2014; Butterfield, 2015; Javaux and Lepot, 2018).

65 During metamorphism organic material experiences dominantly physical transformation to crystalline
66 graphite while chemical transformations associated with carbonization gradually ceases (Beyssac et
67 al., 2002; Buseck and Beyssac, 2014). This change is associated with the onset of graphitization at
68 metamorphic temperatures of ca. 330 °C (Delarue et al., 2016). A direct correlation between
69 increasing peak metamorphic temperature and the degree of graphite crystallinity has led to the
70 widely accepted use of Raman spectroscopy as geothermometer to estimate maximum metamorphic
71 temperatures (Beyssac et al., 2002; Rahl et al., 2005; Beyssac et al., 2007; Aoya et al., 2010; Lahfid et
72 al., 2010; Kouketsu et al., 2014). Thermometry based on graphite crystallinity, however, is most
73 reliable at a thermal alteration of the host rock between ca. 330 °C and 650 °C (Beyssac et al., 2002;

74 Rahl et al., 2005; Beyssac et al., 2007; Aoya et al., 2010). Above 650 °C OM is mostly, if not completely,
75 converted to graphite with a uniform and stable Raman signal (Beyssac et al., 2002). Furthermore,
76 chemical characterization of preserved microfossils is strongly limited to lower graphitization and only
77 possible in rare cases of pristine preservation by the use of nano-structural identification techniques
78 like STXM and TEM (Bernard et al., 2007; Bernard et al., 2009; Lepot et al., 2009).

79 The development of a variety of spectral fitting protocols to infer temperatures of maturation prior to
80 graphitization highlight spectral change derived from a number of ancillary spectral peaks (Sadezky et
81 al., 2005; Lahfid et al., 2010; Kouketsu et al., 2014; Lünsdorf et al., 2014a and b; Henry et al., 2019).
82 However, there is substantial difficulty in producing accurate geothermometers at temperatures
83 equivalent to burial diagenetic overprints (<150 °C) that reflect the lowest levels of carbonization
84 because most Raman parameters used to estimate thermal overprint do not show a linear behavior
85 at such low temperatures (Lahfid et al., 2010; Kouketsu et al., 2014; Henry et al., 2019). Other spectral
86 fitting techniques have been used to assign a Raman Index of Preservation (RIP; Schopf et al., 2005;
87 Czaja et al., 2016).

88 **1.2. Understanding maturity within Proterozoic microfossiliferous rocks**

89 Proterozoic sedimentary rocks that contain recognizable organic microfossils commonly preserve OM
90 that has undergone some extent of carbonization (in diagenetic and burial environments), but less
91 frequently have reached graphitization stages associated with metamorphism. Exceptions are
92 reported from extraordinary examples (Schopf et al., 2005). As noted above, in less thermally mature
93 samples Raman spectroscopy is commonly used to characterize the maturity (or degree of alteration)
94 of OM residues of individual microfossils (Schopf et al., 2005; Ferralis et al., 2016; Baludikay et al.,
95 2018; Guo et al., 2018; Manning-Berg et al., 2019; Pang et al., 2020). A commonality among most of
96 these studies is that the Raman signal is broadly homogeneous on a sample-, outcrop- and often even
97 formation-scale. The recent discovery of microfossiliferous units with heterogeneous Raman signals

98 led to the conclusion that the observed difference in the Raman signal must relate to differences in
99 organic precursors (Qu et al., 2015; Pang et al., 2020).

100 It remains unclear, however, whether (and to what extent) small-scale differences in the diagenetic
101 framework of geological samples may influence the maturity of the OM they host. Precambrian chert
102 is well-known to preserve microfossils across an array of taphonomic states (Schopf et al., 2005;
103 Edwards et al., 2012; Guo et al., 2018; Manning-Berg et al., 2019), and that microfossil-preserving
104 chert can also show fabrics that potentially arise from discrete stages of silicification (Manning-Berg
105 and Kah, 2017). Although the primary taphonomic differences reflect a time-frame of days to months
106 (Bartley, 1996), we have little understanding of the role that diagenetic changes, including the timing
107 of the precipitation of primary and secondary mineral phases, and the recrystallization of microfossil-
108 associated diagenetic phases, may play in the maturation of preserved OM. It therefore remains to be
109 determined whether, in low-temperature diagenetic environments, variation in maturity reflects
110 differences in the diversity of organic precursors, or diagenesis.

111 Here we present a detailed investigation of chert from the ca. 1.0 Ga Angmaat Formation, Arctic
112 Canada (Figure 1), that combines petrographic assessment of microfossiliferous and OM-bearing
113 mineral phases with Raman-spectroscopy and Scanning transmission x-ray microscopy (STXM) of
114 discrete organic phases. Microfossil assemblages in the strata of the Angmaat Formation experienced
115 low-grade diagenesis involving silicification, diagenetic silica infill of structural voids, late-stage
116 emplacement of dolomite veins, and dolomitic recrystallization of the carbonate host rock. To explore
117 the extent to which discrete diagenetic episodes may affect the composition of OM, Raman
118 spectroscopy was used to analyze and characterize OM (unrecognizable OM, microfossils, and distinct
119 taphonomic states) within the context of their diagenetic history. STXM mapping was subsequently
120 used to further characterize the organic chemistry of two coccoidal microfossils with distinct Raman-
121 signals to determine the extent to which spectral differences can be correlated with the chemical
122 composition of the organic microfossils. Our results indicate that small-scale variation in diagenetic

123 history, determined via changes in the petrographic framework of individual samples may have a
124 greater effect on variation in the maturity of OM than the composition of microbial precursor
125 materials.

126

127 **2. Geological background**

128 **2.1. Geologic description of the Angmaat Formation**

129 The Mesoproterozoic (~1.05 Ga; Gibson et al., 2018) Angmaat Formation, Bylot Supergroup, consists
130 of ~500 meters of unmetamorphosed and undeformed carbonate exposed within the fault-bounded
131 Borden Basin of northern Baffin and Bylot islands (Figure 1; Jackson and Iannelli, 1981; Kah et al., 1999;
132 Turner, 2009). Initiation of carbonate deposition within the basin is marked by sea-level rise,
133 restriction of terrigenous input into the basin and the formation of several discrete, deep-water
134 carbonate build-ups associated with fault-derived fluids (Hahn et al., 2015). This is succeeded, with
135 continued sea level rise, by carbonate ramp deposition that includes the laterally adjacent Angmaat
136 and Nanisivik formations (which, along with the underlying Iqqittuq Formation, were formerly termed
137 the Society Cliffs Formation; Turner, 2009). The Angmaat Formation is represented by a broad
138 microbial flat in the southeastern regions of the basin, bounded to the west by an oolitic shoal.
139 Periodic subaerial exposure of the oolitic shoal resulted in restriction and evaporation of associated
140 nearshore environments that are dominated by microbial dolostone, sea floor precipitates, and
141 abundant early diagenetic chert (Hofmann and Jackson, 1991; Kah and Knoll, 1996; Manning-Berg and
142 Kah, 2017; Manning-Berg et al., 2019). Northwest of the oolitic shoal, offshore deposits of the
143 carbonate ramp consist predominantly of finely laminated microbial dolostone and are referred to as
144 the Nanisivik Formation (Turner, 2009).

145 Chert is common in the Angmaat Formation, although microfossil-bearing chert occurs almost
146 exclusively within non-oolitic peritidal facies that are most prevalent southeast of the Milne Inlet
147 (Jackson and Iannelli, 1981; Hofmann and Jackson, 1991; Kah and Knoll, 1996). Microfossil-bearing chert

148 is typically black in color, and occurs as cm-scale lenses and nodules and semi-continuous decimeter-
149 scale beds that can be traced for >100 meters along outcrop exposures. An early diagenetic origin is
150 inferred from exquisite microfossil preservation (Kah and Knoll, 1996; Knoll et al., 2013), the
151 preservation of mesoscale microbial fabrics, and the reworking of lithified chert fragments in syn-
152 depositional high-energy deposits. Later diagenetic chert phases are typically yellow to grey to white
153 in color, and occur as smooth nodules that cross-cut bedding features. With rare exception (cf.
154 Hofmann and Jackson, 1991), these nodules have not been found to be microfossil-bearing.

155 The presence of at least two diagenetic stages of chert formation, synsedimentary and late-stage,
156 dolomitization of the host carbonate (Kah 2000), and the presence of quartz-bearing, cross-cutting
157 veins indicate a complex diagenetic history of Angmaat chert. Although the timing of discrete
158 diagenetic events is unknown, the time-equivalent Nanisivik Formation hosts Mississippi-Valley-Type
159 (MVT) deposits, that mark a clear episode of fluid flow, although primary deposition of MVT deposits
160 occurred >300 km northwest of chert-bearing strata of the Angmaat Formation (Turner, 2009). Fluid
161 inclusion data from ore materials suggest temperatures of 165-210 °C for the main ore body
162 (McNaughton and Smith, 1986; Arne et al., 1991), potentially reaching 313 °C where the ore body is
163 intersected by mid-Neoproterozoic intrusive dikes. The vast majority of late-stage mineralization,
164 associated with late-stage MVT deposition, however, occurred at temperatures only near 100 °C (Arne
165 et al., 1991; Hnatyshin et al., 2016). Relatively low temperatures of the majority of Angmaat diagenesis
166 is consistent with initial Raman analysis of OM within Angmaat cherts (Manning-Berg et al., 2019) that
167 suggest the presence of dominantly immature organic matter.

168 **2.2. Micropaleontology and mineral associations of Angmaat chert**

169 Organic microfossils are abundant in black chert of the Angmaat Formation and display large
170 taxonomic (Knoll et al., 2013) and taphonomic (Manning-Berg et al., 2019) variation. Preserved
171 microfossils and associated organic material are remnants of microbial mats that formed in peritidal
172 evaporitic, carbonate- rich environments. Within these environments, subaqueous and lower

173 intertidal environments are dominated by filamentous communities (Kah and Knoll, 1996) consisting
174 predominantly of sheaths of filamentous cyanobacteria, mainly *Siphonophycus capitaneum* (Nyberg
175 and Schopf, 1984; Knoll et al., 2013) and *Eomicrocoleus crassus* (Horodyski and Donaldson, 1980;
176 Nyberg and Schopf, 1984; Knoll et al., 2013). By contrast, more frequently exposed intertidal to
177 supratidal environments are characterized by an increase in abundance of coccoidal populations,
178 including *Eogloeocapsa bella* (Golovenok and Belova, 1984; Knoll et al., 2013), *Gloeodiniopsis* sp.
179 (Schopf, 1968; Knoll and Golubic, 1979), and the colonial coccoid *Eoentophysalis blecherensis*
180 (Hofmann, 1976).

181 Preserved microbial mats within Angmaat chert show both a range of taphonomic state, from well
182 preserved microfossils to unrecognizable organic matter. Previous Raman analysis showed similar
183 Raman spectra for organic microfossils of different taphonomic grade, consistent with taphonomic
184 processes via natural decomposition, rather than by post-depositional diagenetic conditions
185 (Manning-Berg et al., 2019). Angmaat chert, however, also preserve a variety of silicified and non-
186 silicified mineral phases (Manning-Berg and Kah, 2017). Carbonate strata of the Angmaat Formation,
187 for example, are fully dolomitized, and show evidence of primary precipitation of aragonite (Kah and
188 Knoll, 1996) and both fabric-retentive and fabric-destructive dolomitization (Kah, 2000). Within chert
189 phases, mats are indicative of more persistent subaqueous environments and commonly
190 interlaminated with silicified carbonate drapes and a variety of distinct, sub-mm to mm-diameter
191 voids (Knoll et al., 2013). Voids may represent structural elements within the mat that derive from
192 microbial gas bubble production (Knoll et al., 2013; Bosak et al., 2010), from the post-depositional
193 dissolution—and in rare cases, preservation—of mm-scale gypsum nodules (Kah, 2000), or from the
194 post-depositional dissolution of micritic drapes. By contrast, mats associated with peritidal to
195 supratidal environments are commonly associated with silicified aragonitic fans (Kah and Knoll, 1996;
196 Knoll et al., 2013), silicified gypsum (Kah et al., 2001), and rare occurrences of silicified halite (Kah et
197 al., 2001).

198

199 3. Background on Raman-spectroscopy of organic material

200 Raman spectra of organic material in sedimentary and metasedimentary rocks are generally
201 subdivided into a first-order (ca. 1200 – 1700 cm^{-1}) and a second-order region (ca. 2500 – 3000 cm^{-1})
202 of which the first order region, which shows two distinct maximum intensity regions at ca. 1350 cm^{-1}
203 and at ca. 1600 cm^{-1} , is most commonly used to determine the degree of alteration of OM (Beysac et
204 al., 2002; Beysac et al., 2007; Lahfid et al., 2010; Lünsdorf et al., 2014a and b). These peak regions,
205 commonly referred to as the G- and D- kerogen peaks include both primary and secondary peaks that
206 record changes in the carbon bonding (*sp*² and *sp*³ hybridization) within OM resulting from loss of
207 aliphatic *Sp*³ bonds and an increase in aromatic *Sp*² bonds—and ultimately the degree of organization
208 of aromatic features—during maturation. Primary peaks in this region are composed of a peak at 1580
209 cm^{-1} , commonly referred to as G-peak, that is caused by the in-plane E_{2g} stretching of graphitic carbon
210 bonds, and a peak at 1350 cm^{-1} , commonly referred to as D- (or D1-) peak, that reflects out-of-plane
211 vibration of these bonds (Wopenka and Pasteris, 1993; Ferrari and Robertson, 2000; Beysac et al.,
212 2002; Sforza et al., 2014).

213 Secondary peaks include the D2-peak at 1620 cm^{-1} that is caused by double resonance effects of
214 defects in the crystalline structure of graphite, a D3-peak at ca. 1500 cm^{-1} and a D4-peak at ca. 1250
215 cm^{-1} (expressed as shoulders of the 1350 cm^{-1} maximum), which are caused by out-of-plane defects,
216 tetrahedrally coordinated carbon, dangling bonds, and heteroatoms (Guedes et al., 2010; Lahfid et al.,
217 2010; Kouketsu et al., 2014; Ferralis et al., 2016). Additionally, in some analyses, the spectral region
218 around D4 (1100 – 1300 cm^{-1}) is further divided into two peaks at ca. 1180 cm^{-1} and 1250 cm^{-1} , referred
219 to as the D4- and D5-peaks, respectively, and the spectral area region of the D3-peak (ca. 1380 – 1560
220 cm^{-1}), which forms the minimum between the two main D- (D1-) and G-peaks. This region is divided
221 into two peaks at ca. 1420 cm^{-1} and ca. 1540 cm^{-1} , both referred to as the D3-peaks (Guedes et al.,
222 2010; Ferralis et al., 2016).

223 At low degrees of carbonization, the spectral maximum at 1600 cm^{-1} is dominantly caused by aromatic
224 ring-stretching vibrations, also known as “ π ” motion of polycyclic aromatic hydrocarbons while the
225 influence of the E_{2g} stretching bonds of graphitic carbon is minor (Mapelli et al., 1999; Mayo et al.,
226 2003; Schopf et al., 2005). This change in dominance often results in the use of a single peak solution
227 for the spectral maximum at ca. 1600 cm^{-1} of highly disordered OM, with the resulting peak
228 inconsistently named as D2-, D2+G- or G-peak (Guedes et al., 2010; Kouketsu et al., 2014; Ferralis et
229 al., 2016).

230 Within this scheme, the D1-, D2-, and G-peaks form the main components of Raman-spectra of highly
231 mature OM that experienced graphitization or higher carbonization (Beysac et al., 2002; Kouketsu et
232 al., 2014). Disordered OM that experienced moderate carbonization commonly preserve evidence of
233 the D3- and D4-peaks (Lahfid et al., 2010; Kouketsu et al., 2014). Highly disordered OM that
234 experienced low degrees of carbonization preserve a greater number of structural defects and
235 disorders, leading to preservation of a larger number of recognizable peak-shoulders around the 1350
236 cm^{-1} maximum including the D3- and D5-peaks (Guedes et al., 2010; Ferralis et al., 2016) and the use
237 of a single peak solution for the 1600 cm^{-1} maximum (Guedes et al., 2010; Kouketsu et al., 2014;
238 Ferralis et al., 2016).

239

240 **4. Samples and Methods**

241 Four samples of the Angmaat chert were analyzed in detail in this study (WWB-17-10, WWB-17-5, NL-
242 17-M and NL-17-N). The first two of these were obtained from the west shore of White Bay (WWB),
243 and the latter two from North Lake (NL; Figure 1; Table 1). All samples were collected from 3-10 cm
244 thick black chert beds intercalated with dolomitic carbonate. One standard petrographic thin section
245 of $30\text{ }\mu\text{m}$ thickness was prepared from each sample for microscopic and Raman-spectroscopic
246 examination, and two were prepared from sample WWB-17-5 (A and B). Petrographic microscopy was
247 performed to identify (1): the mineralogy of the samples (2): sedimentological and diagenetic features

248 and (3): organic material either preserved as organic microfossils or as unrecognizable organic
249 material (UOM) with UOM including all forms of OM that are preserved in the analyzed samples and
250 do not resemble or are not recognizable as distinct microfossils. Six double polished thin sections of
251 ca. 50 μm thickness mounted with sodium silicate to avoid possible contamination with epoxy resin
252 were prepared from sample WWB-17-5 for additional petrographic microscopy, Raman spectroscopy
253 and preparation of FIB-foils for STXM-mapping. Sodium silicate is soluble in water and therefore the
254 preparation procedure requires the use of ethanol for sawing and polishing while distilled water can
255 be used to dissolve the mounting agent when sample transfer to different sample holders is needed.

256 **4.1. Raman spectroscopy**

257 Raman spectroscopy was performed on polished thin sections using the LabRAM HR Evolution
258 instrument of the Department for Geosciences, Friedrich-Schiller-University Jena, Germany. This
259 instrument has a focal length of 800 mm, and is equipped with a 532 nm and a 633 nm laser. We used
260 a 600 l/mm grating and a 50 cm^{-1} cut-off edge filter combined with a 1024 x 128-pixel EM-CCD
261 detector. The central position of the spectrometer was set to 1350 cm^{-1} , recording the spectral region
262 from ca. 530 cm^{-1} to ca. 2100 cm^{-1} for all measurements with the 532 nm laser and from ca. 800 cm^{-1}
263 to ca. 1860 cm^{-1} for all spectra measured with a 633 nm laser. The technical resolution of the
264 instrument is 1.86 cm^{-1} for spectra acquired with the 532 nm laser and 1.3 cm^{-1} for spectra acquired
265 with the 633 nm laser. All acquired Raman spectra were calibrated for the Raman-shift (cm^{-1}) using an
266 internal calibration objective with an imbedded polymer. This calibration was applied prior to each
267 analytical session, after sample changes and changes of the setup like switching between lasers. We
268 used an exposure time of 15 - 30 s with two accumulations for single point measurements and for line-
269 maps of up to 20 points per line. The exposure time for area maps was 5 – 10 s per point with two
270 accumulations at each point of the map. All maps were performed with an excitation wavelength of
271 532 nm. The laser intensity on the sample was measured with a handheld laser power meter
272 “Coherent” from Edmund Optics. The maximum laser power on the samples surfaces was ca. 250 μW

273 for single point measurements and line-maps performed with a 532 nm laser and ca. 120 μ W for
274 measurements with a 633 nm laser. For the mapping performed with the 532 nm laser the power on
275 the sample surface was approximately 520 μ W. To avoid polishing effects, a 50X-VIS or 100X-VIS
276 objective was focused on OM below the surface of transparent mineral phases (quartz or dolomite).

277 i. Spectral treatment

278 All single point spectra were consequently treated using the curve fitting software Fityk to estimate
279 the maturation, to calculate H:C ratios, and to better understand maximum thermal alteration of the
280 analyzed OM. The baseline of each spectrum was corrected with a second-order polynomial
281 (Supplementary Figure 1). Because of the variable number of possible peaks (up to 7) the first order
282 Raman spectrum of disordered OM requires complex fitting procedures. Several protocols have been
283 developed to allow reproducible interpretations of Raman spectra of highly disordered OM (Sadezky
284 et al., 2005; Schopf et al., 2005; Lahfid et al., 2010; Kouketsu et al., 2014; Rouzaud et al., 2015; Delarue
285 et al., 2016; Ferralis et al., 2016). The protocols used in this study are described in detail below and a
286 summary is shown in Table 2. The precision of the fit of each spectrum was determined graphically by
287 subtracting the modeled spectra from the original spectra to obtain residual spectra (Supplementary
288 Figures 2 and 3).

289 Area maps were treated using LabSpec 6 first with a baseline correction using second order
290 polynomials and subsequently with classical least squares (CLS) fitting to define areas of similar
291 spectral characteristics.

292 Raman spectra recorded with an excitation wavelength of 532 nm were initially characterized without
293 using any peak-fitting procedure. The intensity values of the spectral maxima at ca. 1350 cm^{-1} and ca.
294 1600 cm^{-1} , the intensity at 1540 cm^{-1} and the full width at half maximum (FWHM) of the spectral
295 maximum at ca. 1600 cm^{-1} were extracted from all spectra. From these values the ratios I-1600/I-1350
296 and I-1540/I-1600 were calculated. The extracted values and calculated ratios were used to describe
297 and visualize the progressive changes of the spectral area between ca. 1520 and ca. 1620 cm^{-1} .

298 Additionally, the intensity ratio I-1600/I-1350 and the FWHM of the 1600 cm⁻¹ spectral maximum were
299 used for a first maturity estimate and to evaluate the needed peak-fitting method to calculate
300 maximum thermal alteration.

301 After the initial characterization a 4-peak fit was applied (Figure 2a and Supplementary Figure 2) that
302 allowed us to estimate the approximate maturation of OM and to calculate maximum thermal
303 alteration (Kouketsu et al., 2014). This procedure usually involves the use of Pseudo-Voigt functions
304 for spectral decomposition to avoid the breakdown of the use of Voigt functions for the decomposition
305 of Raman spectra of low mature OM (Kouketsu et al., 2014). However, because peak decomposition
306 with Pseudo-Voigt functions was largely inconclusive (Supplementary Figure 3) and because Pseudo-
307 Voigt functions are mostly used to model Voigt functions if they are not applicable the procedure was
308 performed using Voigt functions. For this procedure the spectral maximum at ca. 1600 cm⁻¹ was
309 treated as a single peak referred to as D2-peak. A D1 and D2 peak were set with starting positions at
310 ca. 1350 cm⁻¹ and ca. 1600 cm⁻¹ respectively. A D3 and D4 peak were set to fixed position at 1510 cm⁻¹
311 and 1245 cm⁻¹ respectively. The FWHM of D1 was then used to calculate maximum thermal overprint
312 wherein $T(D1) = -2.15(\text{FWHM-D1}) + 478$. The error of T(D1) is estimated with ca. ±30°C (Kouketsu et
313 al., 2014). A second geothermometer based on the FWHM-D2 was established by Kouketsu et al., 2014
314 but found to be less reliable. Therefore we refrained from reporting temperatures calculated with this
315 geothermometer.

316 We used a 5-peak fitting procedure (Figure 2b and Supplementary Figure 2) suitable for OM that
317 experienced a range of alteration reaching from moderate carbonization up to graphitization to
318 potentially estimate the degree of carbonization of OM from the Angmaat Formation (Sadezky et al.,
319 2005; Delarue et al., 2016). Spectra were decomposed as described in Delarue et al. (2016) using
320 Lorentzian/Gaussian functions into a D1, D2, D3, D4 and G band with the D1 band being fixed to the
321 maximum intensity of the D-area around 1350 cm⁻¹. This procedure requires a 2-peak fitting solution
322 for the spectral maximum at ca. 1600 cm⁻¹ with a G-peak at ca. 1580 cm⁻¹ and a D2-peak at ca. 1620

323 cm^{-1} . From this analysis we then extracted the intensity ratio $R1_{(sp)} = D1/G$ and the FWHM of the D1-
324 and G-peaks.

325 A seven-peak fitting procedure was then used to deconvolute the same Raman spectra (532 nm) into
326 discrete and recognizable peak maxima and shoulders (Figure 2c and Supplementary Figure 2) using
327 Voigt functions. Similar procedures were used previously to describe Raman spectra of low mature
328 organic microfossils (Schopf et al., 2005; Ferralis et al., 2016). The procedure includes the disorder
329 bands D1 and D2, here defined with positions at ca. 1340 cm^{-1} and ca. 1610 cm^{-1} respectively. We
330 applied a 2-peak solution for the D3 region with a band at ca. 1415 cm^{-1} and one at ca. 1540 cm^{-1} . A
331 D4 band is applied at ca. 1165 cm^{-1} and a D5 band at ca. 1230 cm^{-1} . A weak G band was added at ca.
332 1570 cm^{-1} . All bands were applied in the order they are listed above. After deconvolution we extracted
333 the FWHM-D1, the FWHM-D2 and the position of the G-peak and calculated the intensity ratio $R1_{(7p)}$
334 $= D1/D2$ and the intensity ratio $R3_{(7p)} = D3/D2$. The use of a particularly small G-peak in our
335 deconvolution procedure, consistent with the immaturity of OM in our samples, requires that we
336 define the intensity ratio $R1_{(7p)}$ as the intensity of the D1-peak divided by the intensity of the D2-peak
337 ($D1/D2$). This peak deconvolution procedure was used to visualize the progressive change of the
338 spectral maximum at 1600 cm^{-1} mainly represented by the D2- and G-peaks and the R3 ratio.

339 Spectra recorded with an excitation wavelength of 633 nm were fitted with the procedure described
340 in Guedes et al., (2010) and Ferralis et al. (2016). This procedure is similar to the described seven-peak
341 procedure and includes the peaks at similar starting positions (Figure 2d and Supplementary Figure 2).
342 The Raman band at 1600 cm^{-1} is treated with a single peak solution with the resulting peak named as
343 G-peak in Guedes et al., (2010) and as G+D2-peak in Ferralis et al., 2016. In this study the peak will be
344 referred to as (G+D2)-peak. The full width at half maximum of all peaks was restricted to a maximum
345 of 100 cm^{-1} . We extracted the intensity ratio $D1/(G+D2)$ and the FWHM-D1. The intensity ratios of
346 $D5/(G+D2)$ and of $(D4+D5)/(G+D2)$ obtained from this fitting procedure were used to calculate H:C

347 ratios of OM, wherein $H:C = 0.871 * D5/(G+D2) - 0.0508$ and $H:C = 0.6024 * (D4+D5)/(G+D2) - 0.0739$
348 (Ferralis et al., 2016).

349 **4.2. STXM**

350 Two ultrathin foils of ca. 20 x 15 x 0.12 μm were prepared using a FIB single-beam instrument at the
351 Institute de Physique du Globe de Paris (IPGP) following the procedure described by Wirth (2009) to
352 maintain textural integrity of sensitive materials. The foils were collected to intersect two coccoidal
353 organic microfossils ca. 4 mm apart in sample WWB-17-5 and analyzed by STXM mapping for the
354 chemical composition of the organic material. The foils were mounted on a copper half grid sample
355 holder using a platinum strap. STXM mapping of carbon was performed at the I08-SXM beamline at
356 the Diamond Light Source (UK).

357 Near edge X-ray absorption fine structure (NEXAFS) spectra were collected at the carbon K-edge from
358 275 to 320 eV on two FIB foils taken from a double polished thin section mounted on a glass holder
359 with sodium silicate to avoid contamination by epoxy resin. On the first foil an area of 5x5 μm , and on
360 the second an area of 6x6 μm was raster-scanned with the transmitted x-rays detected by a photo
361 diode at a fixed energy. The spot size was 66 nm and a dwell time of 10 ms per energy step per pixel
362 was used. Energy steps were set to 0.15 eV steps in the region of interest (283 – 300 eV) and to 0.5 eV
363 in pre- (275 – 283 eV) and post- (300 – 320 eV) regions. Received signals were converted to optical
364 density using incident signal (I_0) measurements from an adjacent, empty region of the image above
365 the carbon K-edge (284.5 eV). All data was processed with MANTIS (Lerotic et al., 2014) first by
366 principal component analysis and subsequently by cluster analysis to visualize potential chemical
367 zoning of carbon species within the mapped areas. Mantis was also used to normalize the carbon K-
368 edge spectra and subtract dark current. In both maps the NEXAFS spectra at the C K-edge were
369 deconvoluted using the software Fityk, following the procedure described in Bonneville et al. (2020)
370 and references therein. After background subtraction using a linear regression line over the range of
371 278 to 282 eV, the spectra were normalized to the area between 280 and 291.5 eV. Gaussian functions

372 were applied with a constant FWHM of 0.8 eV at fixed energy peak-positions (Centroid of the
373 Gaussian) that are representative for specific functional carbon groups (Supplementary Table 1). Two
374 indexes were extracted from the spectra, the aromaticity index (AI) that describes the contribution of
375 aromatic and olefinic carbons and the unsaturated index (UI) that describes the contribution of
376 unsaturated bonds between carbon and OH groups and carbon and heteroatoms like oxygen, nitrogen
377 (Bernard et al., 2012; Alleon et al., 2017). AI is defined as sum of the areas (A) of the Gaussian functions
378 between 284 eV and 285.4 eV ($AI = A_{284} + A_{284.4} + A_{284.9} + A_{285.4}$). UI is defined as the sum of the
379 areas (A) of the Gaussian functions between 285.8 eV and 286.6 eV normalized by AI ($UI = [A_{285.4} +$
380 $A_{286.2} + A_{286.6}]/AI$). These parameters are semi-quantitative with an uncertainty of $\pm 10\%$ that is
381 inherited from the normalization procedure.

382 **4.3. TEM-EDX**

383 FIB sections were inspected after STXM analysis using a FE-TEM (FEI Tecnai G2 FEG) equipped with an
384 Oxford 80 mm² energy-dispersive SDD X-ray detector and a Gatan UltraScan 2k CCD camera at the
385 Institute for Geosciences, University of Jena, Germany. Bright-field (BF) imaging and selected area
386 electron diffraction were performed in conventional TEM mode. EDX analysis was operated in
387 scanning TEM (STEM) mode in companion with high-angle annular dark-field (HAADF) imaging.
388 Furthermore, low angle annular dark-field (LAADF) at long camera length STEM mode was used to
389 image the diffraction contrast of the entire FIB foils at low magnification. TEM analysis was performed
390 to check for photodeposition of organic matter after STXM and to characterize the textural relations
391 between organic material and mineral matrix of the analyzed materials.

392

393 **5. Results**

394 **5.1. Mineralogy and petrology**

395 Petrographic microscopy shows that the analyzed samples are predominantly composed of chert and
396 dolomite with accessory pyrite and iron oxide phases. Chert forms the majority of the sampled

397 material, although samples contain subordinate dolomite as discrete laminae and fracture filling
398 material as indicated by the distribution of the elements that form these minerals (Supplementary
399 Figures 4 and 5). Pyrite is present as euhedral or subhedral grains <100 μm in size within the chert
400 matrix, and iron oxides are primarily associated with dolomite laminations as thin films along laminae
401 and crystal boundaries. Fracture-filling secondary dolomite is free of iron-oxide phases. Detrital
402 material is sparse, with only a few ca. 200 μm large well-rounded quartz-grains. Occasionally, the
403 presence of mm-scale angular chert clasts with a similar fabric to the surrounding chert matrix
404 supports previous observation of syndepositional silicification and penecontemporaneous reworking.
405 Samples record both laminated or nodular chert, with a variety of organic microfossils primarily within
406 the chert phase.

407 Sample WWB-17-10 consists of mm-thick interlaminations of chert and dolomite. Chert laminae
408 contain abundant filamentous sheaths of ca. 25 μm diameter (Figure 3a) attributed to *Eomicrocoleus*
409 (Horodyski and Donaldson, 1984; Knoll et al., 2013). UOM is ubiquitous in both chert and dolomite
410 laminations (Table 1). Two samples (NL-17-M and NL-17-N) show planar to wavy mm-scale laminae,
411 with subordinate 1 mm diameter chert nodules (Table 1). Both samples contain predominantly 15 -
412 30 μm diameter coccoidal microfossils recognized as *Eogloeocapsa* (Golovenok and Belova, 1984;
413 Figure 3b), and rare, fragmented 3 μm diameter filamentous sheaths (Figure 3c). UOM is ubiquitous
414 within chert and dolomite in both samples. Finally, sample 17-5 preserves a network of <2 mm nodules
415 interspersed within dolomite matrix (Table 1). Microfossils are predominantly coccoidal, especially
416 *Gloeodiniopsi* species (Schopf, 1968; Knoll and Golubic, 1979) that vary from 10 μm to 40 μm in
417 diameter (Figure 3d). Filamentous microfossils are rare and often poorly preserved (Figure 3e). UOM
418 is ubiquitous in both chert and dolomite phases but the majority is accumulated in secondary pore
419 spaces between nodules (Figure 3f).

420 The most apparent difference between laminated and nodular chert fabrics is the porosity. Laminated
421 chert is typically dense and preserves only micrometer scale pore-spaces; nodular chert in contrast,

422 contains pore-spaces as large as 3 mm in diameter. Despite these differences, all samples show a
423 similar range of diagenetic fabrics, with alternating dominance of specific features between samples.
424 In all samples, both dolomite and chert are microcrystalline, with crystal sizes < 50 μm (Figure 4a, b).
425 Chert often preserves a microfabric that consists of chalcedony spherules (Dunham and Kah, 2018;
426 Figure 4c). Nodular chert preserves numerous pseudomorphs after dolomite (Figure 4d). Samples
427 containing nodular chert also record pore spaces between nodules that can be as large as the
428 surrounding nodules. This void space is commonly filled by UOM and can contain discrete chert
429 spherules that might represent late-stage silica growth in void space (Figs 3e and 4e, f). Chert
430 spherules are ca. 20 μm in diameter and can coalesce to form nodules up to 1 mm in diameter (Figure
431 4e). These nodules preserve UOM and dolomite pseudomorphs (Figure 4f) but do not show
432 preservation of discrete microfossils or contain spherules with coatings of organic material. Laminated
433 chert does not contain chert spherules.

434 In contrast, laminated chert contains evidence for primary void space (up to 5 mm diameter) that has
435 been filled with dolomite, chalcedony and mega-quartz (Figure 5a and b). Such void spaces contain
436 botryoidal, inward growing chalcedony (Fig. 5). Void spaces commonly show zoning with an outer edge
437 composed of fine-grained (< 50 μm), partly silicified dolomite, followed by a ca. 300 μm thick zone of
438 chalcedony, and a central filling of mega-quartz crystals (Figure 5a and b). Chalcedony lining primary
439 voids is often intergrown with varying amounts of UOM. Most voids show organic staining that
440 highlights radial growth patterns of void lining chalcedony (Figure 5c), some contain substantial OM
441 that appears as a black mass overprinting chalcedony lining (Figure 5d). Microfossils are generally not
442 preserved in void -lining chalcedony, with the rare exception of a few voids in sample WWB-17-5 that
443 contain filamentous microfossils that appear to protrude into the former void spaces (Figure 5c).
444 Central void fillings of mega-quartz, or more rarely dolomite, contain no organic material.

445 Fractures that crosscut chert are generally thin in laminated chert, and mostly without secondary
446 fillings; some contain secondary dolomite or UOM. Veins within nodular chert are wide and filled by

447 secondary euhedral dolomite, in places with crystals as large as 500 μm (Figure 6a and b). These larger
448 dolomite crystals grew often into interstitial space between nodules and incorporated late-stage chert
449 spherules as solid inclusions (Figure 6a and b). Some dolomite crystals that formed in contact with
450 chert nodules preserve spherical structures that preserve faint internal textures and might represent
451 coccoidal microfossils or chert spherules coated by organic carbon (Figure 6c; Supplementary Figure
452 6). Euhedral dolomite that formed as a late-stage fill within voids occurs primarily in close proximity
453 to fractures.

454 Chert also occurs as mixed-phase nodules within dolomitic regions. In these instances, dolomite shows
455 partial silicification resulting in a mixed fabric of equally small ($< 50 \mu\text{m}$) dolomite and chert crystals
456 (Figure 6d) or in full replacement of the inner zone of a nodule by radially aligned chalcedony and
457 mega-quartz resembling void fillings in chert (Figure 6e). Organic material is ubiquitous as thin films
458 between crystals and often as slightly thicker and darker films between nodules or laminae (Figure
459 6e). Secondary dolomite is easily recognizable by its larger crystal size and its brighter appearance due
460 to the lack of OM in its growth fabric (Figure 6f). Occasionally, stylolites can be observed in dolomite
461 lamination forming ca. 20 μm thick anastomosing dark traces filled by UOM (Figure 6f). No microfossils
462 are preserved in dolomite beds.

463 **5.2. Diagenetic sequence**

464 Observations highlighted in the previous section provide evidence of multiple, discrete episodes of
465 mineralization that represent fluid interaction from early through late-stage diagenesis (Figure 7).
466 Initial silicification occurred penecontemporaneous with deposition and represents both the primary
467 mineralization of microbial mats and the replacement of synsedimentary mineral phases, including
468 dolomite, gypsum, and halite (see also Kah et al., 2001; Knoll et al., 2013; Manning-Berg and Kah,
469 2017). Initial silicification is the primary phase responsible for well-preserved microbial remains.
470 Laminated chert, containing mainly filamentous microbial mats, contains evidence for primary
471 constructional voids (Figure 5a, b; Knoll et al., 2013; Manning-Berg and Kah, 2017). Voids are lined

472 with isopachous chalcedony that transitions, with increasing crystal size to void-filling mega-quartz,
473 suggesting continued silica precipitation from a single fluid source. In contrast voids within nodular
474 chert reflect creation of porosity during silicification or associated diagenetic processes. These voids
475 are commonly filled with UOM and less frequently lined with chalcedony (Figure 5c). That signifies
476 either in-situ organic decomposition or later migration of organic-rich fluids. Substantial incorporation
477 of UOM into void-lining chalcedony (Figure 5d) indicates silica precipitation that post-dates the
478 primary microfossil-bearing silica phase. Discrete, optically clear chalcedony spherules that displace
479 UOM within these voids may be associated with this secondary silica precipitation event. Chalcedony
480 spherules are observed as solid inclusions within euhedral, late-stage dolomite (Figure 6a, b)
481 associated with fractures that formed during burial diagenesis. Stylolites observed in these samples
482 also represent fluid interaction during burial diagenesis. Termination of late-stage, dolomite-filled
483 fractures at stylolites indicates that stylolite formation is the final diagenetic stage.

484 **5.3. Raman spectroscopic results**

485 Using the 532 nm laser, we recorded 339 single point Raman spectra of organic microfossils and UOM
486 involved in all previously described diagenetic processes. We also recorded 12 line-maps on individual
487 microfossils and 6 area maps of small microfossil populations and individual microfossils. The Raman
488 signal of preserved OM from the Angmaat formation is highly variable, and variation is clear even prior
489 to peak fitting by a visual comparison of Raman spectra (Figure 8). Two distinct spectral shapes (S1
490 and S4) can be recognized, with multiple recorded spectra of each shape. A similarly large number of
491 spectra have intermediate shapes that indicate transitional states between the two end-members.
492 These intermediate states have been roughly categorized into two groups S2 and S3 (Figure 8). The
493 two most identifiable differences in the spectral shapes are a change in the intensity ratio of the 1350
494 cm^{-1} (D1) and the 1600 cm^{-1} (D2/G) spectral region, and a substantial change of the width of the 1600
495 cm^{-1} spectral region (Figure 8). Notably spectral shape S4 was only recorded from coccoidal
496 microfossils of sample WWB-17-5, whereas S1, S2 and S3 spectral shapes were measured in all
497 samples, although one specific shape tended to dominate within individual samples.

498 i. 532 nm laser-based results

499 The Raman spectra of OM show large variations of extracted values and ratios. Several of these
500 parameters were obtained before any peak fitting procedure was applied, and could be used to decide
501 on the exact peak fitting strategy. The intensity ratio I-1600/I-1350 varies between 1.19 and 1.89
502 while the intensity ratio I-1540/I-1600 varies from 0.14 to 0.59. The FWHM-D2 ranges from 41.8
503 cm^{-1} to 79.4 cm^{-1} (Table 3). High I-1600/I-1350 ratios coincide with low FWHM-D2 (Figure 9a) and low
504 I-1540/I-1600 ratios with the best correlation appearing between the FWHM-D2 and the I-1540/I-1600
505 ratio (Supplementary Figure 7). Values of the intensity ratio I-1600/I-1350 above 1.5 indicate that a 4-
506 peak fitting procedure needs to be used to calculate paleo-temperatures (Kouketsu et al., 2014).
507 Spectra with ratios below 1.5 show FWHM-D2 values above 60 cm^{-1} that also indicate low maturity
508 that requires the use of the same 4-peak fitting procedure.

509 Using the 4-peak fitting procedure (G) of Kouketsu et al. (2014), the FWHM of D1 ranges from 101.63
510 to 138 cm^{-1} , and the FWHM of D2 from 36.41 to 79.9 cm^{-1} . Temperatures calculated using the FWHM-
511 D1 span between ca. 180°C to 260°C (Table 3, Figure 9b).

512 Using the 5-peak fitting procedure of Delarue et al. (2016), the $R1_{(5p)}$ ratio (Table 2) ranges from 1.06
513 to 2.03; the FWHM of D1 ranges from 110.9 cm^{-1} to 148.7 cm^{-1} and the FWHM of G ranges from 32.9
514 cm^{-1} to 126.35 cm^{-1} (Table 3). High $R1_{(5p)}$ ratios coincide with high FWHM-D1 and FWHM-G values. The
515 correlation of the $R1_{(5p)}$ ratios with the FWHM-G values is better pronounced than its correlation to
516 the FWHM-D1 values (Figure 9c, d).

517 Using the 7-peak fitting procedure, the $R1_{(7p)}$ ratio ranges from 0.53 to 1.05, the $R3_{(7p)}$ ratio (Table 2)
518 ranges from 0.14 to 0.59; and the FWHM-D1 and FWHM-D2 range from 80.5 cm^{-1} to 122.5 cm^{-1} and
519 from 32.0 cm^{-1} to 67.5 cm^{-1} , respectively (Table 3). The position of the G-peak obtained in the 7-peak
520 fitting procedure is also highly variable and occurs between 1551.2 cm^{-1} to 1578.5 cm^{-1} (Table 3). High
521 $R1_{(7p)}$ ratios coincide with high FWHM-D1 and high FWHM-D2 values (Figure 9e, f); and low $R3_{(7p)}$ ratios

522 coincide with low FWHM-D2 values (Figure 9g) and higher wavenumbers of the G-peak position
523 (Supplementary Figure 8).

524 ii. 633 nm laser-based results

525 Using the 633 nm laser, 171 single point spectra of both, discrete microfossils and UOM, were
526 recorded on sample WWB-17-5 to calculate H:C ratios and estimate the maturity of organic
527 microfossils. Spectra are assigned to the same categories as for the 532 nm Raman-spectra (Tables 3
528 and 4). Higher H:C ratios correspond to less mature OM while lower H:C ratios correspond to more
529 mature OM. H:C ratios calculated by using $D5/(G+D2)$ intensity-ratios are slightly higher (0.32-0.41)
530 than H:C ratios calculated by using $(D4+D5)/(G+D2)$ intensity-ratios (0.28-0.38). The highest H:C ratios
531 are calculated for UOM (Table 4; Figure 10), and the lowest ratios are calculated for coccoidal
532 microfossils that show the spectral shape S4 of 532 nm spectra (Table 4; Figure 10). Standard
533 deviations show large differences in their values between the defined types of OM. Coccoidal
534 microfossils have been subdivided according to the shape of the recorded spectra (S1 and S4) and
535 show SD between 0.036 and 0.025. A subdivision of organic matter populations by host mineral
536 (coccooids in chert or SOS in dolomite) results in SD as high as 0.054 (Table 4; Supplementary Table 2).
537 The intensity ratio $D1/(G+D2)$ reaches from 0.72 to 1 and the FWHM-D1 from 81.18 to 92.3 cm^{-1} (Table
538 4). High $D1/(G+D2)$ ratios coincides with high values of the FWHM-D1 (Figure 10c).

539 iii. Variations in OM between and within samples

540 In order to better understand the observed variation of the Raman spectra of OM we sorted spectra
541 by sample, by their general taxonomy (filaments vs. coccooids), and by diagenetic context (i.e., their
542 association with mineral phases) and, for sample WWB-17-5, by spectral shape (Table 3). Considering
543 the full set of samples, the variation between Raman spectra of OM is substantial. Individually
544 however, each sample shows a smaller range of variation amongst discrete types of OM (Table 3;
545 Figure 9 and 10). Variation between spectral measurements within discrete types of OM is mostly
546 negligible with exception of OM within sample WWB-17-5, which shows significant overlaps within

547 specific types of OM. Most apparent are the listed differences in maturity of OM between coccoidal
548 microfossils (Table 3). Raman spectroscopic line-maps from individual microfossils however, do not
549 show intra-target variation (Figure 11a – h).

550 Sample WWB-17-10 contains both filamentous microfossils (filaments) and unrecognizable organic
551 matter embedded in chert (UOM-chert). Extracted Raman parameters from these two types of OM
552 show similar values except for intensity ratios I-1600/I-1350, $R1_{(5p)}$ and $R1_{(7p)}$ (Table 3). The calculated
553 maximum thermal alteration of these two types of OM is similar with $T(D1) = 255$ and 242°C (Table 3;
554 Figure 9b).

555 Sample NL-17-M contains coccoidal microfossils (coccoids), free unrecognizable organic matter
556 (UOM), UOM embedded in secondary chalcedony (UOM-chc) and in chert spherules (UOM-sph).
557 Variation among the Raman proxies of different types of OM in this sample are substantial with
558 particularly large variation of the FWHM-D1 and -D2 parameters that were extracted from the 4-peak
559 fit. Variation between UOM and UOM-sph occur at μm -scale where spherules formed within UOM
560 filled pore spaces, wherein OM trapped as inclusions within spherules shows a different Raman signal
561 than OM surrounding the spherules (Figure 11i, j). However, OM inclusions within chert spherules are
562 small and rarely observed. The calculated maximum thermal alteration $T(D1)$ varies between ca.
563 180°C for UOM and ca. 230°C for coccoidal microfossils (Table. 3; Figure 9). The lowest calculated
564 temperatures of the whole set of samples are from sample NI-17-M.

565 Sample NL-17-N contains ubiquitous UOM, coccoidal microfossils (coccoids) and filamentous
566 microfossils (filaments) all preserved in chert. Variation between the Raman proxies of all types of OM
567 are generally low (Table 3). The calculated maximum thermal alteration $T(D1)$ varies between 207°C
568 for filamentous microfossils and 224°C for UOM-chert (Table. 3; Figure 9).

569 Sample WWB-17-5 contains free UOM, mostly occurring as black masses in pore spaces (Figure 3f, 4e
570 and 5c), coccoidal microfossils embedded in chert (cod-chert), spherical organic structures (SOS)
571 embedded within secondary vein-filling dolomite (cod-dol), and filamentous microfossils embedded

572 in chert and chalcedony (filaments). Filaments embedded in chert and chalcedony were not treated
573 separately due to their rarity in this sample (Table 3). The 4 types of OM described here display roughly
574 two different degrees of alteration with filamentous microfossils and UOM both showing low maturity
575 while coccoidal microfossils and SOS in dolomite can display both alteration states high and low
576 mature. The calculated maximum thermal alteration T(D1) of filamentous microfossils and UOM is
577 approximately 230°C, just slightly lower than that of coccoidal microfossils in chert and SOS in
578 dolomite with a temperature of ca. 250°C (Table 3; Figure 9b).

579 Coccoidal microfossils in Sample WWB-17-5 can also be divided according to the basic spectral shape
580 (S1 and S4; Figure 10). Such division results in calculated differences in maturity that are larger than
581 the variation observed across all other samples (Table 3; Figures 9). Coccoidal microfossils with the
582 spectral shape S1 show similar Raman proxies and maximum thermal overprint (T(D1) ~230°C) as UOM
583 and filamentous microfossils. Coccoidal microfossils with the spectral shape S4 show Raman proxies
584 that correspond to the highest calculated maximum thermal overprint of the whole set of samples
585 (T(D1) ~260°C). The observed variation in spectral shape, and subsequently in extracted Raman-
586 proxies can occur within a spatial distance of only a few μm and between OM of the same and of
587 different types (Figure 12).

588 **5.4. STXM results**

589 Two coccoidal microfossils from a double polished thin section of sample WWB-17-5 were selected
590 for STXM analysis based on their contrasting Raman signals and their taxonomic and taphonomic
591 appearance. The two microfossils are approximately 4 mm apart (Figure 13a), both spherical with a
592 diameter of ca. 40 μm , and appear uniformly dark in light microscopy (Figure 13b and c). The uniformly
593 dark appearance does not allow for the identification of internal cellular structures but ensures that
594 the amount of OM within the produced FIB cuts was maximized. The identification of these two
595 structures as microfossils and not as structures such as carbon coated chert spherules is based on: (1)
596 Their size of ca. 40 μm diameter is conform with the size of individuals of *Gloeodiniopsis sp.* while

597 chert spherules are ca. 20 μm in diameter. (2): The chosen microfossils are imbedded in chert nodules.
598 Chert nodules do not contain chert spherules with the exception of nodules that are entirely
599 composed of chert spherules. However, nodules composed of chert spherules do not preserve organic
600 microfossils. (3): The chosen coccoidal microfossils resemble individuals identified as *Gloeodiniopsis*
601 *sp.* and microfossil-A is part of a small colony of this species while microfossil-B is situated next to a
602 neighboring individual of *Gloeodiniopsis sp.* that shows internal cellular structures (Supplementary
603 Figure 9). Within this sample, one microfossil records the Raman spectral shape S1 (microfossil-A) and
604 the other records the Raman spectral shape S4 (microfossil-B; Figure 13d). Raman analyses at 633 nm
605 implies a large difference in their H:C ratios (Figure 13d, e).

606 NEXAFS spectra of the two mapped areas show significant differences, specifically of the intensity of
607 the aromatic spectral range (284 – 285.4 eV) relative to that of ketones and phenols (286.2 – 287.1).
608 The intensity of the NEXAFS spectral region representative for aromatic groups is lower in microfossil-
609 A than in microfossil-B (Figure 14; Supplementary Figure 10). The aromaticity index (AI) of microfossil-
610 A is 0.136, the unsaturated index (UI) is 0.955 (Supplementary Figure 10). Microfossil B shows an AI of
611 0.252 and an UI of 0.699 (Supplementary Figure 10). Cluster analysis indicates that the mapped area
612 of microfossil-A shows limited chemical zoning (Figure 14a). The majority of the mapped area shows
613 approximately equal intensities of the spectral range of aromatic groups and the spectral range of
614 ketones and phenols with the occurrence of some micro- to nano-inclusions that show a weak signal
615 in the aromatic range (Figure 14). In turn cluster analysis of the mapped area of microfossil-B indicates
616 a homogeneous composition of OM that is most apparent by the similarity of the resulting spectra
617 and the undefined edges of the different cluster (Figure 14a).

618 **5.5. TEM-EDX results**

619 EDX mapping and HAADF imaging was performed equivalent to the area mapped by STXM in
620 microfossil-A (Figure 15a). The FIB-foil of microfossil-B experienced physical damage after STXM
621 analysis and prior to TEM analysis and the area mapped by STXM was lost. Consequently, TEM analysis

622 was performed on the remaining part of the foil adjacent to the area mapped by STXM (Figure 15b).
623 The position of the FIB-foil in relation to the probed microfossil indicates that the foil is fully composed
624 of microfossiliferous material (Figure 13c). Both FIB-foils are composed of a homogeneous micro- to
625 nano-crystalline matrix with crystal sizes of ca. <200 nm and low porosity. Obtained diffraction
626 patterns and EDX mapping show that the mineral matrix is composed of polycrystalline quartz (Si+O)
627 with minor, homogeneously distributed portions of carbon (C) that form most likely thin films on
628 quartz surfaces and at pore walls (Figure 15 c, d and Supplementary Figure 11). Additionally, the FIB-
629 foils show sporadic coverage by < 100 nm large salt crystals (bright dots in HAADF image of Figure
630 15d), most likely a result of the preparation with sodium silicate that included repeated transfers of
631 the samples to different sample holders by dissolving the mounting agent in distilled water.

632

633 **6. Data interpretation**

634 Several deconvolution protocols with changing numbers of peaks (up to 6) have been developed to
635 allow for reproducible interpretations of Raman spectra of highly disordered OM (Sadezky et al., 2005;
636 Schopf et al., 2005; Guedes et al., 2010; Lahfid et al., 2010; Kouketsu et al., 2014; Delarue et al., 2016;
637 Ferralis et al., 2016). This requires adaptable fitting procedures to characterize the degree of alteration
638 or maturity of OM and to visualize differences in maturation of OM in geological samples relative to
639 each other.

640 **6.1. Maturity estimation based on 4-peak fitting**

641 Of the three fitting procedures we used for spectra acquired with a 532 nm laser, the 4-peak fitting of
642 Kouketsu et al. (2014) is the best-known method to estimate the maximum thermal alteration of
643 generally immature OM (i.e. temperatures of alteration between 150 – 400°C). A first evaluation of
644 the Raman proxies I-1600/I-1350 and FWHM-D2 provides evidence to determine the exact peak-fitting
645 procedure required for calculation of peak-temperatures (Kouketsu et al., 2014). Highly disordered
646 OM usually shows I-1600/I-1350 ratios > 1.5 and an increase of the FWHM-D2 with increasing degree

647 of disorder. Such trends are recorded in both Phanerozoic rocks (Kouketsu et al., 2014) and
648 Proterozoic organic microfossils (Baludikay et al., 2018; Pang et al., 2020). However, OM of low
649 maturity from Proterozoic organic microfossils is also known to show I-1600/I-1350 ratios < 1.5 that
650 coincide with FWHM-D2 values above 60 cm⁻¹ (Qu et al., 2015; Pang et al., 2020). Such OM still needs
651 to be treated with the G-fitting described in Kouketsu et al., 2016.

652 OM from the Angmaat Formation shows a trend similar to that of low mature Proterozoic organic
653 microfossils (Qu et al., 2015; Pang et al., 2020). All spectra that show the spectral shape S1 and S2
654 have I-1600/I-1350 ratios < 1.5, as low as 1.21, despite increasing FWHM-D2 values (Table 3; Figure
655 9a). The unusually high FWHM-D2 values but relatively normal T(D1) temperatures suggest that
656 spectra with the peak shapes S1 and S2 display highly disordered OM, possibly of an unusual chemical
657 composition of OM that results in a spectral maximum at 1600 cm⁻¹ with an unusually high relative
658 width and low relative intensity. However, although the temperatures obtained with the T(D1)
659 geothermometer appear relatively normal with ca. 260°C - 180°C, deviation from expected trends
660 (Figure 9a) does not permit for an exact estimate of the thermal alteration of the OM of the lowest
661 maturity.

662 **6.2. Maturity estimation based on 5-peak fitting**

663 An even more apparent deviation from expected alteration paths appears when using the 5-peak
664 fitting procedure of Delarue et al. (2015). This procedure allows visualization of the OM maturation
665 pathway (carbonization or graphitization) by plotting the intensity ratio R_{1(5p)} against FWHM-D1
666 (Delarue et al., 2016). With an increasing degree of carbonization, the FWHM-D1 decreases while the
667 R_{1(5p)} ratio increases. When carbonization shifts to graphitization, the values of FWHM-D1 are
668 approximately < 40 cm⁻¹ and the R_{1(5p)} ratio starts to decrease again (Rouzaud et al., 2015; Delarue et
669 al., 2016). Disordered OM that experienced lower degrees of carbonization typically shows low R_{1(5p)}
670 ratios (<1) and high FWHM-D1 values (>100 cm⁻¹). OM from the Angmaat Formation shows FWHM-D1
671 values >110 cm⁻¹, as expected, but also shows unusually high R_{1(5p)} ratios > 1.21 even up to 2.03 (Figure

672 9c). Only Raman spectra with a peak shape S4 provide data that correspond to the expected
673 carbonization path (Figure 9c). An estimate of the degree of carbonization can also be made using the
674 FWHM-G instead of the FWHM-D1 where the FWHM-G decreases while the $R1_{(5p)}$ ratio increases with
675 increasing degree of carbonization (Delarue et al., 2016). OM from the Angmaat Formation however,
676 shows a trend, oblique to that expected, where the $R1_{(5p)}$ ratios decrease with decreasing FWHM-G
677 values (Figure 9d). Deviation of the extracted Raman proxies from previously predicted maturation
678 pathways does not allow for a consistent estimate of the maturity of OM from the Angmaat
679 Formation.

680 **6.3. Maturity estimates based on 633 nm results**

681 Organic microfossils of the Angmaat formation show estimated H:C ratios between 0.41 and 0.29
682 (Figure 10; Table 4) as typical for OM that experienced lower carbonization equivalent to that in the
683 zone of gas formation (Vendenbroucke and Largeau 2007). The intensity ratio $D1/(G+D2)$ and the
684 FWHM-D1 extracted from these spectra are also similar to those of collotelinite of coal from the Penn
685 State Coal Bank (Figure 10c; Guedes et al., 2010) indicative of highly disordered OM with low maturity.

686 **6.4. Raman and STXM**

687 Overall, Raman spectroscopic methods show that spectra of OM from Angmaat Formation chert are
688 consistent with highly disordered OM of low maturity that is highly variable between samples and
689 within samples. The highest maturity is detected in coccoidal microfossils from sample WWB-17-5,
690 which appear to have undergone moderate carbonization with a maximum thermal alteration of ca.
691 260°C. The lowest mature OM occurs in UOM of sample NL-17-M, which likely experienced a
692 maximum thermal overprint of ca. 180°C. However, the OM in this sample and OM of similarly low
693 maturity from other samples deviates from established measures of alteration (Figure 9a-d). Standard
694 analysis of Raman spectra does not explain the maturation processes or chemical differences that
695 caused these variations. STXM mapping and subsequent cluster-analysis reveal distinct differences in
696 chemical composition of organic microfossils that record the S1 and S4 end member shapes of Raman

697 spectra. Specifically, we find that NEXAFS spectra of organic microfossils of low maturity (Raman shape
698 S1) within Angmaat chert show lower amounts of aromatic groups in relation to phenols and ketones
699 whereas NEXAFS spectra of more highly mature organic microfossils (Raman shape S4) that are more
700 consistent with established maturation pathways defined by Raman spectra show higher amounts of
701 aromatic groups in relation to phenols and ketones (Figure 14).

702 **6.5. Effect of chemical variation on Raman spectra**

703 The observed differences in the ratio of aromatic groups relative to ketones and phenols could
704 potentially explain the differences in the Raman spectra. Raman active vibrations associated with
705 stretching and shear modes of aromatic groups cause an intense Raman response around 1600 cm^{-1}
706 (Mapelli et al., 1999; Mayo et al., 2003). Most phenolic compounds have a less intense Raman
707 response at ca. 1600 cm^{-1} . However, the intensity of the Raman response in this spectral area varies
708 strongly between different phenolic compounds independent of their bonding to single or polycyclic
709 aromatic groups (Pompeu et al., 2018). Raman active vibrations of ketones show an extremely weak
710 Raman response at 1600 cm^{-1} and a strong signal in the area between ca. 1560 and 1580 cm^{-1} (Forrest
711 et al., 1976). Relatively low intensities and high widths of the 1600 cm^{-1} maximum of Raman spectra
712 of low mature OM accompanied by high intensities of the D3 area (ca. 1540 cm^{-1}) as observed here
713 would therefore potentially reflect a decrease of aromatic groups in a mixture of organic compounds.
714 STXM-NEXAFS spectral results indicate that the described Raman-spectral properties are linked to a
715 relatively low amount of aromatics while the relative amount of ketones and phenols is high (Figure
716 14a, b). This implies that the spectral properties of the Raman spectral maximum of OM at ca. 1600
717 cm^{-1} in relation to the spectral area around 1540 cm^{-1} can be used to determine the degree of
718 aromaticity. However, since phenolic and ketonic compounds can also be coupled to aromatic groups
719 and the UI index describes the contribution of unsaturated bonds between carbon and OH groups or
720 heteroatoms (Bernard et al., 2012; Alleon et al., 2017) the described Raman-spectral variation could

721 also indicate differences in the H:C, O:C or N:C ratios similar to the relation shown between H:C ratios
722 and the intensity of the pre-1350 cm^{-1} area of Raman spectra of low mature OM (Ferralis et al., 2016).
723 In all used peak fitting procedures, the FWHM-D2 shows a better linear correlation to the
724 corresponding intensity ratio R1 than the FWHM-D1 and a single-peak solution for the 1600 cm^{-1}
725 maximum achieves a better correlation than a 2-peak solution (Figure 9). Such spectral differences are
726 also apparent in the 7-peak procedure (Figure 9e-f) where the FWHM-D2 of the D2-peak shows a
727 strong linear correlation with the R3 ratio (Figure 9g), the position of the G-peak or even the I-1540/I-
728 1600 ratio (Supplementary Figure 8b, c). Here the FWHM-D2 is clearly used as general measure for
729 the width of this spectral area while R3 and the position of the G-peak both constrains the changing
730 left-sided asymmetry of the 1600 cm^{-1} spectral area (Figure 8) and allows for a precise estimate of a
731 possible maturation path based on the degree of this asymmetry vs. the width of D2 (Figure 9g). The
732 appearance of the same linear correlation with the use of the I-1540/I-1600 ratio indicates that this
733 relation is truly originated from the obtained spectra and not an artefact of the used peak-fitting
734 procedures. Although this study includes only two valid STXM-NEXAFS measures and does therefore
735 not allow for a direct correlation between the displayed Raman parameters and the NEXAFS-based AI
736 and UI it appears reasonable that the Raman parameters of the D2- and D3-peaks can potentially be
737 used as measure for aromaticity and the contribution of unsaturated bonds between carbon and OH
738 groups or heteroatoms in highly disordered OM.

739

740 **7. Discussion**

741 Our results show large variations of the Raman signal of OM both between samples and within
742 samples, between organic microfossils of different taphonomic grades, between microfossils of
743 different taxonomy and between microfossils of the same taxonomy (Table 3). These variations are
744 reflected in the degree of maturation (Figure 9), in calculated H:C ratios (Figure 10) and in the chemical
745 composition of organic microfossils (Figures 14 and 15). Our observations imply that preserved OM,

746 and specifically OM associated with preserved microfossils in sedimentary rocks do not necessarily
747 become homogenized during early diagenesis. However, despite the observed chemical differences
748 between discrete microfossils it is not clear what mechanism underlies these differences. The
749 observed deviation from the traditional carbonization path could be caused by a number of processes
750 including, but not limited to: (1) the structural ordering of OM along the surfaces of authigenic mineral
751 phases (2) potential differences in organic precursor materials (e.g. prokaryotic vs. eukaryotic); (3) or
752 chemical ordering of OM caused by localized fluid flow and preferential migration of soluble organic
753 components.

754 **7.1. Physical-structural ordering**

755 The maturity of organic material in rocks can vary on the micro- and nano-scale due to alignment
756 around authigenic minerals such as quartz and chlorite (Bustin et al., 1995; van Zuilen et al., 2012; Qu
757 et al., 2020). However, such ordering is typically linked to intense hydrothermal circulation and to
758 temperatures more consistent with greenschist or higher metamorphism (Bustin et al., 1995; Qu et
759 al., 2020). Black chert of the Angmaat Formation shows no direct evidence for hydrothermal
760 circulation or metamorphic overprint. Most organic microfossils and a large portion of UOM are
761 imbedded in chert that is characterized as penecontemporaneous with deposition or of early
762 diagenetic origin. Still, some UOM and organic microfossils occur in direct contact with or are found
763 imbedded within later diagenetic phases such as chert spherules (Figures 3f and 4e, f, 11i, j),
764 chalcedony void fillings (Figure 5) and dolomite fracture fills (Figures 7a-c). This is particularly true for
765 sample WWB-17-5, which is the sample with the largest variation of the Raman signal (Table 3). In this
766 sample, however, the overall maturity of coccoidal microfossils imbedded in early diagenetic chert
767 and of spherical organic structures embedded in burial diagenetic dolomite as well as the detected
768 variation between individual neighboring organic microfossils and structures in each of these minerals
769 is similar (Figures 9, 10 and 12), which argues against a significant influence by the formation of
770 secondary minerals. The same is true for filamentous microfossils in sample WWB-17-5 that are either

771 imbedded in early diagenetic chert (Figure 3e) or in later stage chalcedony (Figure 5c), which show no
772 difference in their Raman signal. In turn, in both samples with significant sample-scale variation (NL-
773 17-M and WWB-17-5), organic microfossils and UOM imbedded in the mineral matrix show mostly a
774 higher maturity than free UOM in pore space, thereby indicating that early diagenetic mineralization
775 may have influenced the maturity pathway of OM. This is most apparent but rarely observed on a
776 small scale in sample NL-17-M where free UOM shows lower maturity than that of inclusions of UOM
777 in neighboring later diagenetic chert spherules (Figure 11i, j). This observation implies that the actual
778 preservation of OM in a mineral matrix may affect the maturation pathway similarly as to what has
779 been demonstrated experimentally (Li et al., 2014). We expect that such a process, however, only
780 accounts for a minor portion of the observed differences in maturity because of the rarity and the
781 small size of the observed inclusions of OM in the spherules.

782 **7.2. Organic precursors**

783 Variations of the Raman signal of OM caused by different organic precursor materials are generally
784 only detectable in low mature (lower carbonization) OM (Vendenbroucke and Largeau 2007; Igisu et
785 al., 2009; Qu et al., 2015 and 2018; Bonneville et al., 2020; Pang et al., 2020). Interpretations are
786 primarily limited to the very basic subdivision of OM derived from the three domains of life, and need
787 to be backed up by other analytical methods (Igisu et al., 2009; Qu et al., 2015 and 2018; Bonneville
788 et al., 2020). The taxonomy of organic microfossils in the Angmaat Formation appears to be diverse,
789 with multiple filamentous and coccoidal form taxa (Figures 3, 8, 11, 12 and 13). These are described
790 in detail in Knoll et al. (2013) and are interpreted as cyanobacteria, although a variety of small often
791 poorly preserved coccoidal microfossils could also include heterotrophic bacteria (Knoll et al., 2013).
792 The only non-bacterial microfossil known from the Angmaat Formation but not observed in this study
793 is the early red alga *Bangiomorpha pubescens* (Butterfield, 2000; Knoll et al., 2013). The strong
794 dominance of organic microfossils with a cyanobacterial origin suggests that variations of the Raman-
795 signal based on differences of organic precursor material as observed before (Igisu et al., 2009; Qu et

796 al., 2015 and 2018; Bonneville et al., 2020) should be minor and cannot be resolved with the data
797 presented here.

798 Differences in the Raman-signal occur independent of taxonomic classification. The two coccoidal
799 microfossils chosen for STXM-analysis are from the same taxonomic group, yet display a strong
800 difference in both Raman character and their chemical composition. Differences between taxonomic
801 groups are not found, in this study, to be large. Generally, filamentous microfossils record lower
802 variation in maturity than that observed in coccoidal microfossils (Table 3; Figure 9). However, such
803 taxonomic patterns of maturity do not occur across all samples, indicating that observations should
804 not be taken as a robust trend.

805 **7.3. Early diagenesis and migration of OM**

806 Localized early diagenetic mineralization potentially triggered by metabolic reactions has been
807 proposed to cause differences in OM-chemistry observed in weakly metamorphosed rocks (Lepot et
808 al., 2009). The circulation of hydrothermal fluids and potential migration of soluble organic
809 compounds in greenschist metamorphic rocks has also been proposed as possible cause for
810 inconsistencies in the maturity of OM (Qu et al., 2020). The potential for migration of soluble
811 compounds of low mature OM is likely enhanced by the porosity of sedimentary rocks and the higher
812 content of soluble organic compounds in highly disordered OM compared to more mature OM in
813 metasedimentary rocks. Generally, low porous cherts have been suggested to limit such migration; as
814 a result, chert has been used preferentially to derive our understanding of maturation pathways for
815 OM (Delarue et al., 2016).

816 Apparent correlation between the homogeneity of the Raman signal on a sample scale and the overall
817 diagenetic history recorded in the sample suggest that chert is not immune to effects of diagenetic
818 fluid flow and potential migration of organic compounds. The Raman character of OM in laminated
819 chert, that records relatively low porosity (WWB-17-10 and NL-17-N), is largely homogeneous, while
820 the Raman character of OM in nodular chert, which shows wide fractures and pore spaces occupied

821 by free UOM, is highly variable (WWB-17-5 and NL-17-M; Figure 9; Table 1, 3). This indicates that the
822 overall porosity of the host rock is indeed a critical factor for the maturity of OM within these samples.
823 Low porosity samples, however, despite showing overall homogeneous Raman signatures of OM, still
824 record differences in maturity between each other (ΔT of ca. 40°C), indicating that porosity, although
825 most likely the cause of intra-sample variation, may not be the only factor in determination of Raman
826 signals.

827 In highly porous samples, free UOM entrapped within pore spaces is the least mature type of OM
828 (Table 3) and other types of OM, such as organic microfossils or UOM imbedded in a mineral matrix,
829 that are in close proximity to large masses of free UOM show mostly a lower maturity than their more
830 distant counterparts. This suggests that OM of low maturity could have migrated into the pore spaces
831 of nodular chert from rocks that experienced a lower diagenetic overprint. This cannot explain,
832 however, the low maturity of organic microfossils that clearly occur in their original positions (e.g.
833 Figure 13b). In an alternate scenario, exposure of UOM to fluids percolating through the pore spaces
834 could have prevented dehydration of OM which substantially contributes to the carbonization
835 pathway (Vendenbroucke and Largeau 2007; Buseck and Beyssac, 2014). Organic microfossils
836 preserved within chert nodules or spherical organic structures (SOS) preserved in secondary dolomite
837 crystals could be similarly influenced by fluid circulation through micro- and nano- pores. The lower
838 AI and higher UI of the STXM-analyzed low-mature coccoidal microfossil (Figures 14 and
839 Supplementary Figure 10) could be a result of the presence of pore fluids circulating through a
840 neighboring micro-fracture (Figure 12b). Regardless of this mechanism, presumably symsedimentary
841 silicification allowed for excellent chemical preservation of OM and the low permeability of the
842 preserved chert units and pristine preservation of microbial mat structures suggest that OM is still
843 locally derived.

844

845 **8. Conclusion**

846 Organic microfossils and unrecognizable organic material from black cherts of the Angmaat Formation
847 show large variation in Raman spectra resulting in large variation in estimated maturity and calculated
848 H:C ratios between different samples and between organic microfossils and UOM of the same sample.
849 STXM-mapping of two coccoidal microfossils of the same taxonomy and similar taphonomy but with
850 significantly different Raman spectra shows large differences in the chemical composition of the
851 preserved OM that can be attributed to varying ratios of aromatic compounds relative to ketones and
852 phenols. Physical structural ordering and differences in organic precursor material have only minor
853 influence on the observed differences in Raman spectroscopy and STXM. The most likely explanation
854 for the observed variation is chemical ordering or the lack thereof caused by the suppression of
855 carbonization-induced dehydration due to the presence of diagenetic pore fluids. This is strongly
856 influenced by the porosity of the analyzed chert where higher porosity correlates directly to a higher
857 variability of the maturity and underlying chemical composition of OM. The large differences in the
858 involvement of aromatic groups and carbon bound heteroatoms and OH groups shown by STXM-
859 mapping indicate that the diversion of Raman-parameters from the known carbonization pathway of
860 OM is most likely representative of an alternative maturation pathway triggered by these chemical
861 variations. This alternative pathway is most evident by the strongly changing intensity ratio R3 and an
862 equally strong change of the width of the spectral maximum at ca. 1600 cm^{-1} . Our study shows that
863 diverse populations of microfossils in ancient sedimentary rocks show significant small-scale variation
864 in their chemical maturity that are potentially caused by multiple processes. Raman spectroscopy, is
865 a valuable, fast and non-destructive method to identify the least altered specimens in diverse
866 populations of ancient organic microfossils that however, needs to be applied in-situ on
867 petrographically well characterized samples to fully understand the meaning of individual
868 measurements. This is especially important for organic microfossils that show such exceptional
869 preservation as in the chert of the Angmaat Formation where the low chemical and structural
870 alteration potentially allowed for the preservation of the observed variation.

871

872 **References**

- 873 Alleon, J., Bernard, S., Le Guillou, C., Daval, D., Skouri-Panet, F., Kuga, M., Robert, F., 2017. Organic molecular
874 heterogeneities can withstand diagenesis. *Sci. Rep.* 7, 1508. [https://doi.org/10.1038/s41598-017-](https://doi.org/10.1038/s41598-017-01612-8)
875 01612-8
- 876 Aoya, M., Kouketsu, Y., Endo, S., Shimizu, H., Mizukami, T., Nakamura, D., Wallis, S., 2010. Extending the
877 application of Raman carbonaceous-material geothermometer using data from contact metamorphic
878 rocks. *J. metamorphic Geol.*, 28, 895-914. <https://doi.org/10.1111/j.1525-1314.2010.00896.x>
- 879 Arne, D.C., Duddy, I.R., Sangster, D.F., 1990. Thermochronological constraints on ore formation at the Gays
880 River Pb-Zn deposit, Nova Scotia, Canada, from apatite fission track analysis. *Canadian Journal of*
881 *Earth Sciences*, 27, 1013-1022.
- 882 Baludikay, B.K., Francois, C., Sforza, M.C., Beghin, J., Cornet, Y., Storme, J.-Y., Fagel, N., Fontaine, F., Littke, R.,
883 Baudet, D., Delvaux, D., Javaux, E.J., 2018. Raman microspectroscopy, bitumen reflectance and illite
884 crystallinity scale: comparison of different geothermometry methods on fossiliferous Proterozoic
885 sedimentary basins (DR Congo, Mauritania and Australia). *International Journal of Coal Geology*, 191,
886 80-94. <https://doi.org/10.1016/j.coal.2018.03.007>
- 887 Bartley, J.K., 1996. Actualistic Taphonomy of Cyanobacteria: Implications for the Precambrian Fossil Record.
888 *PALAIOS*, 11, 571–586.
- 889 Bernard, S., Benzerara, K., Beyssac, O., Menguy, N., Guyot, F., Brown Jr., G.E., Goffe, B., 2007. Preservation of
890 plant fossils in high-pressure metamorphic rocks. *Earth and Planetary Science Letters* 262 (1–2), 257–
891 272.
- 892 Bernard S., Benzerara K., Beyssac O., Brown, Jr., G. E., Grauvogel-Stamm L. and Düringer P. 2009.
893 Ultrastructural and chemical study of modern and fossil sporoderms by Scanning Transmission X-ray
894 Microscopy (STXM). *Review of Palaeobotany and Palynology* 156, 248–261.
- 895 Bernard, S., Horsfield, B., Schulz, H-M., Wirth, R., Schreiber, A., Sherwood, N., 2012. Geochemical evolution of
896 organic-rich shales with increasing maturity: A STXM and TEM study of the Posidonia Shale (Lower
897 Toarcian, northern Germany). *Marine and Petroleum Geology*, 31, 70-89.
- 898 Beyssac, O., Goffe, B., Chopin, C., Rouzaud, J.N., 2002. Raman spectra of carbonaceous material from
899 metasediments: a new geothermometer. *J. metamorphic Geol.*, 20, 859–871.
900 <https://doi.org/10.1046/j.1525-1314.2002.00408.x>
- 901 Beyssac, O., Simoes, M., Avouac, J-P., Farley, K., Chen, Y-G., Chan, Y-C., Goffe, B., 2007. Late Cenozoic
902 metamorphic evolution and exhumation of Taiwan. *Tectonics*, 26, TC6001.
903 <https://doi.org/10.1029/2006TC002064>
- 904 Bonneville, S., Delpomdor, F., Preat, A., Chevallier, C., Araki, T., Kazemlan, M., Steel, A., Schreiber, A., Wirth, R.,
905 Benning, L.G., 2020. Molecular identification of fungi microfossils in Neoproterozoic shale rock.
906 *Science Advances*, 6, eaax7599. <https://doi.org/10.1126/sciadv.aax7599>
- 907 Bosak, T., Bush, J., Flynn, M., Liang, B., Ono, S., Petroff, A.P., Sim, M.S., 2010. Formation and stability of
908 oxygen-rich bubbles that shape photosynthetic mats: *Geobiology*, 8, 45–55.
909 <http://doi.org/10.1111/j.1472-4669.2009.00227.x>.
- 910 Buseck, P.R., and Beyssac, O., 2014. From organic matter to graphite: Graphitization. *Elements* 10, 421-426.
911 <https://doi.org/10.2113/gselements.10.6.421>
- 912 Bustin, R.M., Ross, J.V. and Rouzaud, J.N., 1995. Mechanism of graphite formation from kerogen: experimental
913 evidence. *International Journal of Coal Geology*, 28, 1-36. [https://doi.org/10.1016/0166-](https://doi.org/10.1016/0166-5162(95)00002-U)
914 5162(95)00002-U
- 915 Butterfield, N.J., 2000. *Bangiomorpha pubescens* n. gen., n. sp.: Implications for the evolution of sex,
916 multicellularity and the Mesoproterozoic/Neoproterozoic radiation of eukaryotes: *Paleobiology*, 26,
917 386-40. [https://dx.doi.org/10.1666/0094-8373\(2000\)026%3C0386:BPNGNS%3E2.0.CO;2](https://dx.doi.org/10.1666/0094-8373(2000)026%3C0386:BPNGNS%3E2.0.CO;2)

- 918 Butterfield, N.J., 2015. Early evolution of the Eukaryota. *Palaeontology*, 58, 5–17.
919 <https://doi.org/10.1111/pala.12139>
- 920 Czaja, A.D., Beukes, N.J., and Osterhout, J.T., 2016. Sulfur-oxidizing bacteria prior to the Great Oxidation Event
921 from the 2.52 Ga Gamohaan Formation of South Africa. *Geology*, 44, 983–986. doi:10.1130/G38150.1
- 922 Delarue, F., Rouzaud, J-N., Derenne, S., Bourbin, M., Westall, F., Kremer, B., Sugitani, K., Deldicque, D., Robert,
923 F., 2016. The Raman-Derived Carbonization Continuum: A Tool to Select the Best-Preserved Molecular
924 Structures in Archean Kerogens. *Astrobiology*, 16, 407-417.
925 <https://dx.doi.org/10.1089%2Fast.2015.1392>
- 926 Dunham, J.J. and Kah, L.C., 2018. Crystallization of opal to length-fast chalcedony within Proterozoic
927 microfossiliferous chert. GSA Annual Meeting, Indianapolis, Indiana, USA.
928 <https://doi.org/10.1130/abs/2018AM-322571>
- 929 Edwards C.T., Pufahl P.K., Hiatt E.E., Kyser T.K. 2012. Paleoenvironmental and taphonomic controls on the
930 occurrence of Paleoproterozoic microbial communities in the 1.88Ga Ferriman Group, Labrador
931 Trough, Canada. *Precambrian Research*, 212/213, 91-106.
932 <https://doi.org/10.1016/j.precamres.2012.04.020>
- 933 Ferralis, N., Matys, E.D., Knoll, A.H., Hallmann, C., Summons, R.E., 2016. Rapid, direct and non-destructive
934 assessment of fossil organic matter via microRaman spectroscopy. *Carbon*, 108, 440-449.
935 <https://doi.org/10.1016/j.carbon.2016.07.039>
- 936 Ferrari, A.C. and Robertson, J., 2000. Interpretation of Raman spectra of disordered and amorphous carbon.
937 *Physical Review B*, 6, 14095–14107. <https://doi.org/10.1103/PhysRevB.61.14095>
- 938 Forrest, G., Vilcins, G, Lephardt, J.O., 1976. Structural characterization of cyclopropyl pyridyl ketones by i.r. and
939 Raman spectroscopy. *Spectrochimica Acta*, 32A, 511-518.
- 940 Gibson, T.M., Shih, P.M., Cumming, V.M., Fischer, W.W., Crockford, P.W., Hodgskiss, M.S.W., Wörndle, S.,
941 Creaser, R.A., Rainbird, R.H., Skulski, T.M., Halverson, G.P., 2018. Precise age of *Bangiomorpha*
942 *pubescens* dates the origin of eukaryotic photosynthesis. *Geology*, 46, 135–138.
943 <https://doi.org/10.1130/G39829.1>
- 944 Golovenko, V.K., & Belova, N.YU, 1984. Riphean microbios in cherts of the Billyakh Group on the Anabar
945 Uplift: *Paleontological Journal*, 4, 20–30.
- 946 Guedes, A., Valentim, B., Prieto, A.C., Rodrigues, S., Noronha, F., 2010. Micro-Raman spectroscopy of
947 collotelinite, fusinite and macrinite. *International Journal of Coal Geology*, 83, 415 – 422.
948 <https://doi.org/10.1016/j.coal.2010.06.002>
- 949 Guo, Z., Peng, X., Czaja, A.D., Chen, S., Ta, K., 2018. Cellular taphonomy of well-preserved Gaoyuzhuang
950 microfossils: A window into the preservation of ancient cyanobacteria. *Precambrian Research*, 304,
951 88-98. <https://doi.org/10.1016/j.precamres.2017.11.007>
- 952 Hahn, K.E., Turner, E.C., Babechuk, M.G., Kamber, B.S., 2015. Deep-water seep-related carbonate mounds in a
953 Mesoproterozoic alkaline lake, Borden Basin (Nunavut, Canada). *Precambrian Res.*, 271, 173–197.
- 954 Henry, D.G., Jarvis, I., Gillmore, G., Stephenson, M., 2019. Raman spectroscopy as a tool to determine the
955 thermal maturity of organic matter: Application to sedimentary, metamorphic and structural geology.
956 *Earth-Science Reviews*, 198, 102936. <https://doi.org/10.1016/j.earscirev.2019.102936>
- 957 Hnatyshin, D., Kontak, D.J., Turner, E.C., Creaser, R.A., Morden, R., Stern, R.A., 2016. Geochronologic (Re-Os)
958 and fluid-chemical constraints on the formation of the Mesoproterozoic-hosted Nanisivik Zn-Pb
959 deposit, Nunavut, Canada: evidence for early diagenetic, low-temperature conditions of formation;
960 *Ore Geology Reviews*, 79, 189–217. <https://doi.org/10.1016/j.oregeorev.2016.05.017>
- 961 Hofmann, H.J., 1976. Precambrian microflora, Belcher Island, Canada: Significance and systematic: *Journal of*
962 *Paleontology*, 50, 1040–1073.

- 963 Hofmann, H.J., Jackson, G.D., 1991. Shelf-Facies Microfossils from the Uluksan Group (Proterozoic Bylot
964 Supergroup), Baffin Island, Canada. *J. Paleontol.*, 65, 361–382.
- 965 Horodyski, R.J., and Donaldson, J.A., 1980. Microfossils from the middle Proterozoic Dismal Lakes Group, arctic
966 Canada: *Precambrian Research*, 11, 125–159. [https://doi.org/10.1016/0301-9268\(80\)90043-1](https://doi.org/10.1016/0301-9268(80)90043-1)
- 967 Igisu, M., Ueno, Y., Shimojima, M., Nakashima, S., Awramik, S.M., Ohta, H., Maruyama, S., 2009. Micro-FTIR
968 spectroscopic signatures of Bacterial lipids in Proterozoic microfossils. *Precambrian Research*, 173, 19-
969 26. <https://doi.org/10.1016/j.precamres.2009.03.006>
- 970 Jackson, G., Iannelli, T., 1981. Rift-related cyclic sedimentation in the Neohelikian Borden Basin, northern
971 Baffin Island. *Geol. Surv. Can. Pap.*, 81, 269–302.
- 972 Javaux, E.J., Knoll, A.H., Walter, M.R., 2001. Morphological and ecological complexity in early eukaryotic
973 ecosystems. *Nature* 412, 66–69. <https://doi.org/10.1038/35083562>
- 974 Javaux, E.J., Lepot, K., 2018. The Paleoproterozoic fossil record: Implications for the evolution of the biosphere
975 during Earth's middle-age. *Earth-Science Reviews*, 176, 68-86.
976 <https://doi.org/10.1016/j.earscirev.2017.10.001>
- 977 Kah, L.C., 2000. Depositional $\delta^{18}\text{O}$ signatures in Proterozoic dolostones: Constraints on seawater chemistry
978 and early diagenesis. *SEPM (Society for Sedimentary Geology), Special Publication* 67.
- 979 Kah, L.C., Knoll, A.H., 1996. Microbenthic distribution of Proterozoic tidal flats: Environmental and taphonomic
980 considerations. *Geology*, 24, 79–82.
- 981 Kah, L.C., Lyons, T.M., Chelsey, J.T., 2001. Geochemistry of a 1.2 Ga carbonate-evaporite succession, northern
982 Baffin and Bylot Islands: Implication for Mesoproterozoic marine evolution: *Precambrian Research*,
983 111, 203–234. [https://doi.org/10.1016/S0301-9268\(01\)00161-9](https://doi.org/10.1016/S0301-9268(01)00161-9)
- 984 Kah, L.C., Sherman, A.G., Narbonne, G.M., Knoll, A.H., Kaufman, A.J., 1999. $\delta^{13}\text{C}$ stratigraphy of the
985 Proterozoic Bylot Supergroup, Baffin Island, Canada: Implications for regional lithostratigraphic
986 correlations. *Can. J. Earth Sci.*, 36, 313–332.
- 987 Knoll, A. H., 2014. Paleobiological perspectives on early eukaryotic evolution. *Cold Spring Harbor Perspectives*
988 *in Biology*, 6 (1), <https://doi.org/10.1101/cshperspect.a016121>
- 989 Knoll, A.H., and Golubic, S., 1979. Anatomy and taphonomy of a Precambrian algal stromatolite: *Precambrian*
990 *Research*, 10, 115–151. [https://doi.org/10.1016/0301-9268\(79\)90022-6](https://doi.org/10.1016/0301-9268(79)90022-6)
- 991 Knoll, A.H., Wörndle, S., Kah, L.C., 2013. Covariance of microfossil assemblages and microbialite textures across
992 an upper Mesoproterozoic carbonate platform. *Palaios*, 28, 453–470.
993 <https://doi.org/10.2110/palo.2013.p13-005r>
- 994 Kouketsu, Y., Mizukami, T., Mori, H., Endo, S., Aoya, M., Hara, H., Nakamura, D., and Wallis, S., 2014. A new
995 approach to develop the Raman carbonaceous material geothermometer for low-grade
996 metamorphism using peak width. *Island Arc*, 23, 33-50. <https://doi.org/10.1111/iar.12057>
- 997 Lahfid, A., Beyssac, O., Deville, E., Negro, F., Chopin, C. and Goffe, B., 2010. Evolution of Raman spectrum of
998 carbonaceous material in low-grade metasediments of the Glarus Alps (Switzerland). *Terra Nova*, 22,
999 354–360. <https://doi.org/10.1111/j.1365-3121.2010.00956.x>
- 1000 Lepot K., Benzerara K., Rividi N., Cotte M., Brown, Jr., G. E. and Philippot P. 2009. Organic matter
1001 heterogeneities in 2.72 Ga stromatolites: alteration versus preservation by sulfur incorporation.
1002 *Geochimica et Cosmochimica Acta*, 73(21), 6579–6599. <https://doi.org/10.1016/j.gca.2009.08.014>
- 1003 Lerotic, M., Mak, R., Wirick, S., Meirer, F., Jacobsen, C., 2014. MANTIS: a program for the analysis of X-ray
1004 spectromicroscopy data. *Journal of Synchrotron Radiation*, 21, 1206–1212.
1005 <https://doi.org/10.1107/S1600577514013964>
- 1006 Li, J., Bernard, S., Benzerara, K., Beyssac, O., Allard, T., Cosmidis, J., Moussou, J., 2014. Impact of
1007 biomineralization on the preservation of microorganisms during fossilization: An experimental
1008 perspective, *Earth and Planetary Science Letters*, 400, 113-122.

- 1009 Lünsdorf, N.K., Dunkl, I., Schmidt, B.C., Rantitsch, G., von Eynatten, H., 2014a. Towards a Higher Comparability
1010 of Geothermometric Data obtained by Raman Spectroscopy of Carbonaceous Material. Part I:
1011 Evaluation of Biasing Factors. *Geostandards and Geoanalytical Research*, 38, 73-94.
1012 <https://doi.org/10.1111/j.1751-908X.2013.12011.x>
- 1013 Lünsdorf, N.K., Dunkel, I., Schmidt, B.C., Rantitsch, G., von Eynatten H., 2014b. Towards a Higher Comparability
1014 of Geothermometric Data obtained by Raman Spectroscopy of Carbonaceous Material. Part 2: A
1015 Revised Geothermometer. 41, 593-612. <https://doi.org/10.1111/ggr.12178>
- 1016 Manning-Berg, A.R., and Kah, L.C., 2017. Proterozoic microbial mats and their constraints on environments of
1017 silicification. *Geobiology*, 15, 469-483. <https://doi.org/10.1111/gbi.12238>
- 1018 Manning-Berg, A.R., Wood, R.S., Williford, K.H., Czaja, A.D., Kah, L.C., 2019. The Taphonomy of Proterozoic
1019 Microbial Mats and Implications for Early Diagenetic Silicification. *Geosciences*, 9, 40.
1020 <https://doi.org/10.3390/geosciences9010040>
- 1021 Mapelli, C., Castiglioni, C., Zerbi, G., and Müllen, K. 1999. Common force field for graphite and polycyclic
1022 aromatic hydrocarbons. *Phys. Rev. B* 60, 12710–12725.
- 1023 Mayo, D.W., Miller, F.A., Hannah, R.W., 2003. Course Notes on the Interpretation of Infrared and Raman
1024 Spectra: John Wiley & Sons, Inc, pp. 567. <https://doi.org/10.1002/0471690082>
- 1025 McNaughton, K., Smith, T.E., 1986. A fluid inclusion study of sphalerite and dolomite from the Nanisivik lead-
1026 zinc deposit, Baffin Island, Northwest Territories, Canada. *Economic Geology*, 81, 713–20.
- 1027 Nyberg, A.V., Schopf, J.W., 1984. Microfossils in stromatolitic cherts from the upper Proterozoic Min'Yar
1028 Formation, southern Ural Mountains, USSR: *Journal of Paleontology*, 58, 738–772.
- 1029 Pang, K., Tang, Q., Wu, C., Li, G., Chen, L., Wan, B., Yuan, X., Bodnar, R.J., Xiao, S., 2020. Raman spectroscopy
1030 and structural heterogeneity of carbonaceous material in Proterozoic organic-walled microfossils in
1031 the North China Craton. *Precambrian Research*, 346, 105818.
1032 <https://doi.org/10.1016/j.precamres.2020.105818>
- 1033 Pompeu, D.R., Larondelle, Y., Rogez, H., Abbas, O., Fernandez Pierna, J.A., Baeten, V., 2018. Characterization
1034 and discrimination of phenolic compounds using Fourier transform Raman spectroscopy and
1035 chemometric tools. *Biotechnol. Agron. Soc. Environ.*, 22, 13-28. <https://doi.org/10.25518/1780-4507.16270>
- 1037 Qu, Y., Engdahl, A., Zhu, S., Vajda, V., McLoughlin, N., 2015. Ultrastructural Heterogeneity of Carbonaceous
1038 Material in Ancient Cherts: Investigating Biosignatures Origin and Preservation.
1039 <https://doi.org/10.1089/ast.2015.1298>
- 1040 Qu, Y., van Zuilen, M.A., Lepland, A., 2020. Hydrothermal circulation and oil migration at the root of the
1041 heterogeneous micro-structure of carbonaceous material in the 2.0 Ga Zaonega Formation, Onega
1042 Basin, Russia. *Precambrian Research*, 343, 105705. <https://doi.org/10.1016/j.precamres.2020.105705>
- 1043 Qu, Y., Zhu, S., Whitehouse, M., Engdahl, A., McLoughlin, N., 2018. Carbonaceous biosignatures of the earliest
1044 putative macroscopic multicellular eukaryotes from 1630 Ma Tuanshanzi Formation, north China.
1045 *Precambrian Research*, 304, 99-109. <https://doi.org/10.1016/j.precamres.2017.11.004>
- 1046 Rahl, J.M., Anderson, K.M., Brandon, M.T., Fassoulas, C., 2005. Raman spectroscopic carbonaceous material
1047 thermometry of low-grade metamorphic rocks: Calibration and application to tectonic exhumation in
1048 Crete, Greece. *Earth and Planetary Science Letters*, 240, 339-354.
1049 <https://doi.org/10.1016/j.epsl.2005.09.055>
- 1050 Romero-Sarmiento, M.F., Rouzaud, J.-N., Bernard, S., Deldicque, D., Thomas, M., Littke, R., 2014. Evolution of
1051 Barnett Shale organic carbon structure and nanostructure with increasing maturation. *Org. Geochem.*
1052 71, 7–16. <https://doi.org/10.1016/j.orggeochem.2014.03.008>
- 1053 Rouzaud, J.-N., Delicque, D., Charon, É., Pageot, J., 2015. Carbons at the heart of questions on energy and
1054 environment: A nanostructural approach. *C. R. Geoscience*, 347, 124-133.
1055 <http://doi.org/10.1016/j.crte.2015.04.004>

1056 Sadezky, A., Muckenhuber, H., Grothe, H., Niessner, R., Pöschl, U., 2005. Raman microspectroscopy of soot and
1057 related carbonaceous materials: spectral analysis and structural information. *Carbon*, 43, 1731–1742.

1058 Schopf, J.W., 1968. Microflora of the Bitter Springs Formation, late Precambrian central Australia: *Journal of*
1059 *Paleontology*, 42, 651–688.

1060 Schopf, J.W., Kudryavtsev, A.B., Agresti, D.G., Czaja, A.D., and Wdowiak, T.J., 2005. Raman imagery: a new
1061 approach to assess the geochemical maturity and biogenicity of permineralized Precambrian fossils.
1062 *Astrobiology*, 5, 333–371. doi:10.1089/ast.2005.5.333

1063 Sforza, M.C., van Zuilen, M.A., and Philippot, P. 2014. Structural characterization by Raman hyperspectral
1064 mapping of organic carbon in the 3.46 billion-year-old Apex chert, Western Australia. *Geochim*
1065 *Cosmochim Acta*, 124, 18–33. <https://doi.org/10.1016/j.gca.2013.09.031>

1066 Turner, E.C., 2009. Mesoproterozoic carbonate systems in the Borden Basin, Nunavut. *Can. J. Earth Sci.*, 46,
1067 915–938.

1068 Vandenbroucke, M., Largeau, C., 2007. Kerogen origin, evolution and structure. *Organic Geochemistry*, 38,
1069 719–833. <https://doi.org/10.1016/j.orggeochem.2007.01.001>

1070 van Zuilen, M.A., Fliegel, D., Wirth, R., Leland, A., Qu, Y., Schreiber, A., Romashkin, A.E., Philippot, P., 2012.
1071 Mineral-templated growth of natural graphite films. *Geochim. Cosmochim. Acta*, 83, 252–262.
1072 <https://doi.org/10.1016/j.gca.2011.12.030>

1073 Wirth, R., 2009. Focused Ion Beam (FIB) combined with SEM and TEM: Advanced analytical tools for studies of
1074 chemical composition, microstructure and crystal structure in geomaterials on a nanometer scale.
1075 *Chem. Geol.* 261, 217–229. <https://doi.org/10.1016/j.chemgeo.2008.05.019>

1076 Wopenka, B. and Pasteris, J.D., 1993. Structural characterization of kerogens to granulite-facies graphite:
1077 applicability of Raman microprobe spectroscopy. *Am Mineral*, 78, 533–557.

1078 Zhang, Y., 1981. Proterozoic stromatolitic microfloras of the Gaoyuzhuang Formation (early Sinian, Riphean),
1079 Hebei, China: *Journal of Paleontology*, 55, 485–506.

1080

1081 **Figure 1:** General geology of the Bylot Supergroup on northern Baffin Island, Canada (modified after
1082 Manning-Berg et al., 2019). **(a):** Western Baffin Island and Bylot Island (upper right). The field area in
1083 the red rectangle is shown in b. **(b):** General geology of the east/central Borden basin on Baffin Island
1084 with the Angmaat Formation as part of the Uluksan Group (Legend to the lower left). Sampling
1085 locations are marked with red dots. WWB: west White Bay; NL: north lake.

1086

1087 **Figure 2:** Peak-fitting solutions for Raman spectra of organic microfossils of the Angmaat Formation.
1088 **(a):** 4-peak deconvolution (fitting G) of Raman spectra obtained with 532 nm laser after Kouketsu et
1089 al., (2016). **(b):** 5-peak deconvolution of Raman spectra obtained with 532 nm laser after Delarue et
1090 al., (2016). **(c):** 7-peak deconvolution of Raman spectra obtained with 532 nm laser. **(d):** 6-peak
1091 deconvolution of Raman spectra obtained with 633 nm laser after Ferralis et al., (2016). Note: the
1092 spectrum in d was obtained from the same spot as in a – c. Note: details of fitting solutions and residual
1093 spectra are shown in Supplementary Figure 2.

1094

1095 **Figure 3:** Organic microfossils and unrecognizable organic material (UOM) in Angmaat Formation
1096 chert. **(a):** Thick filamentous microfossils in laminated chert of sample WWB-17-10. **(b):** Coccoidal
1097 microfossils in laminated chert of sample NL-17-M. The image is overexposed to light to visualize the
1098 internal structures of individual microfossils. **(c):** Thin, fragmented filamentous microfossil in

1099 laminated chert from sample NL-17-N. **(d)**: Colonial coccoidal microfossils in chert from sample WWB-
1100 17-5. **(e)**: Thin, poorly preserved filamentous microfossils preserved in chert from sample WWB-17-5.
1101 **(f)**: UOM in pore space between chert nodules and spherules in sample WWB-17-5.

1102

1103 **Figure 4:** Mineral fabrics and pseudomorphs. **(a, b)**: Translucent- and polarized-light image of
1104 microcrystalline-dolomite (upper left) and -chert (lower right) in sample WWB-17-5. **(c)**: Polarized-
1105 light image of chert pseudomorphs after gypsum rosettes (sample WWB-17-10). **(d)**: Translucent-light
1106 image of partly silicified dolomite (black arrow) and chert pseudomorphs after dolomite (white
1107 arrows) in sample WWB-17-5. **(e)**: Nodule composed of chert spherules (sample WWB-17-5A). The
1108 zoning is caused by varying amounts of OM involved in the formation of the nodule. Black arrows point
1109 towards fairly well preserved coccoidal microfossils outside the nodule. The area in the dashed
1110 rectangle is shown in more detail in f. **(f)**: Polarized-light image of spherules showing typical radial
1111 alignment of chalcedony.

1112

1113 **Figure 5:** Fillings of former void spaces. **(a, b)**: Translucent- and polarized-light image ca. 5 mm large
1114 former void in the laminated area of sample NL-17-N. The filling shows zoning starting with a zone of
1115 fine crystalline dolomite at the edge followed by radially aligned chalcedony and mega-quartz in the
1116 center. **(c)**: Former voids in sample WWB-17-5 filled by botryoidal chalcedony. Note the filamentous
1117 microfossils at the edges that protrude into the former void (black arrows). **(d)**: Former void space
1118 filled by botryoidal chalcedony (sample NL-17-M) and a high amount of UOM that forms a dark film
1119 covering the radial growth of the chalcedony.

1120

1121 **Figure 6:** Diagenetic fabrics of dolomite. **(a, b)**: Translucent- and polarized-light image of up to 500 μm
1122 large vein filling idiomorphic dolomite crystals (sample WWB-17-5). The dolomite fills former pore
1123 space occupied by UOM and chert spherules that are now preserved as inclusions in dolomite. **(c)**:
1124 Vein filling euhedral dolomite incorporating spherical organic structures that are potential coccoidal
1125 microfossils or chert spherules coated by organic carbon (black arrows). **(d)**: Polarized-light image of
1126 a partly silicified dolomite nodule. Silicification is more advanced in the center of the nodule. **(e)**:
1127 Polarized-light image of a strongly silicified dolomite nodule with radially aligned chalcedony as outer
1128 zone followed by chert and micro-dolomite and mega-quartz in the center. Note the amalgamations
1129 of OM as dark thin layers between dolomite nodules. **(f)**: Stylolite in dolomite layer visible as
1130 meandering thin trace of OM.

1131

1132 **Figure 7:** Simplified diagenetic sequence of black chert of the Angmaat Formation with emphasis to
1133 sedimentary and diagenetic phases that interact with OM.

1134

1135 **Figure 8:** Raman spectral shapes recorded from coccoidal organic microfossils of sample 17-5. The
1136 shown coccoidal microfossils are embedded in chert and show cellular structures or are part of a
1137 colony of organic microfossils that contains numerous individuals with cellular structures.

1138

1139 **Figure 9:** Raman-parameters extracted from Raman-spectra of organic microfossils and UOM obtained
1140 with 533 nm laser. **(a)**: FWHM-1600 cm^{-1} vs. intensity ratio $R1(I-1600/I-1350)$. The gray arrow shows
1141 the inferred development of the two parameters with increasing maturity of OM after Kouketsu et al.,
1142 (2014). The black arrow shows the approximate development of the two parameters with increasing

1143 maturity of organic matter from the Angmaat Formation. **(b)**: Maximum thermal overprint (T in °C)
1144 calculated using the FWHM-D1 extracted from 4-peak fit after Kouketsu et al., (2014). **(c and d)**:
1145 Intensity ratio $R1_{(5p)}$ vs. FWHM-D1 and -D2 obtained from 5-peak fit after Delarue et al. (2016).
1146 Previously predicted carbonization and graphitization paths (¹Rouzaud et al., 2015; ²Delarue et al.,
1147 2016;) are given for comparison. **(e and f)**: Intensity ratio $R1_{(7p)}$ vs. FWHM-D1 and -D2 obtained from
1148 7-peak fit. Blue dashed lines show linear trends of each plot with arrows pointing towards increasing
1149 maturity. **(g)**: FWHM-D2 vs. $R3_{(7p)}$ obtained from 7-peak fit. **(h)**: Legend for a-g showing symbols sorted
1150 by sample, diagenetic and taxonomic context.

1151

1152 **Figure 10**: Raman parameters extracted from spectra recorded with 633 nm laser from sample WWB-
1153 17-5 **(a)**: Intensity ratio $D5/(G+D2)$ vs. H:C ratio. **(b)**: Intensity ratio $(D4+D5)/(G+D2)$ vs. H:C ratio. H:C
1154 ratios calculated using this intensity ratio are slightly lower than in a. **(c)**: Intensity ratio $D1/(G+D2)$ vs.
1155 FWHM-D1. Empty symbols are for comparison and show Raman parameters obtained from macerals
1156 of coals from the Penn State Coal Bank presented in Guedes et al. 2010. The cutoff at 100 cm^{-1} for the
1157 FWHM-D1 is a result of the restriction of the maximum peak width to this value. **(d)**: Legend for a – c.

1158

1159 **Figure 11**: Raman characteristics of organic microfossils and UOM. Spectral plots show multiple
1160 normalized spectra from the marked spots. Spectra may appear as one if they are similar. **(a, b)**: Line-
1161 map of filamentous microfossil from sample WWB-17-10. **(c, d)**: Line-map of coccoidal microfossil with
1162 preserved internal structures of sample NL-17-N. **(e, f)**: Line-map of coccoidal microfossil in secondary
1163 dolomite from sample WWB-17-5. **(g, h)**: Line-map of coccoidal microfossil in chert from sample
1164 WWB-17-5. **(i)**: Free UOM and UOM-sph in pore-space of sample NL-17-M. Spherules can contain
1165 inclusions of OM (light blue lens) or OM can be captured between amalgamated spherules (dark blue
1166 lens). **(j)**: Normalized Raman spectra of free UOM (yellow), of UOM-inclusion in spherule (light blue)
1167 and of UOM between spherules (dark blue).

1168

1169 **Figure 12**: Raman maps of organic microfossils from sample WWB-17-5 with higher mature OM
1170 marked in blue and lower mature OM marked in yellow. The respective spectra used to define blue
1171 and yellow areas and their parameters are shown to the right of each map. **(a)**: Raman map of a
1172 filamentous and coccoidal microfossil preserved in chert. **(b)**: Raman point map of coccoidal
1173 microfossils preserved in chert. **(c)**: Raman map of spherical organic structures preserved in dolomite.
1174 **(d)**: Raman map of coccoidal microfossils in contact to UOM preserved in chert.

1175

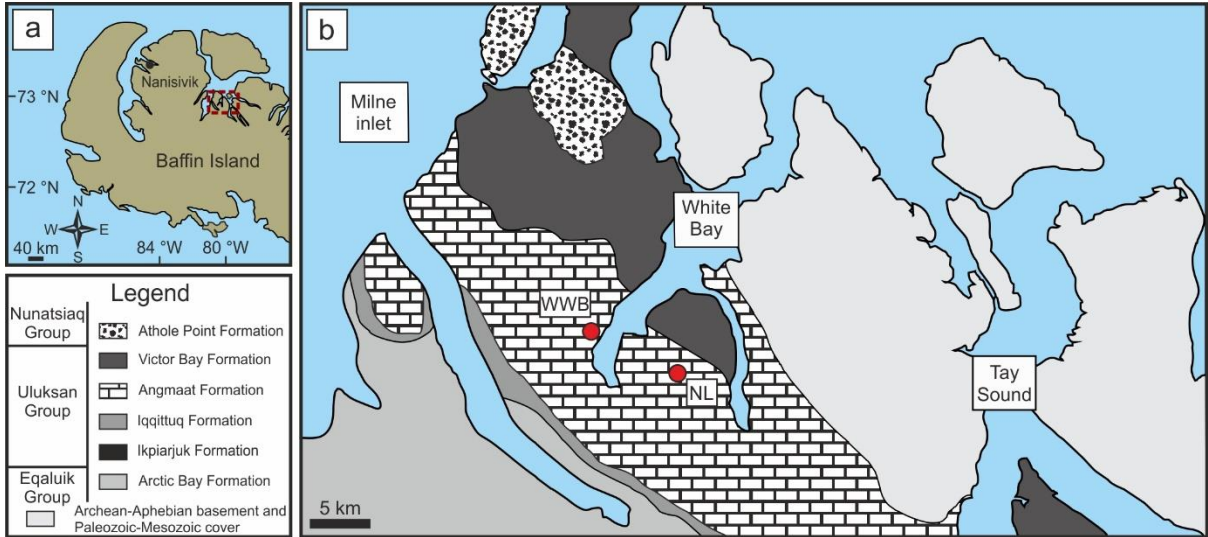
1176 **Figure 13**: Organic microfossils from sample WWB-17-5 analyzed by STXM-mapping. **(a)**: Polished slide
1177 of with position of coccoidal microfossils (in b and c) ca. 4 mm apart. **(b and c)**: Coccoidal microfossils
1178 chosen for STXM-mapping. The microfossil in b shows the Raman spectral shape S1 (microfossil A),
1179 the microfossil in c shows the Raman spectral shape S4 (microfossil B). Raman spots are shown as
1180 yellow and blue dots that correlate to the spectra in d and e. Lines are the positions of the FIB cuts.
1181 The dashed line in b marks the track of a thin fracture. **(d)**: Raman spectra of coccoidal microfossil A
1182 obtained with 532 nm and 633 nm laser and extracted Raman parameters indicative of lower maturity.
1183 **(e)**: Raman spectra of coccoidal microfossil B obtained with 532 nm and 633 nm laser and extracted
1184 Raman parameters indicative of higher maturity.

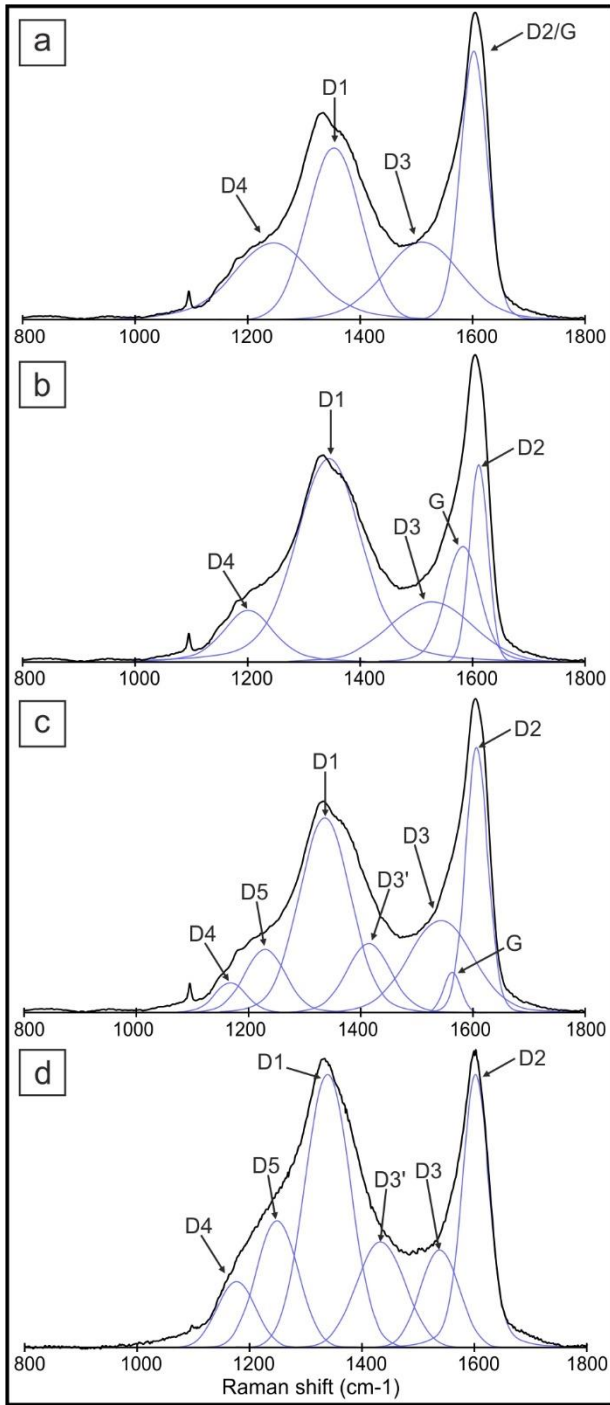
1185

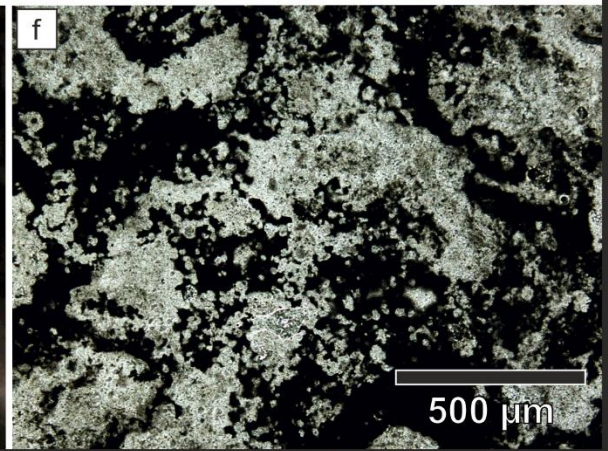
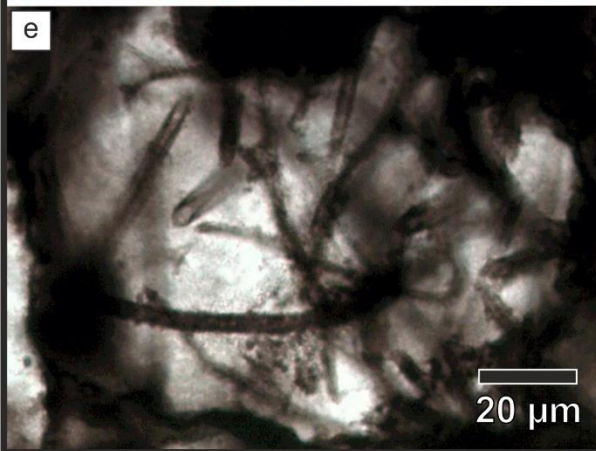
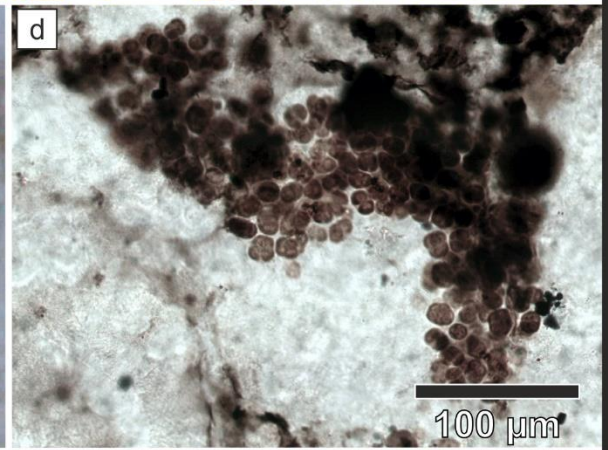
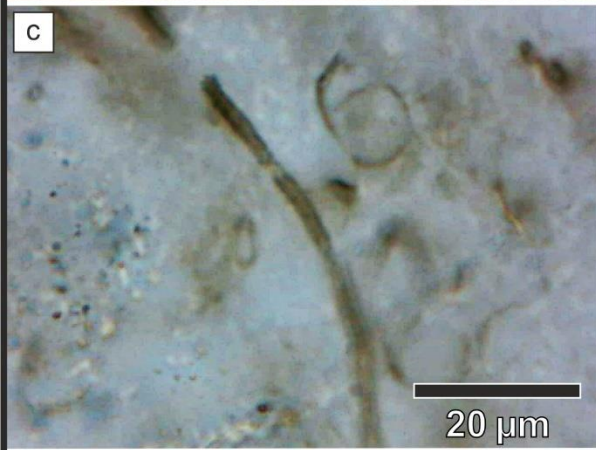
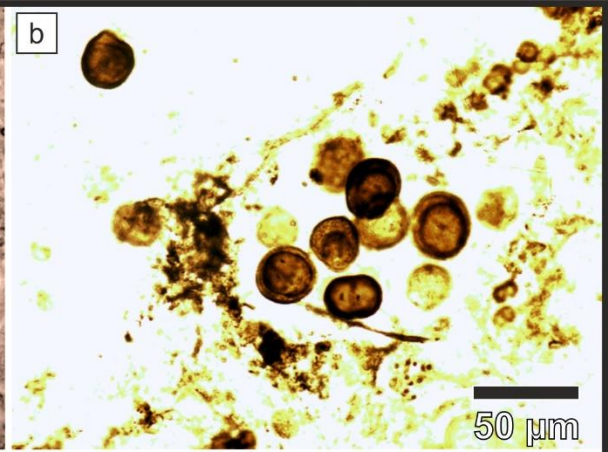
1186 **Figure 14:** STXM maps and corresponding NEXAFS-spectra. **(a):** Position of STXM map (6X6 μm) of
1187 organic microfossil-A with Raman spectral shape S1 (Figure 13b, d) on FIB foil and cluster map
1188 indicating three areas with different composition of organic matter. **(b):** Position of STXM map (5X5
1189 μm) of organic microfossil-B with Raman spectral shape S4 (Figure 13c, e) indicating three areas with
1190 different composition of organic matter. **(c):** NEXAFS spectrum of mapped area in (a) of microfossil-A
1191 with corresponding fitting. **(d):** NEXAFS spectrum of mapped area in (b) of microfossil-B with
1192 corresponding fitting. Fitting positions of Gaussian functions in (c) and (d) are shown in Supplementary
1193 Table 1. **(e):** NEXAFS spectra of cluster analysis of STXM map in (a). Colors correspond to the colormap
1194 in (a). **(f):** NEXAFS spectra of cluster analysis of STXM map in (b). Colors correspond to the colormap
1195 in (b).

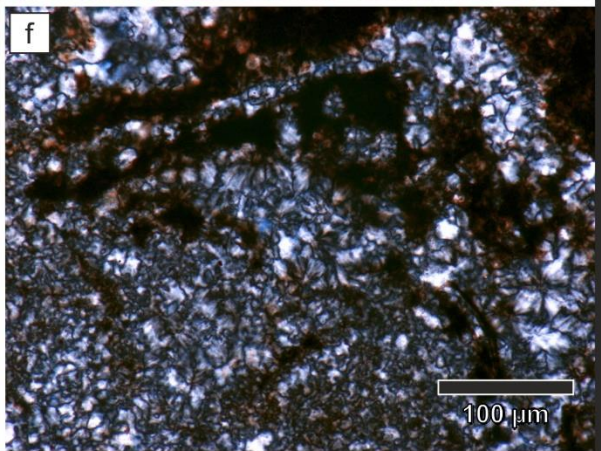
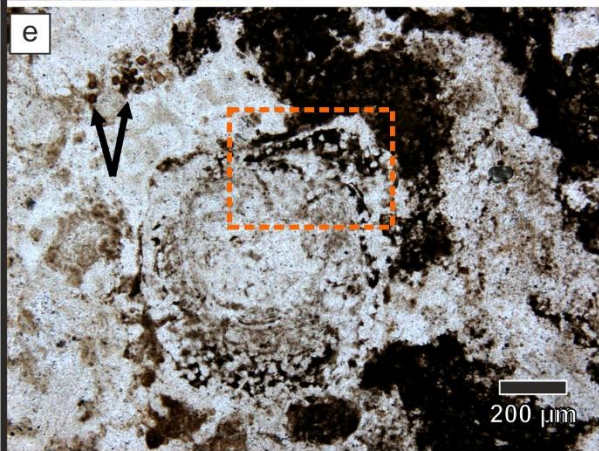
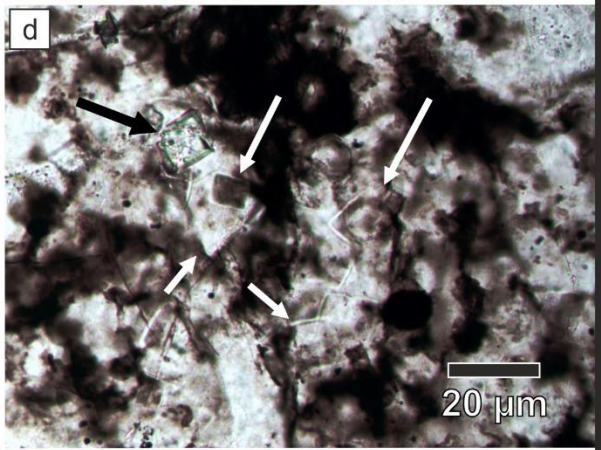
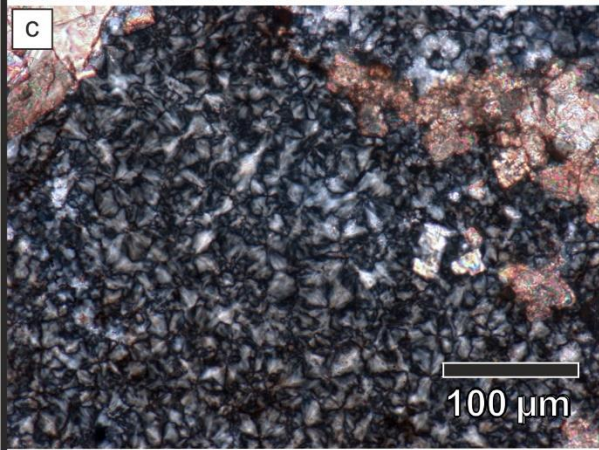
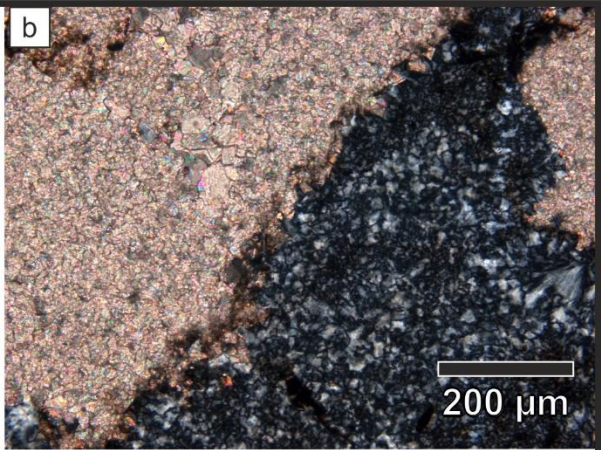
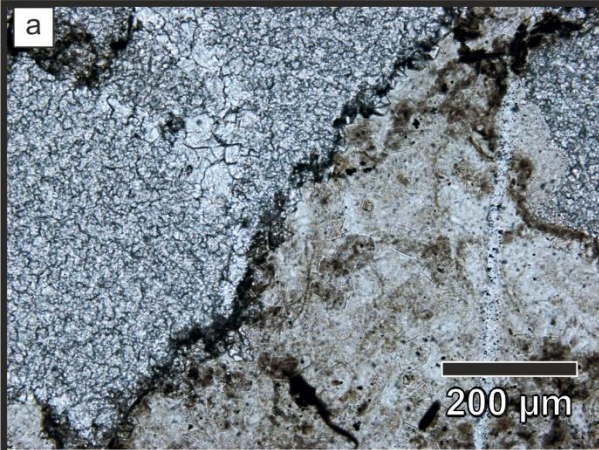
1196

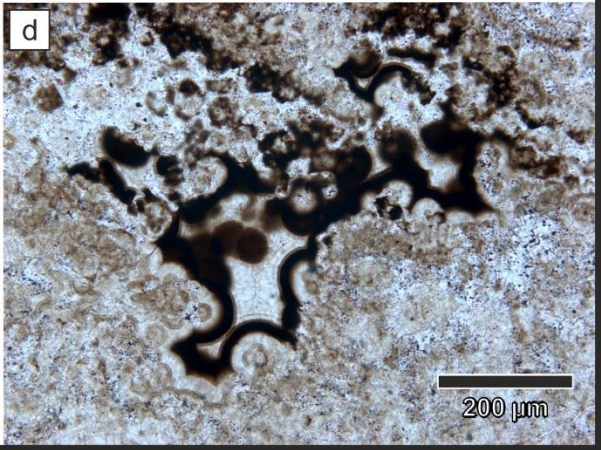
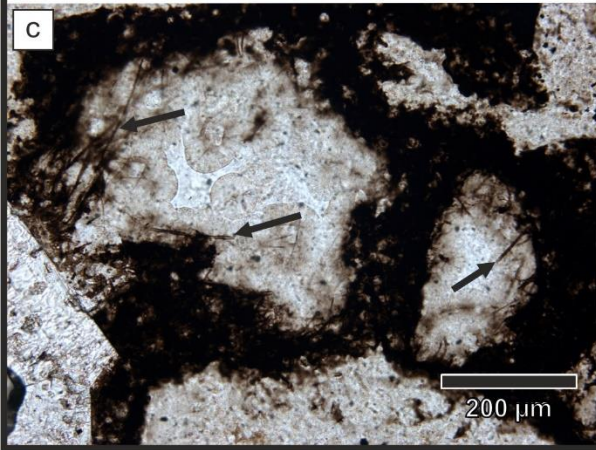
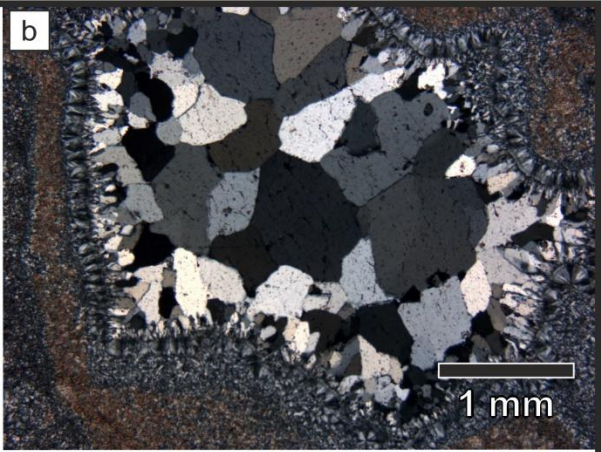
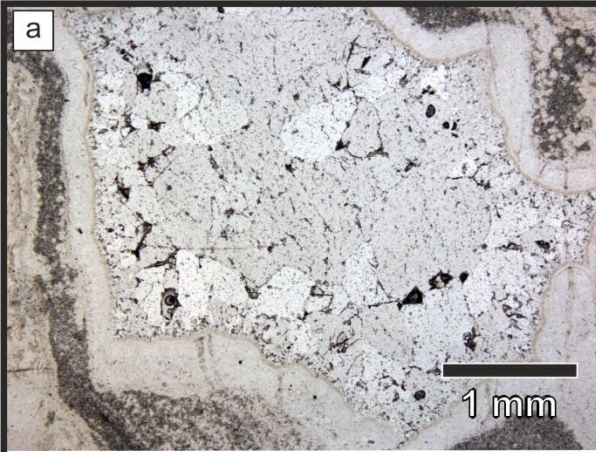
1197 **Figure 15:** TEM images and maps. **(a and b):** LAADF images (diffraction contrast) of the entire FIB foils.
1198 Areas mapped by TEM-EDX are outlined by white squares. Note: foil in b is damaged and turned
1199 clockwise by 90° compared to SEM image shown in figure 14b, dashed line indicates the position of
1200 the area mapped by STXM. **(c and d):** HAADF images, TEM-EDX maps of Si, O, C, and diffraction
1201 patterns of mapped areas outlined in a and b. The HAADF image in the lower center in c shows a
1202 closeup of the C-rich porous area to the left of the EDX maps. The distribution of Cl to the lower center
1203 in d correlates to the bright spots in the HAADF image and indicates the presence of halite. All
1204 diffraction spots/rings stem from polycrystalline quartz.

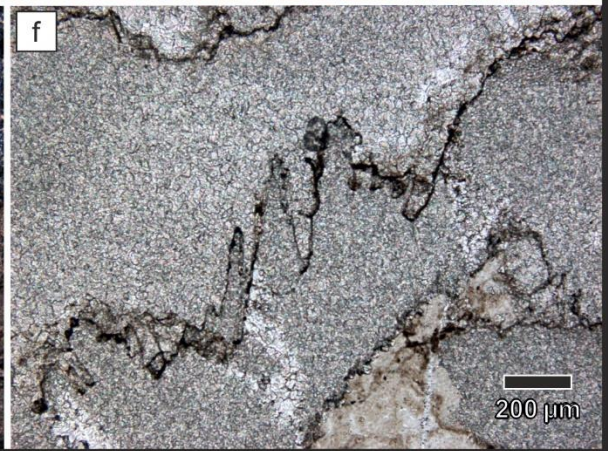
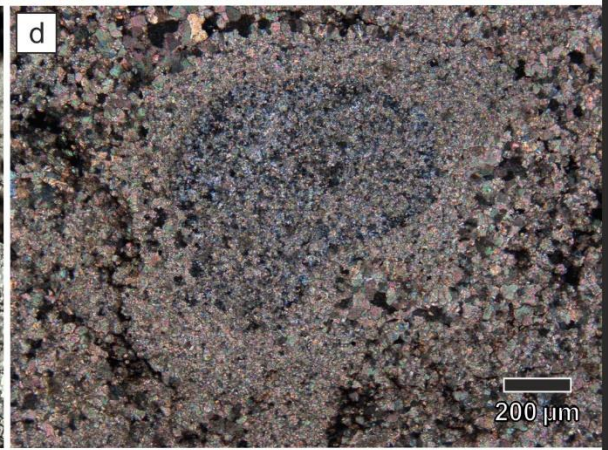
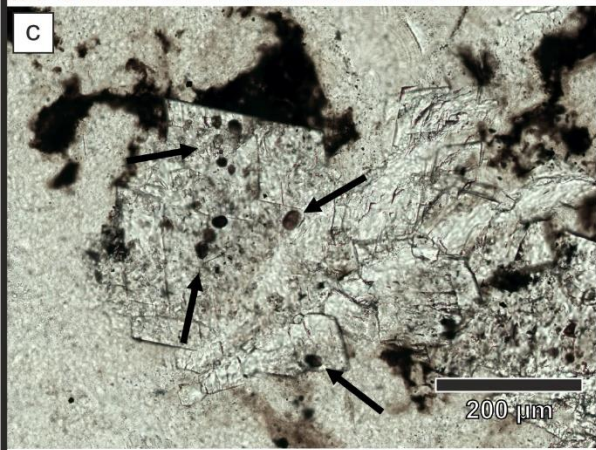
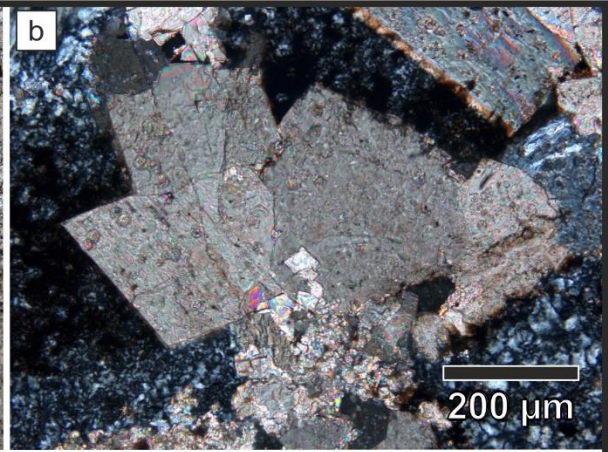
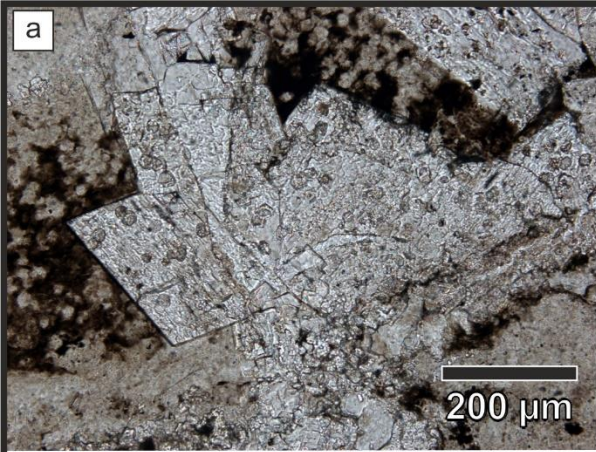


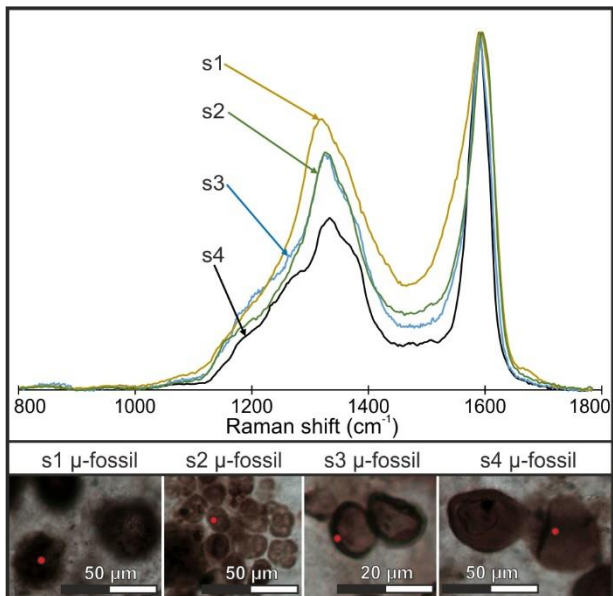
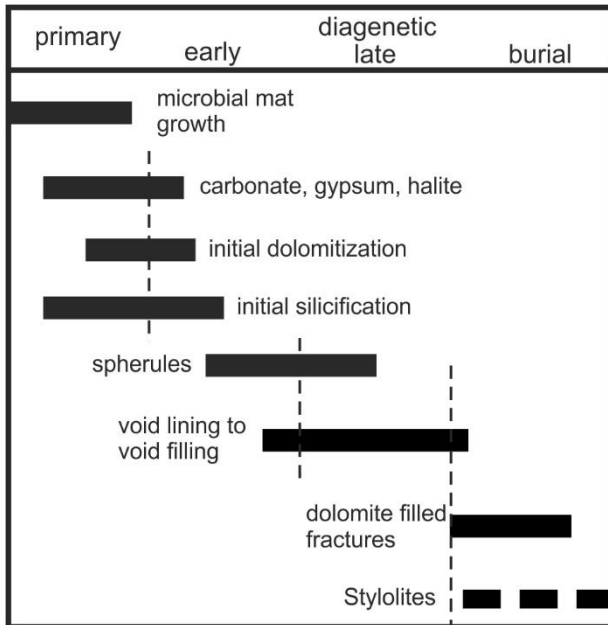


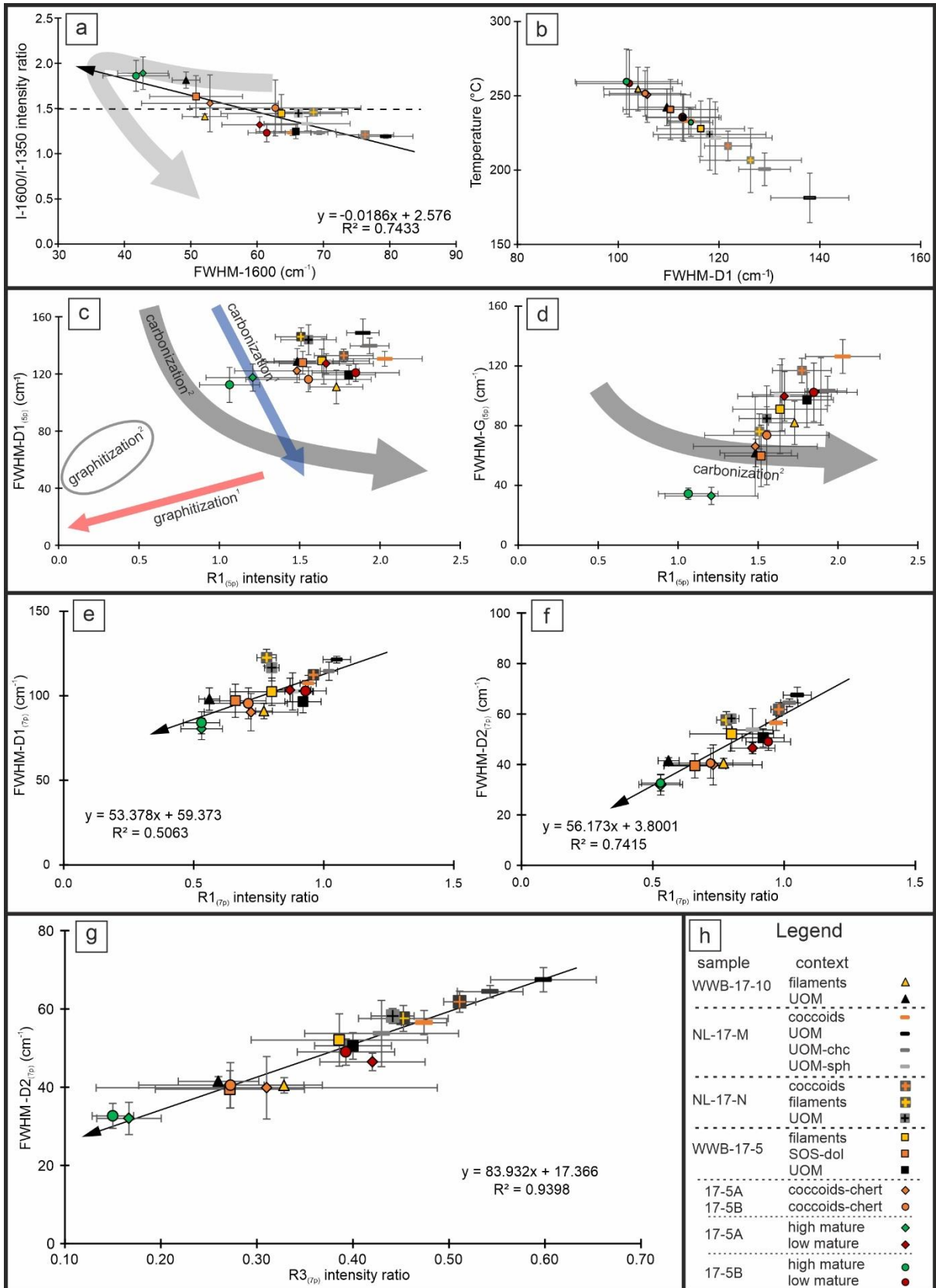


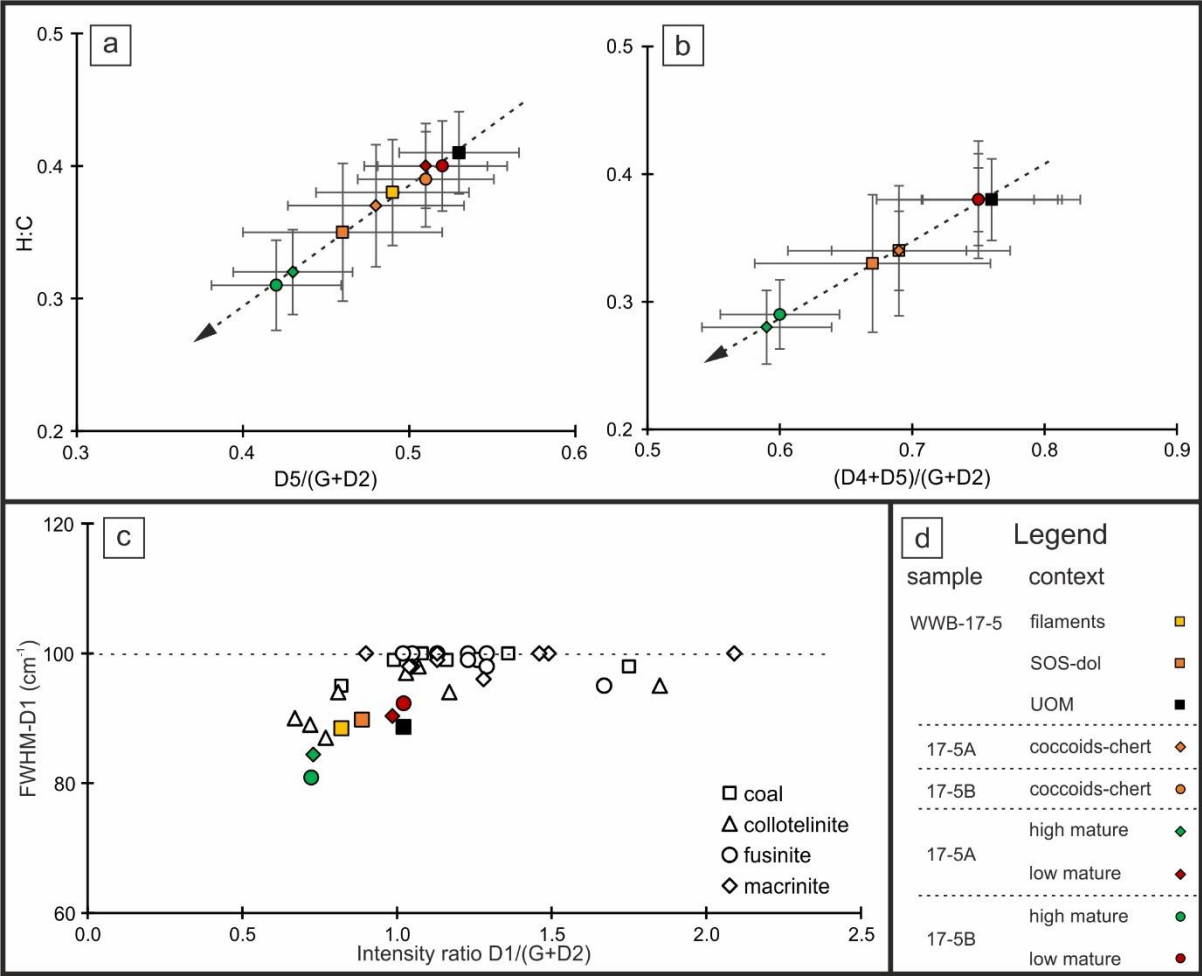


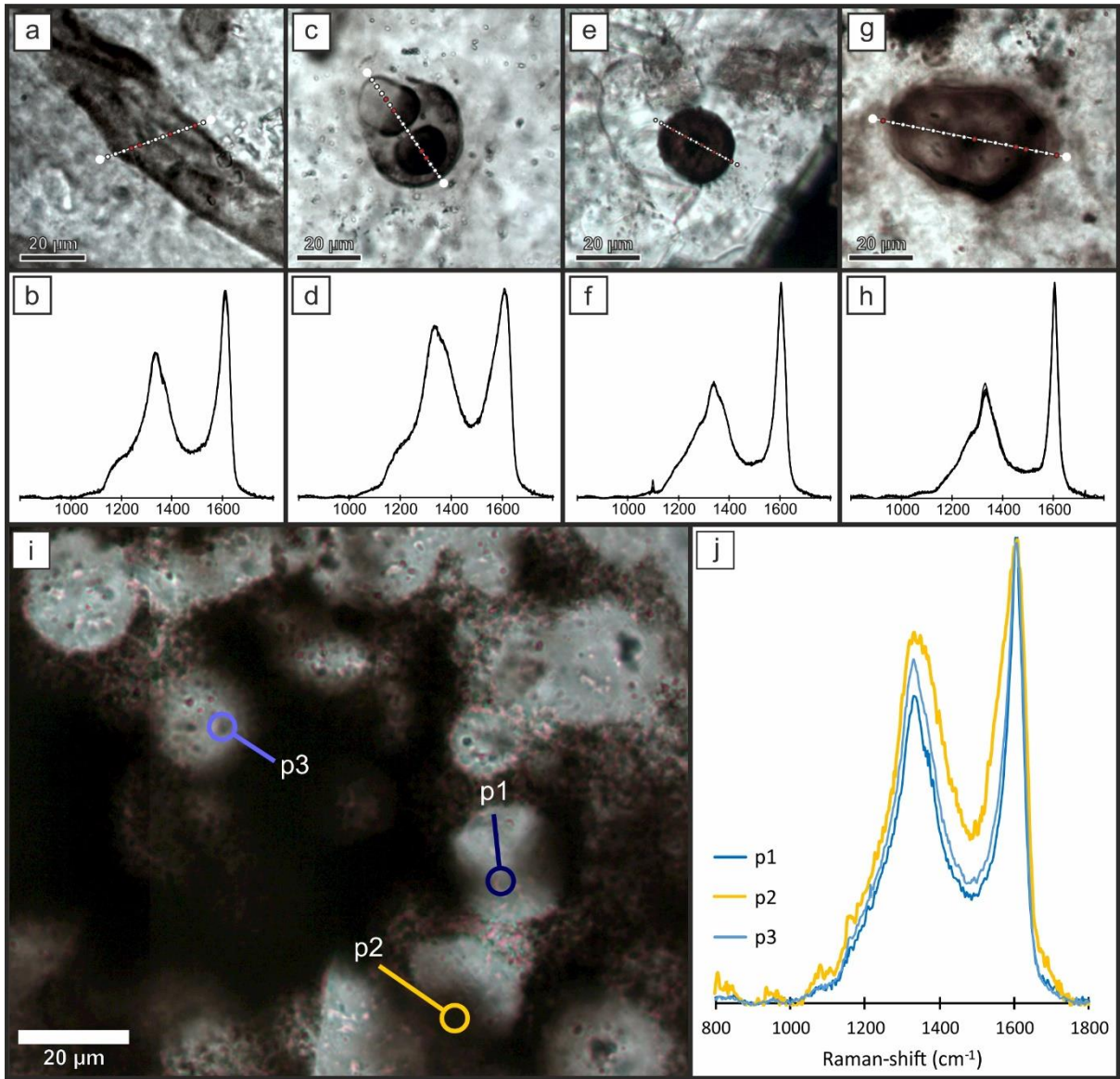


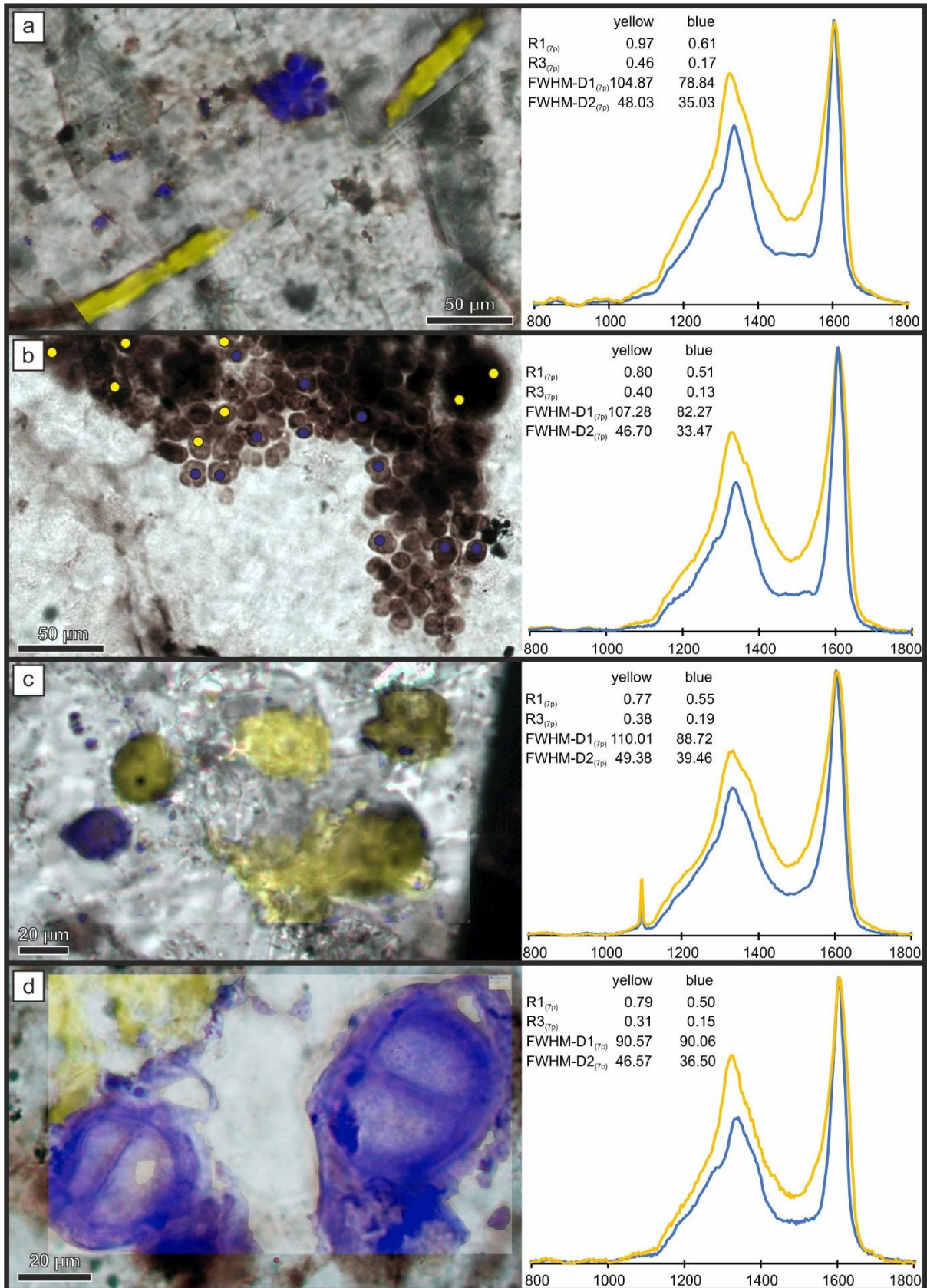


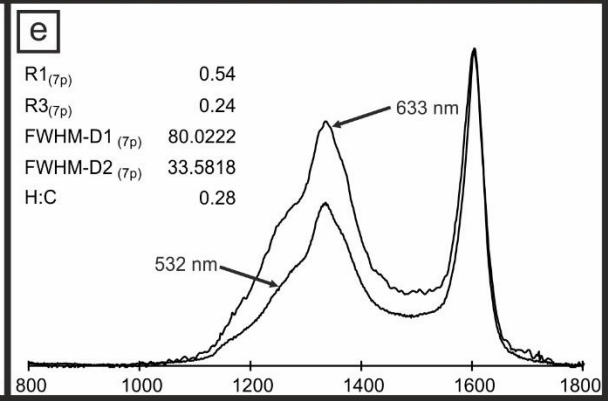
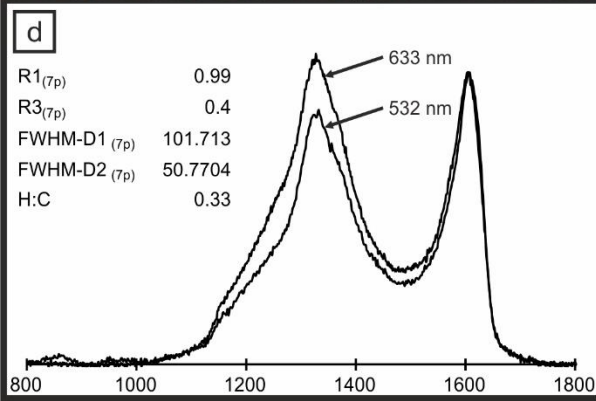
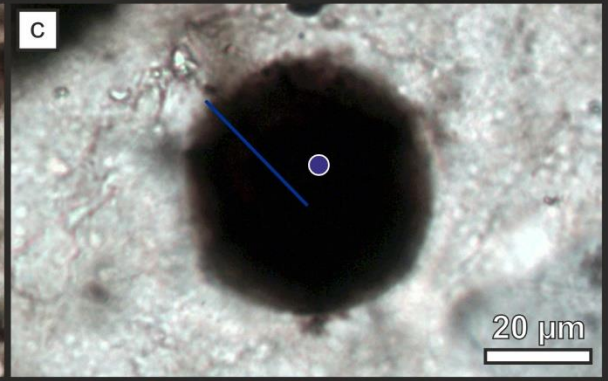
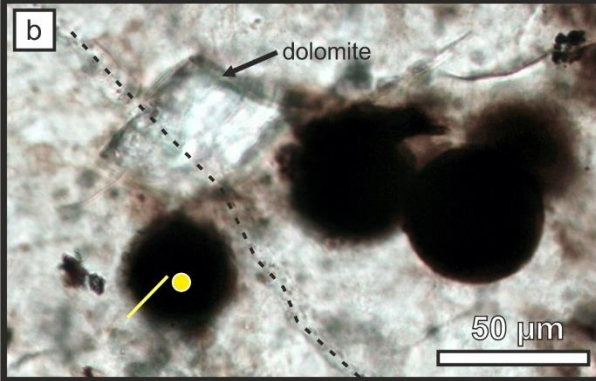


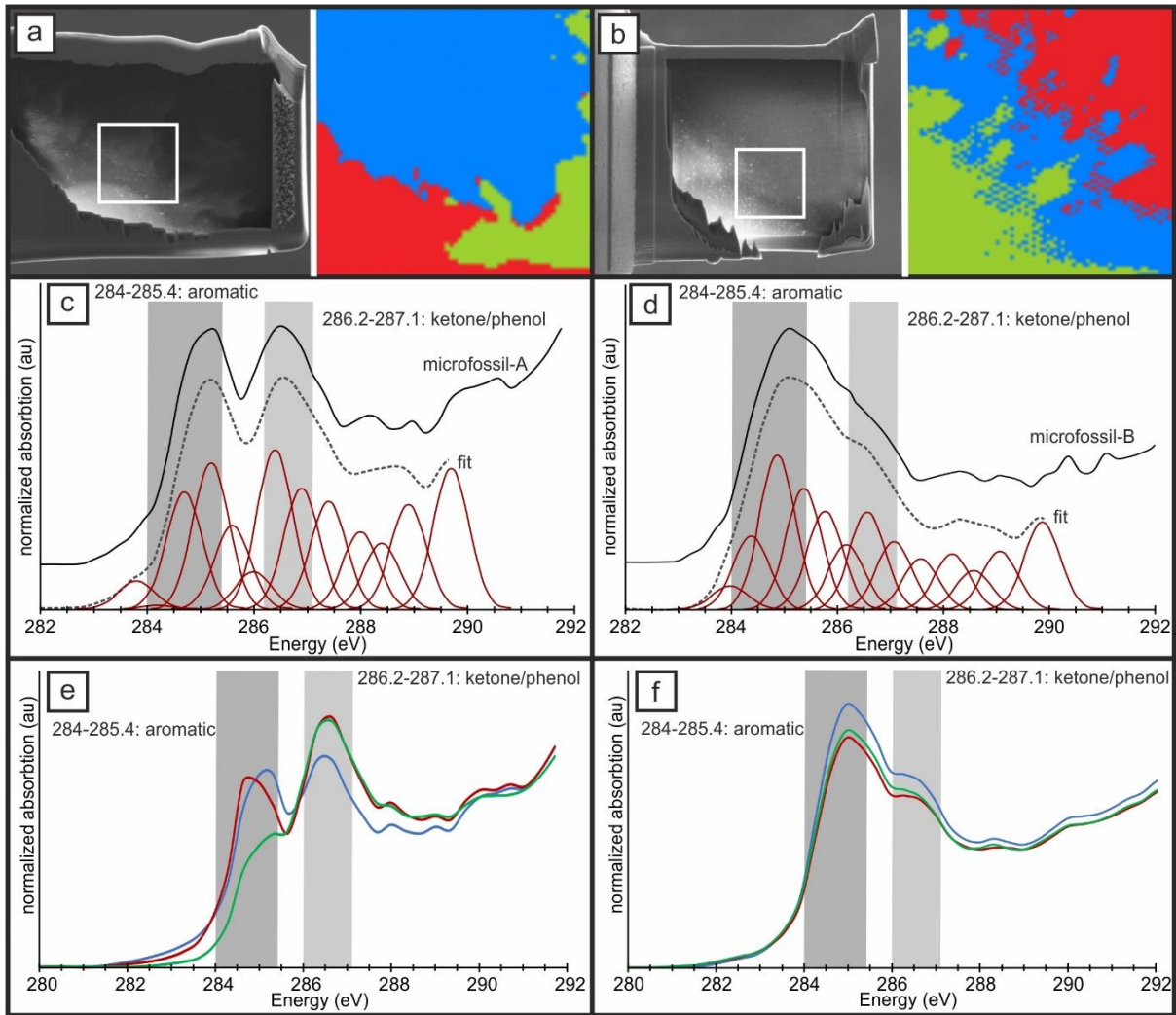












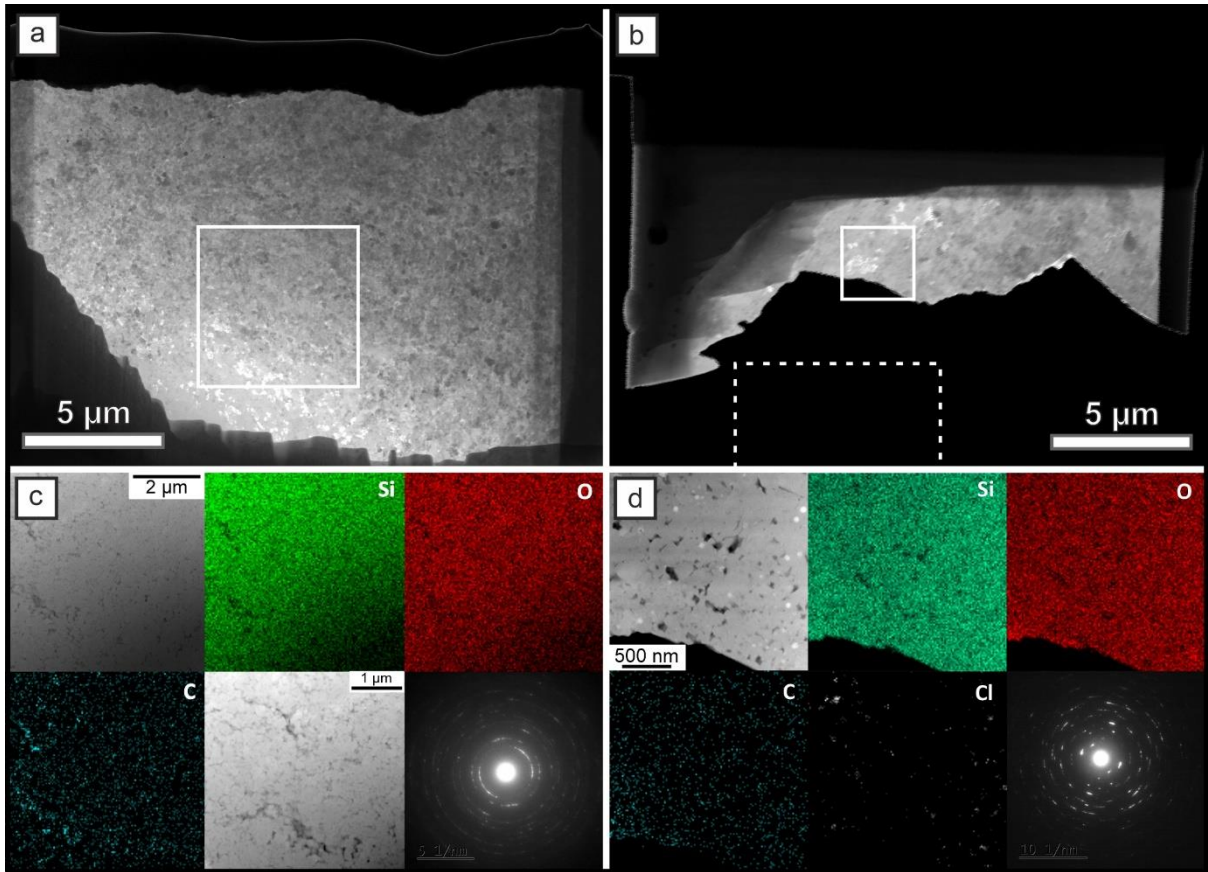


Table 1: Sedimentology, diagenetic context and appearance of organic microfossils in Angmaat cherts. UOM: unrecognizable organic material; gy: gypsum; chc: chalcedony; qz: quartz; dol: dolomite.

Sample	Lithology	primary sedimentary	secondary diagenetic	Microfossils and OM
WWB 17-10	chert, minor dolomite	wavy lamination	pseudomorphs: gy laminated chert laminated dolomite void fillings: chc closed fractures	none filamentous, UOM UOM minor UOM UOM
NL 17-M	chert, dolomite	laminated with nodules	pseudomorphs: gy, dol laminated chert laminated dolomite nodular chert chert spherules void fillings: chc closed fractures	none coccoidal, UOM UOM coccoidal, UOM UOM UOM UOM
NL 17-N	chert	laminated with minor nodules	pseudomorphs: gy laminated chert nodular chert void fillings: qz, chc, dol closed fractures	none coccoidal, filamentous, UOM coccoidal, UOM minor UOM UOM
WWB 17-5	chert, dolomite	nodular	pseudomorphs: dol, gy nodular chert nodular dolomite chert spherules void fillings: chc, dol Fracture filling dol stylolites in dolomite	none coccoidal, minor filamentous, UOM UOM UOM in places filamentous and UOM spherical organic structures UOM

Table 2: Summary of peak decomposition procedures and extracted and calculated Raman parameters.

Decomposition procedure	Peaks with starting position	Extracted parameters	Calculated parameters
No decomposition	none	Intensity of 1350 and 1600 cm^{-1} maxima Intensity at 1540 cm^{-1} FWHM of 1600 cm^{-1} maximum	Intensity ratio I-1600/I-1350 Intensity ratio I-1540/I-1600
4-peak decomposition after Kouketsu et al., 2014	D1 - 1350 cm^{-1} D2 - 1600 cm^{-1} D3 - 1510 cm^{-1} D4 - 1245 cm^{-1}	FWHM-D1 FWHM-D2	T-D1 ($^{\circ}\text{C}$) = - $2.15(\text{FWHM-D1}) + 478$
5-peak decomposition after Delarue et al., 2016	D1 - 1350 cm^{-1} D2 - 1620 cm^{-1} D3 - 1500 cm^{-1} D4 - 1200 cm^{-1} G - 1580 cm^{-1}	Intensity of D1 and G FWHM-D1 and -G	Intensity ratio $R1_{(5p)} = \text{D1/G}$
7-peak decomposition	D1 - 1340 cm^{-1} D2 - 1610 cm^{-1} D3 - 1415 cm^{-1} D3' - 1540 cm^{-1} D4 - 1165 cm^{-1} D5 - 1230 cm^{-1} G - 1570 cm^{-1}	Intensity of D1, G and D3 FWHM-D1 and -D2 Position of G peak	Intensity ratios $R1_{(7p)} = \text{D1/D2}$ and $R3_{(7p)} = \text{D3/D2}$
Decomposition 633 nm spectra after Ferralis et al., 2016	D1 - 1330 cm^{-1} D3 - 1400 cm^{-1} D3' - 1500 cm^{-1} D4 - 1150 cm^{-1} D5 - 1260 cm^{-1} (G+D2) - 1600 cm^{-1}	Intensity of D1, D2, D4, D5 and (G+D2)	Intensity ratios $\text{D1}/(\text{G+D2})$ and $(\text{D4+D5})/(\text{G+D2})$ Ratios H:C = 0.871 * $\text{D5}/(\text{G+D2}) - 0.0508$ and H:C = 0.6024 * $(\text{D4+D5})/(\text{G+D2}) - 0.0739$

Table 2: Raman parameters of OM measured with 532 nm laser and sorted by sample in relation to taxonomic and diagenetic context. ¹after Kouketsu et al., 2014 to estimate maximum thermal alteration; ²after Delarue et al., 2016 to estimate the degree of carbonization; ³7-peak fit to visualize the progressive change of the D2-peak with increasing maturity; sph: chert spherules; cod: coccoids; SOS: spherical organic structures. For spectral shapes (S4 and S1) see Figure 8. Errors are standard deviations of given parameter.

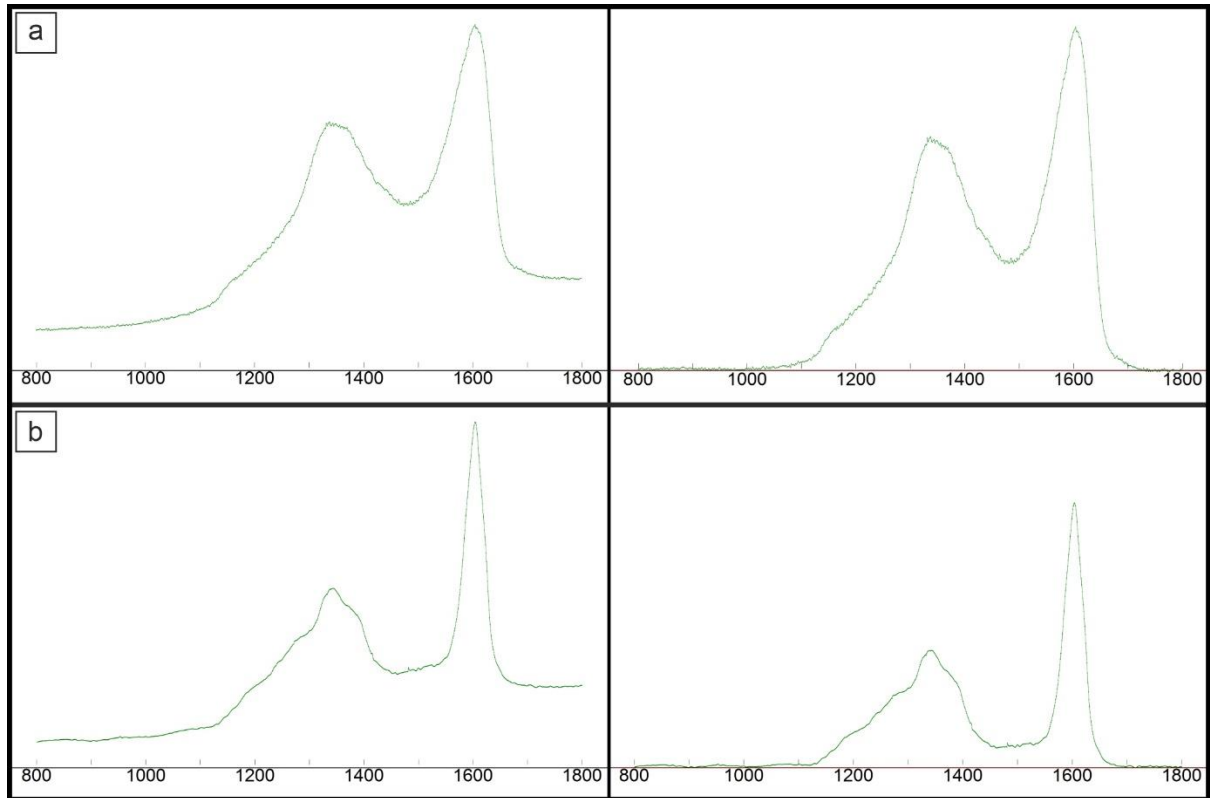
Sample	context	n	no fitting			4-peak-fit ⁺			5-peak fit [*]			7-peak fit				
			1600/1350	1540/1600	FWHM-D2	FWHM-D1	FWHM-D2	T-D1 (°C)	R1 _(5p)	FWHM-D1	FWHM-G	R1 _(7p)	R3 _(7p)	FWHM-D1	FWHM-D2	G-position
WWB-17-10	filaments	22	1.41±0.03	0.29±0.01	52.1±3.4	103.9±6.8	48.4±3.4	254.6±14.7	1.73±0.16	110.9±11.8	81.9±14.6	0.77±0.03	0.33±0.02	90.9±4.5	40.5±1.9	1570.4±2.7
	UOM-chert	11	1.81±0.09	0.27±0.03	49.3±2.1	109.7±5.7	48.7±5.5	242.3±12.3	1.49±0.22	128.7±8.9	61.8±9.3	0.56±0.04	0.26±0.04	98.1±6.6	41.5±1.2	1573.2±2.1
NL-17-M	coccoids	12	1.23±0.03	0.47±0.02	65.4±2.8	113.9±4.2	63.6±2.7	232.9±8.9	2.03±0.23	148.7±5.2	126.4±11.3	0.94±0.03	0.47±0.02	107.4±4.7	56.5±3.1	1555.2±2.2
	UOM	10	1.19±0.02	0.59±0.04	79.4±4.1	138.0±7.7	79.9±4.3	181.3±16.6	1.89±0.1	148.7±9.8	102.9±22.5	1.05±0.05	0.60±0.06	121.4±2.0	67.5±3.1	1551.6±2.4
	UOM-chc	14	1.21±0.03	0.54±0.03	76.3±4.3	129.0±5.1	72.4±3.7	200.6±11.0	1.94±0.12	139.6±5.5	103.3±9.8	1.02±0.03	0.54±0.03	114.5±5.4	64.4±1.6	1550.5±1.9
	UOM-gl	10	1.33±0.08	0.43±0.09	67.5±6.5	119.2±11.3	60.6±9.4	221.6±24.3	1.65±0.18	128.8±15.9	100.8±24.1	0.88±0.08	0.43±0.08	102.6±10.9	53.7±8.5	1560.0±4.9
NL-17-N	coccoids	27	1.23±0.02	0.50±0.01	69.4±1.3	121.8±4.7	66.9±2.5	216.2±10.0	1.77±0.18	132.8±4.6	116.9±8.2	0.96±0.02	0.51±0.02	112.4±2.9	61.8±2.7	1555.6±2.7
	filaments	17	1.46±0.04	0.48±0.02	68.5±5.2	126.3±10.1	69.3±2.5	206.6±21.7	1.51±0.16	146.0±6.4	76.1±11.8	0.78±0.04	0.45±0.05	122.5±4.9	57.6±3.3	1561.8±4.5
	UOM	20	1.45±0.02	0.48±0.02	66.2±3.3	118.1±11.2	67.7±3.0	223.9±24.0	1.56±0.17	143.9±10.6	84.8±7.9	0.80±0.03	0.44±0.02	116.6±7.8	58.2±1.9	1558.7±2.8
WWB-17-5	filaments	25	1.44±0.21	0.40±0.07	63.7±9.1	116.4±8.7	57.4±6.4	227.8±18.7	1.64±0.30	129.1±8.3	90.9±29.8	0.80±0.16	0.39±0.09	102.4±8.1	52.1±6.7	1561.2±8.6
	SOS-dol	21	1.63±0.23	0.27±0.08	50.8±7.0	110.5±9.4	46.1±7.2	240.5±20.2	1.52±0.23	127.8±8.0	59.7±20.6	0.66±0.12	0.27±0.08	96.9±9.8	39.4±4.8	1567.7±5.4
	UOM	30	1.25±0.08	0.38±0.06	65.8±6.0	112.8±7.2	56.4±3.6	235.6±15.6	1.78±0.17	121.8±6.7	102.5±18.4	0.92±0.07	0.40±0.04	100.2±8.3	50.3±3.4	1559.8±3.7
17-5A	cod-chert	54	1.56±0.31	0.27±0.10	52.9±10.3	105.8±8.6	46.7±9.9	250.6±18.5	1.48±0.39	122.1±8.1	66.1±33.3	0.72±0.18	0.31±0.18	90.3±11.1	39.9±8.0	1570.7±7.7
17-5B	cod-chert	65	1.51±0.31	0.27±0.11	62.8±12.9	105.3±7.1	47.4±7.9	251.5±15.2	1.56±0.39	116.1±8.7	73.6±33.1	0.71±0.15	0.27±0.10	95.6±9.2	40.2±5.8	1570.4±6.2
17-5A	high mature	20	1.89±0.18	0.15±0.02	42.8±3.8	102.2±10.5	37.2±4.3	258.3±22.5	1.21±0.29	117.4±9.5	32.9±5.8	0.53±0.08	0.17±0.03	80.5±6.3	32.0±4.1	1578.2±4.1
	low mature	19	1.32±0.09	0.38±0.03	60.4±5.7	114.4±4.3	56.8±2.7	231.9±9.3	1.67±0.29	127.2±7.0	99.7±16.6	0.87±0.08	0.42±0.05	103.4±6.9	46.4±2.2	1563.3±2.6
17-5B	high mature	22	1.86±0.17	0.14±0.01	41.8±5.0	101.6±10.2	36.4±4.8	259.5±21.9	1.04±0.19	114.0±12.3	34.1±3.7	0.53±0.07	0.15±0.02	84.1±6.5	32.6±3.2	1578.5±2.0
	low mature	27	1.23±0.10	0.38±0.03	61.5±2.8	112.9±7.4	56.8±3.3	235.1±15.9	1.85±0.27	120.8±6.1	102.4±19.6	0.93±0.08	0.39±0.05	102.9±6.2	48.9±3.4	1562.2±3.8

Table 3: Overview of parameters and H:C ratios extracted from 633 nm Raman spectra of OM. For spectral shapes (S4 and S1) see Figure 8. Errors are standard deviations of given parameters.

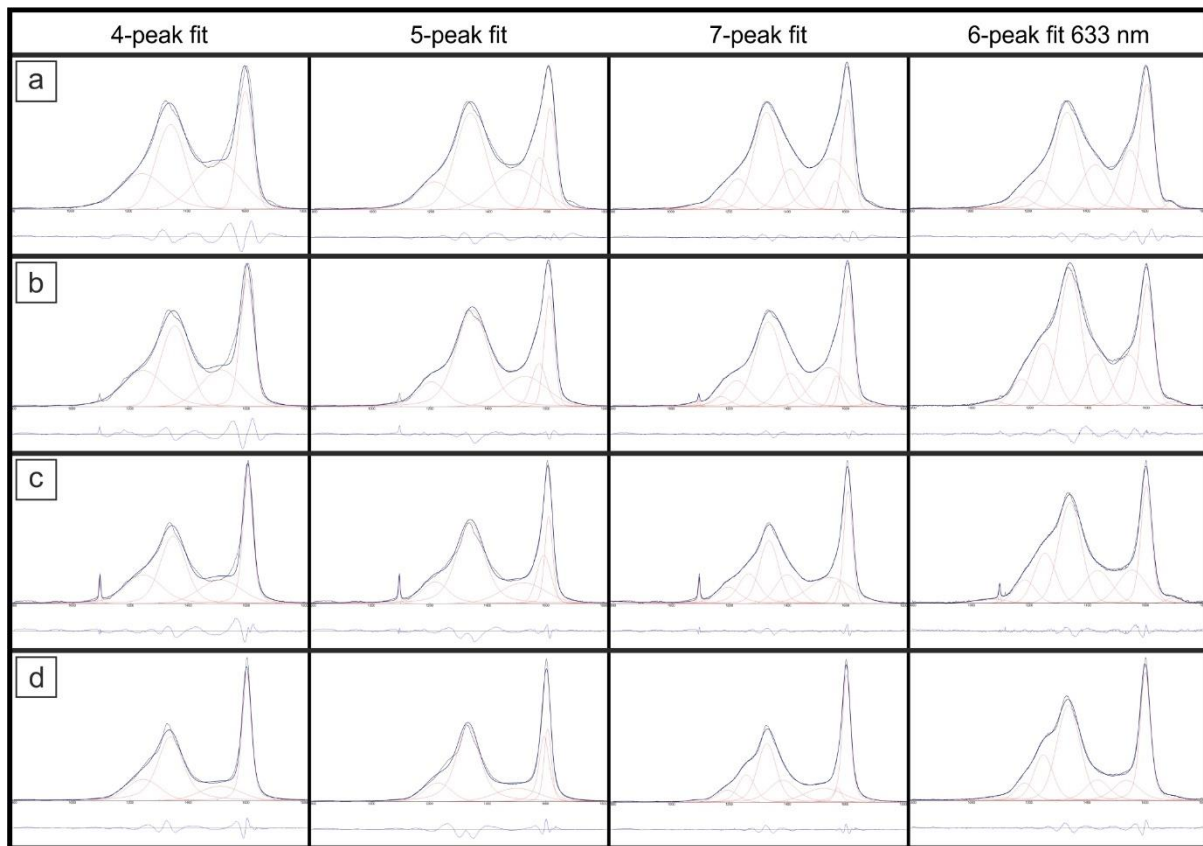
Sample	context	n	D1/(G+D2)	FWHM-D1	D5/(G+D2)	(D4+D5)/(G+D2)	H:C-D5	H:C-D4+D5
WWB-17-5	filaments	4	0.81±0.13	88.61±3.42	0.49±0.046	0.69±0.051	0.38±0.04	0.34±0.031
	SOS-dol	18	0.88±0.09	89.68±5.59	0.46±0.06	0.67±0.089	0.35±0.052	0.33±0.054
	UOM	17	1.01±0.05	88.75±6.93	0.53±0.036	0.76±0.053	0.41±0.031	0.38±0.032
17-5A	cod-chert	54			0.48±0.053	0.69±0.084	0.37±0.056	0.34±0.051
17-5B	cod-chert	65			0.51±0.041	0.75±0.077	0.39±0.036	0.38±0.046
17-5A	S4	20	0.73±0.04	84.35±5.88	0.43±0.036	0.59±0.049	0.32±0.032	0.28±0.029
	S1	19	0.98±0.06	90.33±5.14	0.51±0.037	0.75±0.042	0.40±0.032	0.38±0.025
17-5B	S4	22	0.72±0.05	81.18±4.72	0.42±0.039	0.60±0.045	0.31±0.034	0.29±0.027
	S1	27	1.00±0.06	92.30±4.87	0.52±0.039	0.75±0.06	0.40±0.034	0.38±0.036

Supplementary material for:

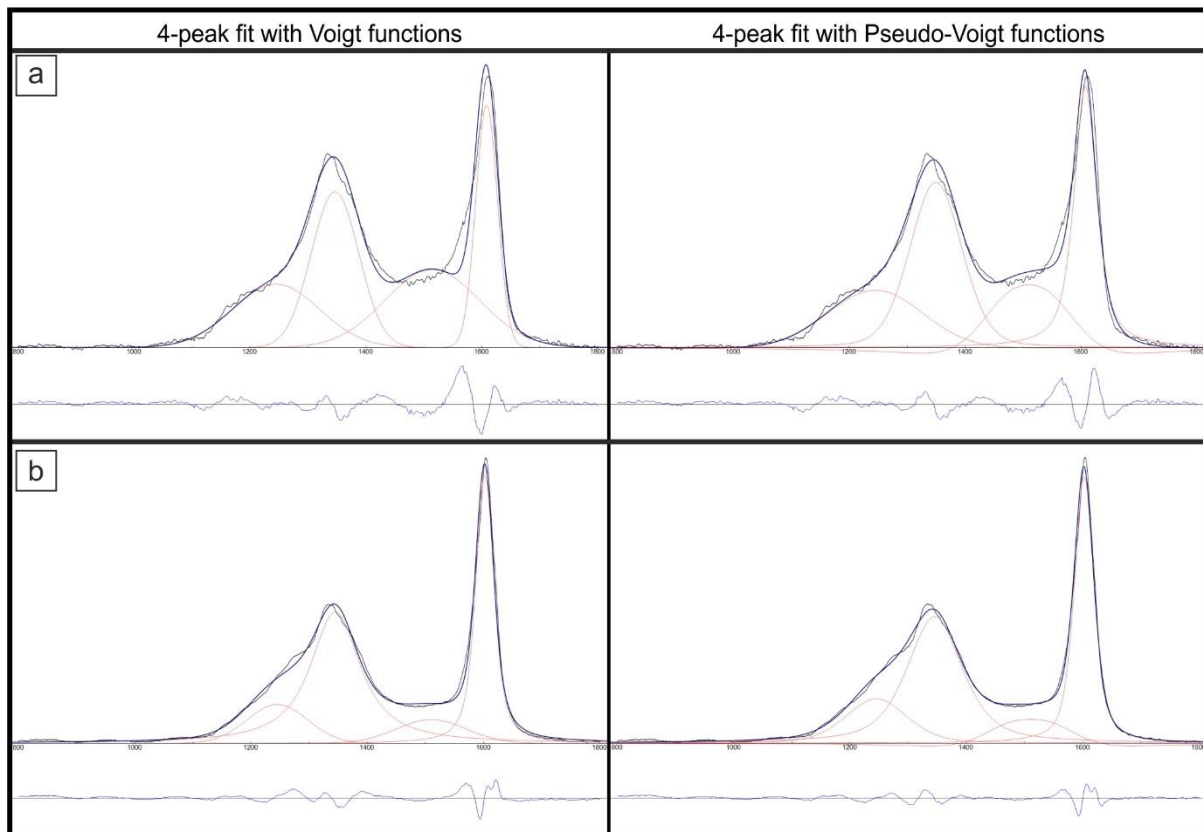
Structural and chemical heterogeneity of Proterozoic organic microfossils of the ca. 1 Ga old Angmaat Formation, Baffin Island, Canada



Supplementary Figure 1: Raman spectra from Angmaat chert before and after baseline correction was applied. (a): Raman spectrum of spectral shape S1 indicating lower mature OM. (b): Raman spectrum of spectral shape S4 indicating higher mature OM.



Supplementary Figure 2: Raman spectra from Angmaat chert showing spectral shapes S1 - S4 (a – d, black lines) with fitting procedures used for spectral decomposition (red peaks), decomposition results (blue lines) and difference spectra below each fitted spectrum.



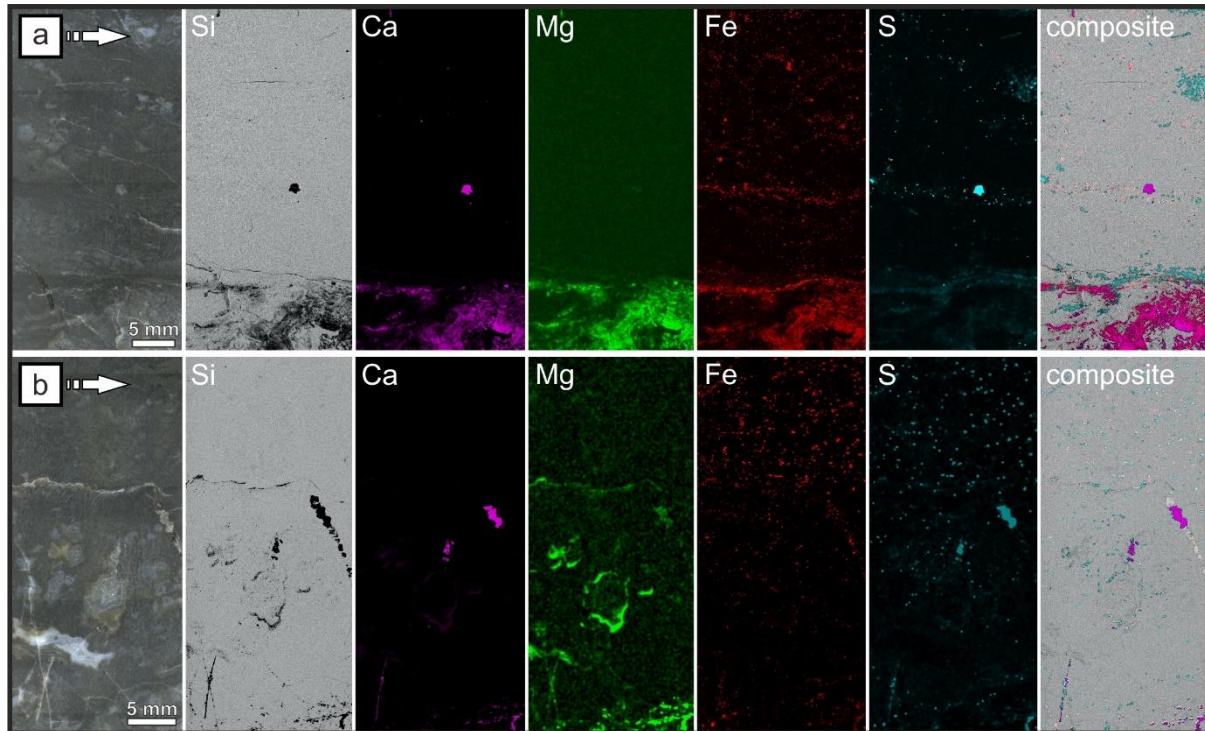
Supplementary Figure 3: Peak fitting of Raman-spectra of low mature **(a)**: and high mature **(b)**: OM from Angmaat chert according to fitting procedure G of Kouketsu et al., 2014 using Voigt functions (left) and Pseudo-Voigt functions (right). Note the negative excursions of the D3-peak resulting from the use of Pseudo-Voigt functions.

Micro-XRF mapping:

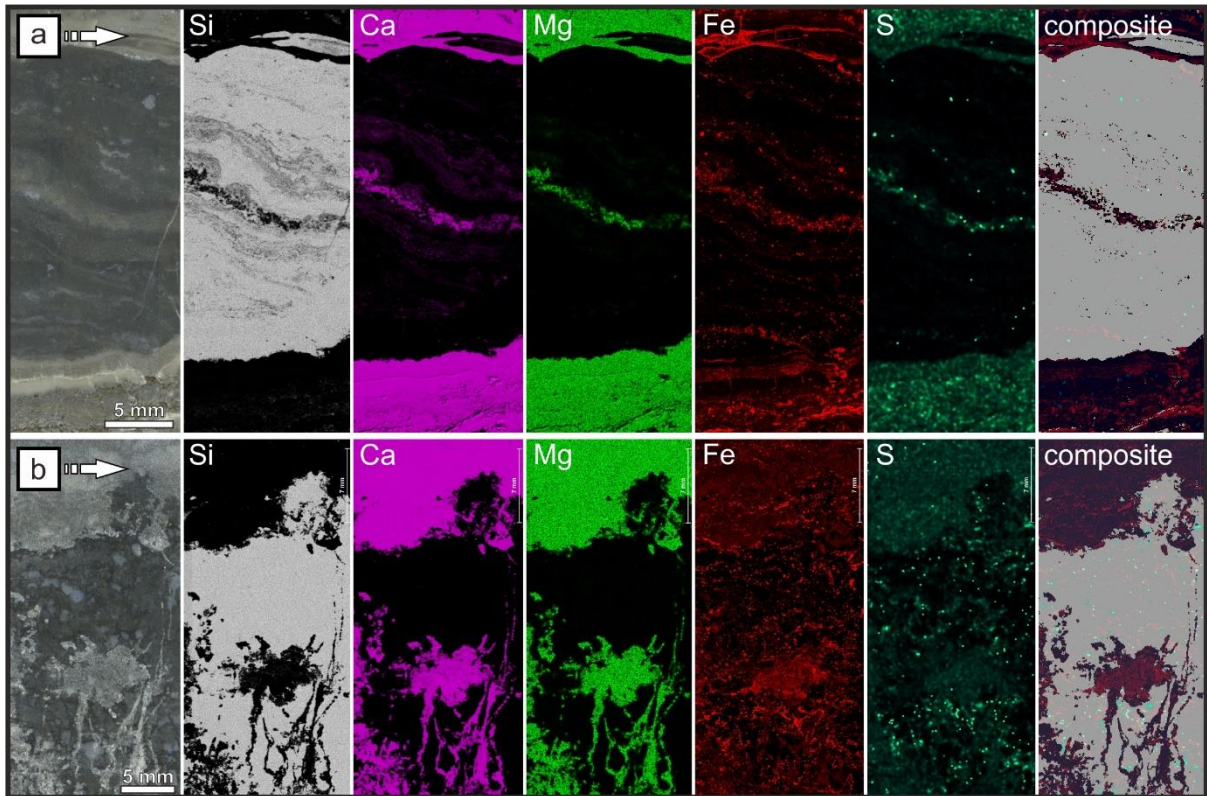
μ -XRF mapping was performed using the Bruker Tornado M4 micro-X-ray fluorescence analyzer of the department of Geosciences of the Friedrich-Schiller-University in Jena. We used the ca. 2 x 4 cm large billets of the respective thin sections NL-17-M, NL-17-N, WWB-17-10 and WWB-17-5A to determine the elemental composition and the distribution of the detected elements of the analyzed material. Elemental maps were recorded with spot size of 20 μm and a step sizes of ca. 27 μm at a dwell time of 35 ms at each spot. The current was set to 200 μA at a voltage of 50 kV and the sample chamber was evacuated to an air pressure of 20 mbar. The detection limit of this method is ca. 0.1 w%

All samples show Si as most common element without overlap with other detected elements and therefore indicative of the broadly siliceous (quartz) composition of the analyzed material. Other detected major elements are Ca, Mg, Fe, and S are all displayed in Supplementary Figures 4 and 5. Elements like Al, Mn and Ti are detected as minor components mostly concentrated in few small spots and are not shown here. In all analyzed samples Ca and Mg largely overlap as typical for a dolomitic composition with minor contents of Fe and S as indicated by a faint signal of these elements that overlaps with the stronger Ca and Mg signals. Stronger signals of S appear spotty throughout all samples and overlap mostly with similarly strong Fe signals indicative of small pyrite grains. However, a few larger spots enriched in S also overlap with Ca indicating a CaSO_4 composition (Supplementary Figure 4). This material is strictly limited to fracture fillings and the exact mineralogical composition of

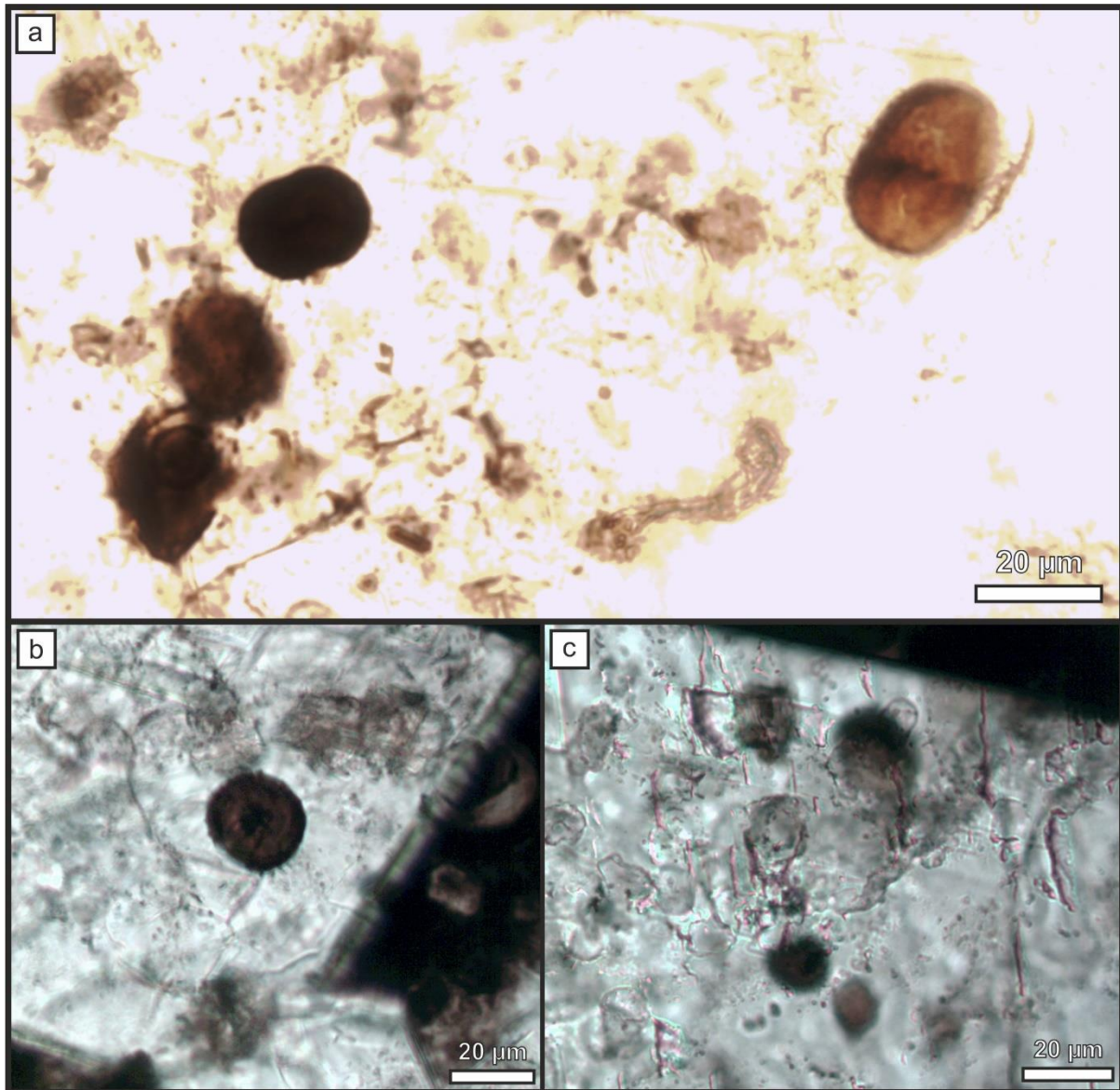
this phase cannot be inferred. Apart from the appearance of Fe in the dolomitic phase and as potential pyrite it appears also as strong signal at thin laminations in and close to the dolomitic areas. Petrographic microscopy shows that such areas are composed of a brown mineral phase and with the exclusive appearance of Fe in this area in the μ -XRF maps this mineral phase is most likely an iron-oxide such as hematite.



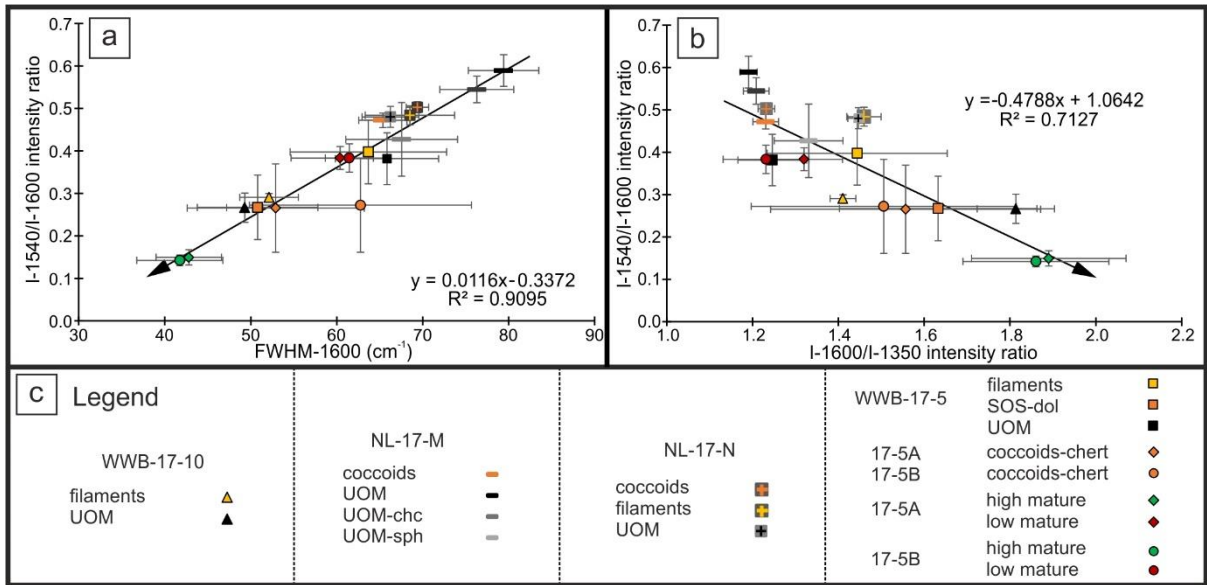
Supplementary Figure 4: μ -XRF element maps of black chert samples from the Angmaat Formation. **(a+b):** From left to right: Overview image of scanned billet (the scale applies to all images), elemental maps (Si, Ca, Mg, Fe and S) and composite map of elements to visualize minerals. Minerals inferred from the element maps are quartz (dark gray), dolomite (purple), pyrite (light blue) and iron oxides (pale red). The overlapping areas with Ca and S are CaSO_4 -rich fracture fillings **(a):** Sample NL-17-M, laminated chert with few chert nodules. **(b):** Sample NL-17-N, laminated chert with few nodules and numerous up to 5 mm large chalcedony and dolomite filled voids. Note the Mg enrichment on the edges of the voids.



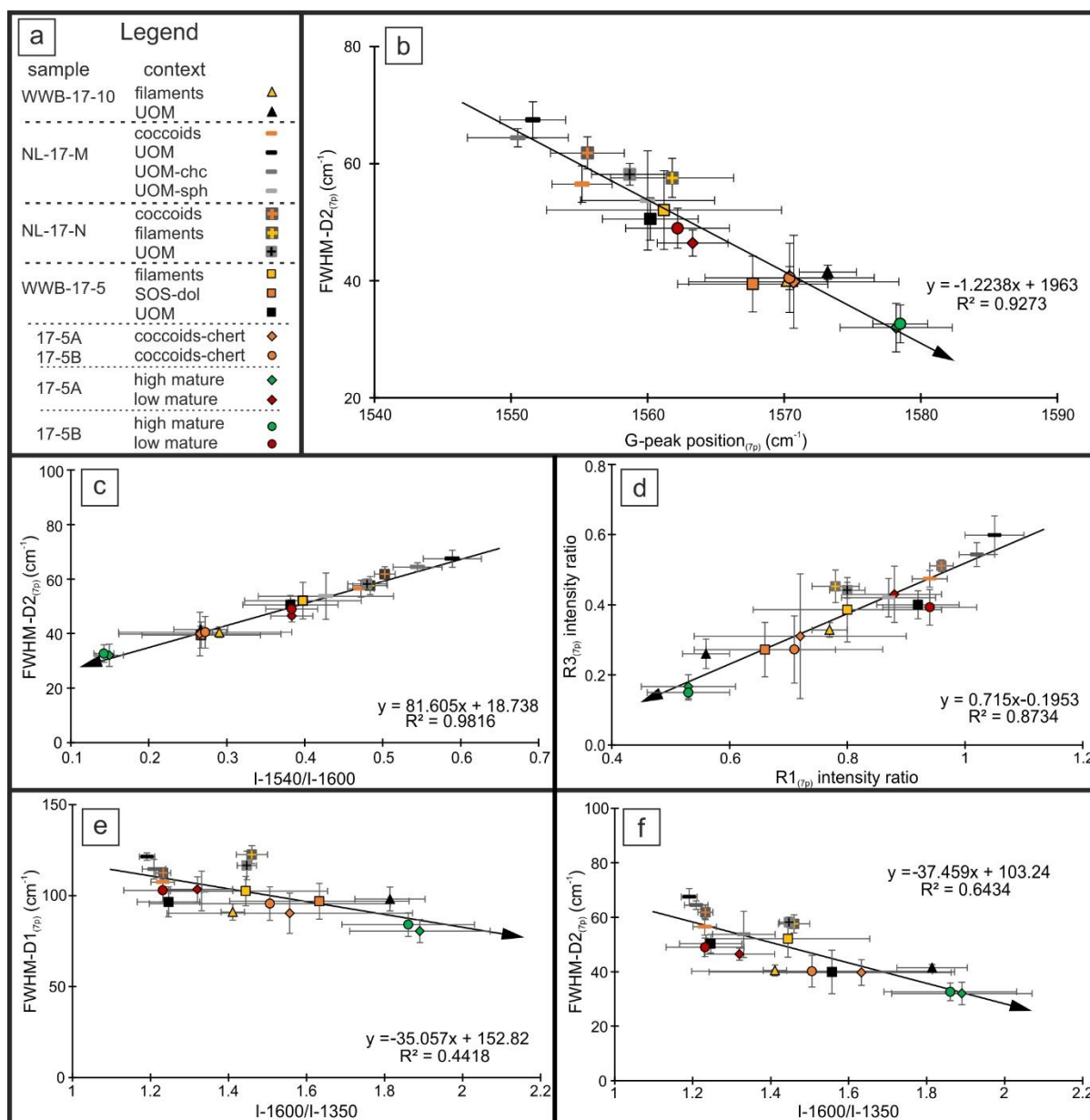
Supplementary Figure 5: μ -XRF element maps of black chert samples from the Angmaat Formation. **(a+b):** From left to right: Overview image of scanned billet (the scale applies to all images), elemental maps (Si, Ca, Mg, Fe and S) and composite map of elements to visualize minerals. Minerals inferred from the element maps are quartz (dark gray), dolomite (dark blue), pyrite (light blue) and iron oxides (red). The S in the Ca and Mg rich areas is indicative of minor portions of sulfate **(a):** Sample WWB-17-10, a wavy laminated chert. **(b):** Sample WWB-17-5A, a nodular chert with sub-vertical dolomite fractures.



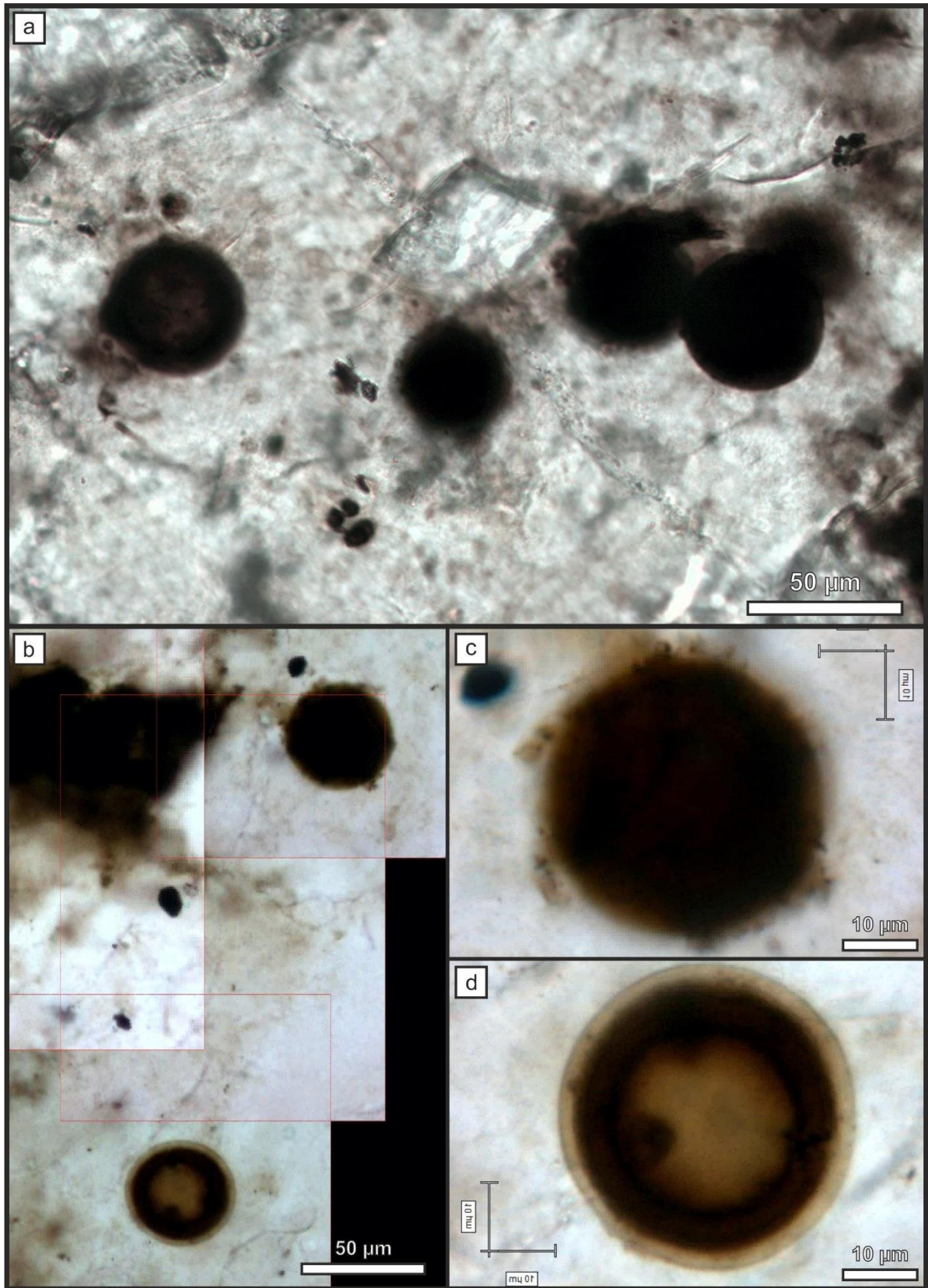
Supplementary Figure 6: Spherical organic structures (SOS) in secondary dolomite in sample WWB-17-5. Structures shown in a and b show internal textures that might indicate their origin as coccoidal microfossils while SOS in c show no internal textures and are more likely chert spherules coated by organic matter.



Supplementary Figure 7: Raman-parameters extracted prior to peak-fitting of Raman-spectra of OM obtained with 533 nm laser. **(a):** FWHM-1600 cm⁻¹ vs. intensity ratio I-1540/I-1600. **(b):** Intensity ratio I-1600/I-1350 vs. intensity ratio I-1540/I-1600. **(c):** Legend for a and b. **Note:** Black arrows in plots shows the approximate development of parameters with increasing maturity of organic matter.

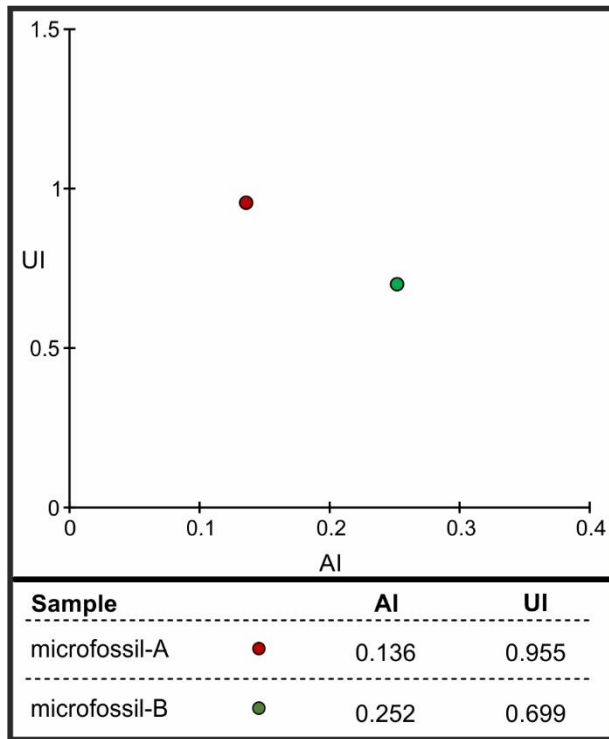


Supplementary Figure 8: Raman-parameters extracted prior to peak-fitting and from 7-peak fitting procedure of Raman-spectra OM obtained with 533 nm laser. **(a):** Legend for b - f. **(b):** FWHM-D2 vs. G-peak position of 7-peak fitting procedure. **(c):** FWHM-D2 of 7-peak fit vs. intensity ratio I-1540/I-1600. **(d):** R1 vs. R3 ratios extracted from 7-peak fitting procedure. **(e):** Intensity ratio I-1600/I-1350 vs. FWHM-D1 of 7-peak fit. **(f):** Intensity ratio I-1600/I-1350 vs. FWHM-D2 extracted from 7-peak fit. **Note:** Black arrows in plots shows the approximate development of parameters with increasing maturity of organic matter. Plots in b -d show a good linear correlation between parameters while linear correlations in plots in e and f are less well pronounced similar to Plots shown in Figure 9c-f.

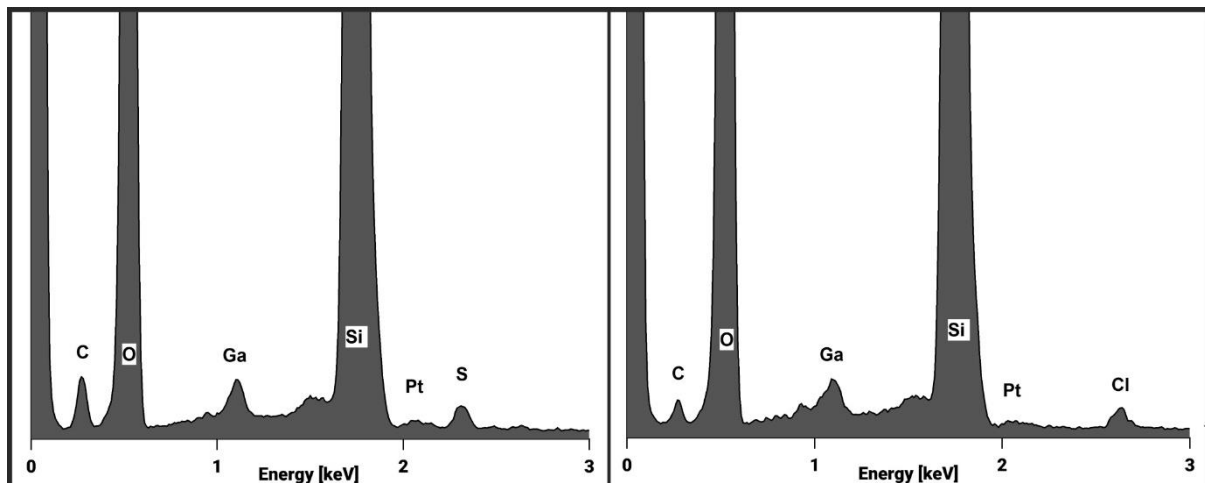


Supplementary Figure 9: Coccolithal microfossils from sample WWB-17-5 used for STXM analysis in their preservation context. (a): Small colony of four coccolithal microfossils preserved in chert most likely individuals of *Gloeodiniopsis* sp. The microfossil to the right shows potential cellular structures.

The microfossils chosen for STXM analysis is in the center of the image. **(b-d)**: Two potential individuals of *Gloeodiniopsis* sp. preserved in chert. The individual shown in (c) was chosen for STXM-analysis while the neighboring individual in (d) clearly shows preserved internal cellular structures.



Supplementary Figure 10: Chemical variation of organic microfossils detected by STXM-mapping and represented by the aromaticity index (AI) plotted against the unsaturated index (UI) both extracted from NEXAFS spectra shown in Figure 14c and d.



Supplementary Figure 11: TEM-EDX spectra of mapped areas from microfossil-A (left) and -B (right). Both samples show mostly Si and O with minor amounts of C, S and Cl. Ga and Pt are relicts from using a platinum strap to fix the sample on the sample holder.

Supplementary Table 1: Functional carbon groups and respective peak-positions in NEXAFS spectra after Alleon et al. (2017) and Bonneville et al. (2020).

Functional group	Fit position (eV)
aromatic	284
quinones	284.4
aromatic/olefinic	284.9
aromatic	285.4
imines	285.8
ketone/phenol	286.2
ketone/phenol	286.6
ketone/phenol	287.1
aliphatic	287.6
amide	288.2
carboxylic	288.6
aldehydes	289.1
aliphatic	289.9